ABSTRACT

Title of dissertation: DESIGN, FABRICATION AND TESTING OF MICRONOZZLES FOR GAS SENSING APPLICATIONS

Sheng Li, Doctor of Philosophy, 2006

Dissertation directed by: Professor Reza Ghodssi
Department of Electrical and Computer Engineering

Real-time identification and quantitative analysis of volatile and semi-volatile chemical vapors are critical for environmental monitoring. Currently available portable instruments lack the sensitivity for routine air quality monitoring, so preconcentrators are employed as front-ends for miniaturized chemical sensors. However, commonly used techniques for sensitivity enhancement have a time constant associated with adsorption/desorption or permeation of gas molecules being concentrated. Little work has been reported on fast-response concentrating techniques for gas sensing applications.

This research is devoted to the development of a fast-response microfluidic gas concentrating device with appropriate flow dynamic shapes and pressure gradients based

on the separation nozzle method. It is capable of concentrating heavy gas molecules diluted in light ones when they are flowing at high speeds, thus maintaining the measurement system response time. This is promising for developing real-time preconcentrators to improve the sensitivity of miniature chemical sensors.

In the initial phase of this work, linear test structures were used to characterize viscous effects in microfluidic devices. Unit processes were developed to fabricate encapsulated micronozzles with through-hole inlets and outlets. The mass flow efficiency of the test structures was measured to be in the range of 0.36-0.81, increasing with rising Reynolds number as a result of the decreasing influence of boundary layers.

Single-stage gas concentration devices were designed and fabricated on the basis of the test structures. A gas separation experimental setup and a mass spectrometric analysis apparatus were developed to evaluate the performance of the devices. Analytical and finite element analyses were conducted to better understand and verify the experimental results.

As a proof-of-concept, gas separation experiments with two different inert gas mixtures were carried out in conjunction with mass spectrometric analysis. More than two-fold enrichment of SF_6 molecules with a response time on the order of 0.01 ms was demonstrated through the device. The effects of design parameters and operating conditions on the separation factor were determined experimentally and compared to the numerical simulation results. This study forms the basis for developing a cascade of single-stage elements envisioned as a preconcentrator for miniature chemical sensors to realize real-time environmental monitoring.

DESIGN, FABRICATION AND TESTING OF MICRONOZZLES FOR GAS SENSING APPLICATIONS

by

Sheng Li

Dissertation submitted to the Faculty of the Graduate School of the
University of Maryland, College Park in partial fulfillment
of the requirements for the degree of
Doctor of Philosophy
2006

Advisory Committee:
Professor Reza Ghodssi, Chair
Professor Christopher Cadou
Professor Peter Kofinas
Professor Perinkulam Krishnaprasad
Professor John Melngailis

Dedication

To Fangfang.

And to my parents and my son, Steven.

Acknowledgements

This dissertation has only been possible with the help of many individuals in the past few years, and its completion is a tribute to them.

My first acknowledgement is to my advisor, Prof. Reza Ghodssi, who introduced me to MEMS, and has always been a source of inspiration and encouragement. I would also like to thank the committee members, Prof. Christopher Cadou, Prof. Peter Kofinas, Prof. Perinkulam Krishnaprasad, and Prof. John Melngailis, for their constructive comments and feedback.

Many colleagues at the University of Maryland provided help and support in many different ways. I especially acknowledge Mr. Jonathan Day and Prof. Christopher Cadou (Department of Aerospace Engineering) who made significant contributions to device modeling. Mr. Jung J. Park, Mr. Wei Lei, Mr. Laurent Henn-Lecordier, Ms. Yuhong Cai, and Prof. Gary Rubloff (Department of Materials Science and Engineering) were extremely helpful with device characterization using mass spectrometry. I wish to thank Mr. Yiu Au (ECE) for his help in modeling linear micronozzles and developing the automated pressure measurement system. I am indebted to Mr. Nolan Ballew and Mr. Tom Loughran for their assistance in using the IREAP and ECE cleanroom facilities, respectively. All the members of MSAL assisted in various aspects of this research. I especially thank Dr. Marcel Pruessner for reviewing this dissertation and giving me useful comments and suggestions.

Also my sincere thanks go to Dr. Carl B. Freidhoff and Dr. Robert M. Young at Northrop Grumman who gave me valuable suggestions on the design, fabrication and characterization of linear test structures, and to Mr. Jeff S. Pulskamp who helped me in the anodic bonding process. In addition, Northrop Grumman funded the initial phase of this work.

Finally, I am very grateful for my family. My wife, Fangfang, provides a cozy atmosphere at home for me to escape from the lab. My son, Steven, is my source of joy. My parents in China have always encouraged me along the way to achieve my academic goals. Words fail to express my gratitude for their enduring love, support, and sacrifices.

Sheng Li
February 6, 2006

Table of Contents

Dedication ii
Acknowledgements iii
Table of Contents iv
List of Tables vii
List of Figures viii

CHAPTER 1 1
INTRODUCTION 1
1.1 Introduction 1
1.2 Motivation and Background 2
1.3 Literature Review 3
1.3.1 Common Sensitivity Enhancement Techniques 3
1.3.2 Separation Nozzle Method for Isotope Separation 7
1.4 Objectives 11
1.5 Contributions 11
1.6 Thesis Organization 13

CHAPTER 2 14
LINEAR TEST STRUCTURES 14
2.1 Introduction 14
2.2 Design of Linear Nozzles 15
2.2.1 One-dimensional Isentropic Model 17
2.2.2 Finite Element Analysis 20
2.3 Device Fabrication and Packaging 22
2.3.1 SU-8 Bonding Process 24
2.3.2 Anodic Bonding Process 27
2.3 Fluidic Interconnection 30
2.4 Gas Flow Test 32
2.5 Results and Discussion 33
2.6 Summary 38

CHAPTER 3 40
DEVICE DESIGN AND MODELING 40
3.1 Introduction 40
3.2 Theory: Separation Nozzle Method 40
3.2.1 Equilibrium Separation 41
3.2.2 Diffusion Processes 43
3.3 Design of Separation Element 44
3.4 Computational Fluid Dynamics Modeling 47
3.4.1 Governing Equations 48
3.4.2 Boundary Conditions 50
3.4.3 Solution Method 51
3.4.4 Results 53
3.5 Summary 61

CHAPTER 4 62
DEVICE FABRICATION 62
4.1 Introduction 62
4.2 Processing 65
4.2.1 Wafer Cleaning 65
4.2.2 Photolithography 67
4.2.3 Reactive Ion Etching 68
4.2.4 Deep Reactive Ion Etching 71
4.2.5 Anodic Bonding 73
4.2.6 Packaging and Mounting 75
4.3 Summary 76

CHAPTER 5 77
DEVICE CHARACTERIZATION 77
5.1 Introduction 77
5.2 Gas Separation Experiment 77
5.2.1 Experimental Setup 78
5.2.2 Mass Flow Test 79
5.3 Mass Spectrometric Gas Analysis 82
5.3.1 Principle of Mass Spectrometry 82
5.3.2 Evaluation of Mass Spectra 84
5.3.3 Experimental Setup 85
5.4 Results and Discussion 87
5.4.1 Characterization of Separation Effect 87
5.4.2 Evaluation of Device Performance 94
5.5 Summary 95

CHAPTER 6 97
CONCLUSION 97
6.1 Introduction 97
6.2 Summary of Current Research 97
6.3 Future Work 99

APPENDIX A 103
BASIC THEORY OF COMPRESSIBLE FLUID FLOW 103
A.1 Introduction 103
A.2 Compressibility 103
A.3 Fundamental Principles and Aspects of Compressible Flow 104
A.4 Convergent-Divergent Nozzle 106
A.5 Summary 109

APPENDIX B 110
EQUILIBRIUM SEPARATION NOZZLE FLOW 110
B.1 Introduction 110
B.2 Equilibrium Separation Process 110
B.3 Equilibrium Bifractional Splitting 112

B.4 Summary 114

APPENDIX C 115
AUTOMATED PRESSURE MEASUREMENT SETUP 115
C.1 Introduction 115
C.2 Computer Setup 115
C.3 LabVIEW 119
C.4 Summary 122

APPENDIX D 123
ELECTRONIC NOSE TECHNOLOGY 123
D.1 Introduction 123
D.2 Caltech Electronic Nose 124
D.3 Comments and Summary 127

BIBLIOGRAPHY 128

List of Tables

Table 2.1: Design parameters of two different linear nozzles…….…….17

Table 2.2: Typical examples and evaluation results of SU-8 bonding tests…….……26

Table 3.1: Geometric parameters of three designed separation nozzles (adapted from [33] and [37])…….…..47

Table 4.1: Process parameters of the STS DRIE system..…….……...72

Table 5.1: Geometric parameters of three designed separation nozzles (repeat of Table 3.1 for convenient reference)……..……..…81

List of Figures

Figure 1.1: Schematic of a gas chromatograph along with a photograph of the separation column (adapted from [14])...……..……...…….……5

Figure 1.2: Scanning Electron Micrograph (SEM) of a preconcentrator consisting of a thick micromachined Si heater and graphitized carbon beads as adsorbents [17] ....…….…….……...……...6

Figure 1.3: The selectively permeable membrane is strong enough to hold the differential pressure and allows selected gases to travel through it faster than others....…….…….……..……...……...7

Figure 1.4: Schematic diagram of a slit-type separation nozzle (adapted from [23])……9

Figure 1.5: SEM micrograph of a 390μm thick silicon chip perforated by DRIE [33]……10

Figure 2.1: Principle of single-stage separation nozzle element. The gas mixture is divided into a light fraction stream depleted in SF_6 and a heavy fraction stream enriched in SF_6 after the separation process……14

Figure 2.2: Schematic of a linear nozzle with upstream, downstream and throat pressure measurement chambers……16

Figure 2.3: Design parameters of the linear nozzle. The exit gas flow speed is mainly determined by the expansion ratio of D_2/D_1 of the contoured nozzle……..17

Figure 2.4: Isentropic and non-isentropic flow regions in a C-V nozzle (adapted from [37])……..18

Figure 2.5: Variation of expansion ratio and pressure ratio with Mach number……19

Figure 2.6: ANSYS/FLOTRAN meshed FEA model with applied boundary conditions……...…...21

Figure 2.7: Mach number contour of gas flow in the designed C-V nozzle with an inlet-to-outlet pressure ratio of 8……..22

Figure 2.8: Pressure distribution of gas flow in the designed C-V nozzle with an inlet-to-outlet pressure ratio of about 8……23

Figure 2.9: Process flow for the fabrication of linear micronozzle using SU-8 bonding…….24

Figure 2.10: Optical micrographs of sealed nozzle structure using SU-8-5 intermediate layers at different bonding temperatures: (*a*) 48 °C; (*b*) 55 °C and 75°C……..27

Figure 2.11: Schematic of silicon-to-glass anodic bonding apparatus (adapted from [46])……..28

Figure 2.12: Process flow for the fabrication of linear nozzles using silicon-to-glass anodic bonding…….29

Figure 2.13: Photograph of a microfabricated chip using silicon-to-glass anodic bonding. The holes are the pressure measurement ports etched through in silicon using DRIE……...30

Figure 2.14: Schematic diagram of micro-to-macro interconnection……...31

Figure 2.15: Photograph of a packaged nozzle connected with Tygon flexible tubing……32

Figure 2.16: Gas flow test setup for testing linear micronozzles. It consists of manometers, a flow controller and flow meters connected with the MEMS device through flexible tubing and fittings…….....33

Figure 2.17: A comparison between SU-8 bonding and anodic bonding devices for gas flow rates with increasing regulator pressures: (a) SU-8 bonding nozzle; (b) anodic bonding nozzle……..34

Figure 2.18: (a) Comparison of mass flow rate between the model predictions and measurements for design 1; (b) effects of the Reynolds number on the coefficient of discharge of the gas flow……...35

Figure 2.19: Effects of inlet pressure on the coefficient of discharge for the two designs……..36

Figure 2.20: Comparison of measured and calculated throat pressure as a function of inlet pressure……37

Figure 2.21: Effect of downstream pressure P_b on the mass flow rate. The inlet pressure P_0 is kept at one atmosphere while the downstream pressure P_b varied……....37

Figure 3.1: Schematic of the single-stage separation nozzle system and close-up of the separation element with the critical design parameters……45

Figure 3.2: Computational domain used for the numerical model…….50

Figure 3.3: Finite element mesh for the model geometry. …….52

Figure 3.4: Simulated flow field in the device at pressure ratio of 1.75…….54

Figure 3.5: Second flow mode in the device at pressure ratio of 2…….55

Figure 3.6: Pressure distributions in the flow field for three different pressure ratios: (a) 1.75, (b) 2.0, and (c) 2.5……...57

Figure 3.7: Mass flux distribution of SF_6 (a) and N_2 (b) for the pressure ratio of 2.0…….58

Figure 3.8: Variation of separation factor with pressure ratio for the two flow modes……...60

Figure 3.9: Residence time of gas flow in the device as a function of pressure ratio…61

Figure 4.1: Fabrication process for single-stage separation nozzle including microfluidic interfacing……66

Figure 4.2: Double-sided alignment scheme (adapted from [56])……..69

Figure 4.3: Depth measurements of etched structures as a function of time……..70

Figure 4.4: Optical micrograph of an etched separation nozzle before stripping the photoresist mask……...71

Figure 4.5: AFM micrograph of a device wafer surface before anodic bonding……74

Figure 4.6: EVG501Bonder used for silicon-to-glass anodic bonding……...74

Figure 4.7: Optical micrograph of a microfabricated chip after silicon-to-glass anodic bonding with a close-up view of a single-stage separation nozzle……..75

Figure 4.8: View of mounted chip on the test setup……...76

Figure 5.1: Schematic of setup for gas separation experiments……..78

Figure 5.2: (a) Photograph of a stainless miniature sample cylinder with two stainless bellow valves connected at both ends; (b) the assembly is attached to the setup for gas separation experiments……...79

Figure 5.3: Measured mass flow percentage of heavy fraction compared with model calculations for devices 1 and 2 with different f/r_0 ratios, 1/6 and 1/3, respectively……...80

Figure 5.4: Simulated residence time versus pressure ratio in comparison with the estimate from the mass flow measurements…….81

Figure 5.5: Operating principle of a quadrupole mass spectrometer (adapted from [55])……..83

Figure 5.6: (a) Principle of the Faraday cup; (b) Photograph of a flanged-mounted Faraday cup [64]……...84

Figure 5.7: Standard mass spectrum of SF_6 (adapted from [66]). Six fragments (i.e., masses 127, 89, 108, 129, 51, and 70) are of significant intensity and counted to evaluate the ion abundance of SF_6……..85

Figure 5.8: Setup for mass spectrometric gas analysis. The sample cylinder is connected to the vacuum chamber through a 1-μm orifice to control the gas flow, so the vacuum can be maintained on a desirable level for effective electron ionization……..86

Figure 5.9: The six strongest fragment peaks of SF_6 are shown properly after manually calibrating the mass spectrometer……86

Figure 5.10: Comparison of mass spectra of (a) SF_6 and (b) N_2 between the heavy fraction stream and light fraction stream. Noticeable enrichment of SF_6 is achieved in the heavy fraction, as seen from the increased total ion abundance of the SF_6 fragments while N_2 is kept the same as indicated by the ion abundance of main N_2 fragments (i.e., masses 14 and 28)……...88

Figure 5.11: Comparison of the experimental determinations of the separation factor with the predictions of the analytical and numerical……..……..89

Figure 5.12: Separation factor A of the mixture of 99 mole % N_2 and 1 mole % SF_6 versus pressure ratio for the three designed devices……90

Figure 5.13: Separation factor A of an H_2/C_7F_{14} mixture (95 mole% H_2 and 5 mole% C_7F_{14}) versus Reynolds number Re for various normalized widths a/r_o of the standard separation nozzle (adapted from [24])……91

Figure 5.14: Comparison of mass spectra of (a) SF_6 and (b) Ar between the heavy fraction stream and light fraction stream using the gas mixture SF_6/Ar. SF_6 is enriched in the heavy fraction, as indicated from the increased total ion abundance of the main SF_6 fragments and decreased abundance of the main Ar fragments (i.e., masses 20 and 40)……..93

Figure 5.15: Variation of separation factor A of mixtures N_2/SF_6 and Ar/SF_6 as a function of pressure ratio for devices 1 and 3……94

Figure 6.1: Schematic of a multi-stage separation nozzle system……100

Figure 6.2: Conceptual schematic of the main modules of the proposed on-chip chemical detection system…….……101

Figure A.1: A converging-diverging nozzle with two cross sections A_1 and A_2……104

Figure A.2: Flow in a convergent-divergent nozzle (adapted from [38])……..107

Figure B.1: Influence of the peripheral Mach number Ma_m (r_0) and the SF_6 molar fraction N_h (r_0) upon the elementary effect of the mixture separation (A*-1) for an isothermal cylindrical flow of N_2/SF_6 mixture……113

Figure C.1: Block diagram for the NI-PCI6034E data acquisition device card [76]……117

Figure C.2: Pin assignment on the NI-PCI6034E DAQ card [76]……118

Figure C.3: The data logger after modifying the data viewer program……120

Figure D.1: Swelling occurs as vapor molecules enter the polymer. An increase in the electrical resistance of the film is caused by the vapor-induced film swelling (adapted from [92])……125

Figure D.2: A linear response of an individual sensor signal as a function of concentration is observed for a variety of analytes (adapted from [92])……126

CHAPTER 1

INTRODUCTION

1.1 Introduction

Microelectromechanical Systems (MEMS) have evolved from the fabrication technology used for microelectronic devices to the enabling technology to integrate mechanical elements, sensors, actuators, and electronics to realize system-on-a-chip (SOC). Microfluidics, one of the major application areas in MEMS technology, is a collection of processes for moving fluid (gas or liquid) or controlling the paths of selected particles, cells or molecules, in flows [1]. Microfluidic devices allow us to process and analyze minuscule amounts of samples and reagents in the nano or pico liter range [2]. Furthermore, microfluidics has the potential to revolutionize the processes and products that manipulate fluids by scaling down their dimensions and introducing high-level integration, the impact of which can be as profound as that of integrated circuit (IC) technology. Therefore length scale matching between the fluid flow and the device is the key for realizing efficient momentum and energy transfer for specific applications. The most important advantages of miniaturizing fluidic system are increased assay speed, reduced reagent and power consumption, and integration of different functions on a single chip. With properly designed and engineered microfluidic devices, molecules can be precisely manipulated by the flow patterns inside the device, which provides a pathway to explore the micro and nano world [1].

Microfluidics can be applied to miniaturization of chemical and biochemical instrumentation, which has made enormous progress over the past years since the

pioneering work of *Manz et al*. and *Harrison et al*. [3, 4]. Nowadays many technologies known to work in the macroscopic world in these fields have been successfully miniaturized. The development of microfluidic devices that miniaturize the conventional, general-purpose chemistry laboratory onto a single chip (lab-on-a-chip) has become widespread in the chemical, biochemical and biological research field. For example, micro total analysis systems (μTAS) have served to run chemical microreactors (*Srinivasan et al*. 1997) [5], to perform capillary electrophoresis assays (*Simpson et al.* 1998) [6], and to probe red blood cell rigidity (*Brody et al*. 1995) [7].

1.2 Motivation and Background

On-site identification and quantitative analysis of volatile and semi-volatile chemical vapors are critical for environmental monitoring. Currently, detecting chemical vapors relies on labor-intensive and costly sample collection and laboratory analytical methods, which limits the quality, quantity, and frequency of data to be analyzed [8]. This situation therefore demands the development of portable and/or handheld instruments that can be used for real-time or near real-time detection and analysis of air pollutants, toxic releases or even chemical warfare agents.

Chemical sensors have been downsized over the past years due to advances in MEMS technology and microelectronics. Miniaturized chemical sensors have such advantages as fast response, low power consumption and measurement of small flows. However, many of the sensors are for single gases and are applied for niche applications. Universal chemical sensing systems have either consisted of banks of the individual gas

sensors or are large laboratory based units, such as mass spectrometers and gas chromatographs.

Taylor et al. [9] and *Freidhoff et al.* [10] developed a miniature quadrupole mass spectrometer (QMS) in which the conventional rod arrangement has been replaced with a microengineered version. The structure is made in silicon, using MEMS fabrication techniques, with metallized specially drawn glass fibers to act as the quadrupole rods. This is about one order of magnitude smaller than most conventional QMS filters, with the potential for further reduction in size. It achieves parts per million (ppm) single scan sensitivities with a high scan speed (i.e., a few seconds). The performance is better than that of some large commercial laboratory based mass spectrometers. However, the sensitivity is still recognized to be too low for many applications such as cargo and personnel monitoring at commercial airports and seaports. The sensitivity enhancement required for such applications is about 100 to 1000 times greater than ppm level, so that gas sensors can detect traces of volatile and semi-volatile chemical vapors at the parts per billion (ppb) levels in air during a short time period. With improvements in gas concentration techniques and detector electronics, ppb and sub-ppb levels of sensitivity should be achievable.

1.3 Literature Review

1.3.1 Common Sensitivity Enhancement Techniques

There are a number of approaches used to increase the sensitivity of chemical sensors: gas chromatography, preconcentration through thermally cycled, absorbent materials, cryogenic accretion of materials on a surface, or the use of selectively

permeable polymer diaphragms [11-14]. All of these techniques achieve the increase of sensitivity, but significantly increase the time between measurements or the response time of the system. Gas chromatography uses differences in surface affinity and mass to separate mixtures entrained in a carrier gas and typically takes from 2 to 20 minutes per sample. Both the thermally cycled absorbents and the cryogenics require time to accumulate the amount of material from the air passing through the system before desorbing the collected material into the sensor. Therefore, time is needed to pass enough of the material through the system. The selectively permeable polymers work by allowing selective chemicals to dissolve into them, pass through and be desorbed on the sensor side due to a vacuum pump. The polymer has a time constant for absorption and desorption that slows the system down and can possess a memory of chemicals even after they have dissipated. In addition, these front-ends involve the use of additional power or consumable materials, such as cryogens. These concentration techniques are briefly discussed below.

A. Gas Chromatography

Gas chromatography acts as a chemical separator. Figure 1.1 shows a schematic diagram of gas chromatograph with a photograph of the separation column [15]. A gas sample is transported through the column via a carrier gas such as helium. The column is a stainless steel coil (typically 1-5 m total length and 5 mm inner diameter) that is filled with the high-surface-area inorganic or polymer packing such as polysiloxane. The gaseous species are separated by their size, and retention due to adsorption on the packing material. Detection is accomplished at the end of the tube as each constituent

passes by, usually by measuring the gas's thermal conductivity. Gas chromatographs have been miniaturized using micromachining techniques [8, 16]. Pressure-tuned separations of vapor mixtures have been demonstrated in a few minutes.

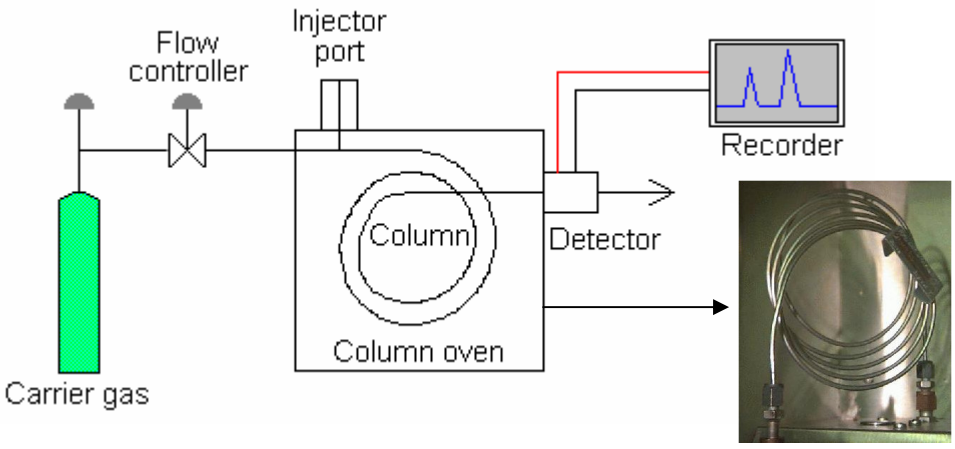

Figure 1.1: Schematic of a gas chromatograph along with a photograph of the separation column (adapted from [15]).

B. Sorbent Beds

Conventional sorbent bed preconcentrators normally consist of a long glass capillary tube packed with one or more adsorbent materials [17]. They adsorb in one direction and desorb in the other. A current is passed through a metal wire coiled around the glass tube to heat the preconcentrator to 200 °C for desorption. The thermal desorbers used for preconcentrator are large, cumbersome and require several watts of power. *Tian et al* [18, 19] developed single-stage and multiple-stage microfabricated preconcentrator-focusers for the microscale gas chromatograph mentioned above. As shown in Figure 1.2, it consists of a thick micromachined silicon heater packed with a small quantity of a

granular adsorbent material (i.e., roughly spherical granules of a high-surface-area, graphitized carbon). Upon thermal desorption efficient separation has been achieved.

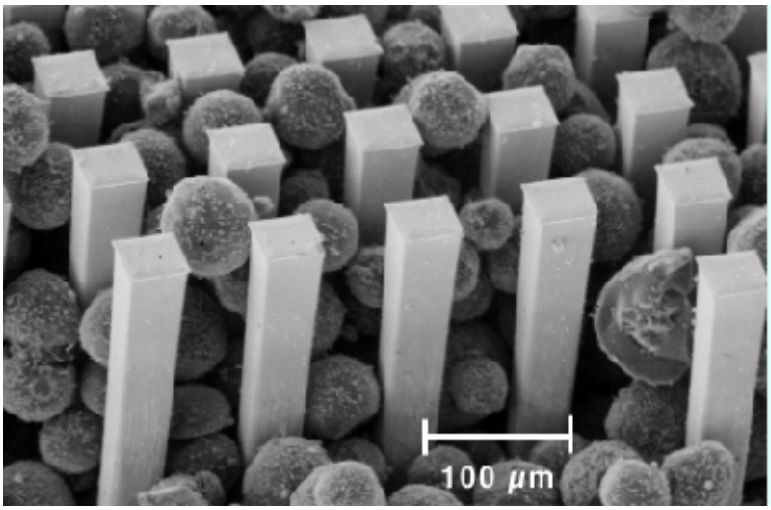

Figure 1.2: Scanning Electron Micrograph (SEM) of a preconcentrator consisting of a thick micromachined Si heater and graphitized carbon beads as adsorbents [17].

C. Selectively Permeable Membranes

Selectively permeable membranes are also used to improve sensitivity as front-ends for chemical sensing systems. The concept is shown schematically in Figure 1.3. There are polymeric films that allow the passage of different gases due to the differences in the solubility and diffusion of chemicals into the films themselves [20, 21]. The use of polymeric membranes as a selective barrier does not increase the power needed by the system, but does affect the response time of the sensing due to the "reservoir" effect of the polymer film (i.e., adsorption and desorption of gas molecules).

There are a number of polymers in commercial use for different families of gases. The polymers consist of polyvinylchloride, polystyrene, polyethylene, polydimethylsiloxane and polytrimethylsilylpropyne, as well as others. These polymers

restrict the passage of oxygen and nitrogen. The propynes show a permeation of organic molecules while being able to exclude nitrogen and oxygen. The permeation of vapors depends on the solubility of the vapor into the material and the diffusion constant of the vapor within the material; so polymers that do not dissolve oxygen or nitrogen will be effective barriers to these gases. The disadvantage is that the time constant of the polymer membrane will determine the amount of time that the sensor needs to be in the area before a true determination of the quantity of a vapor can be determined.

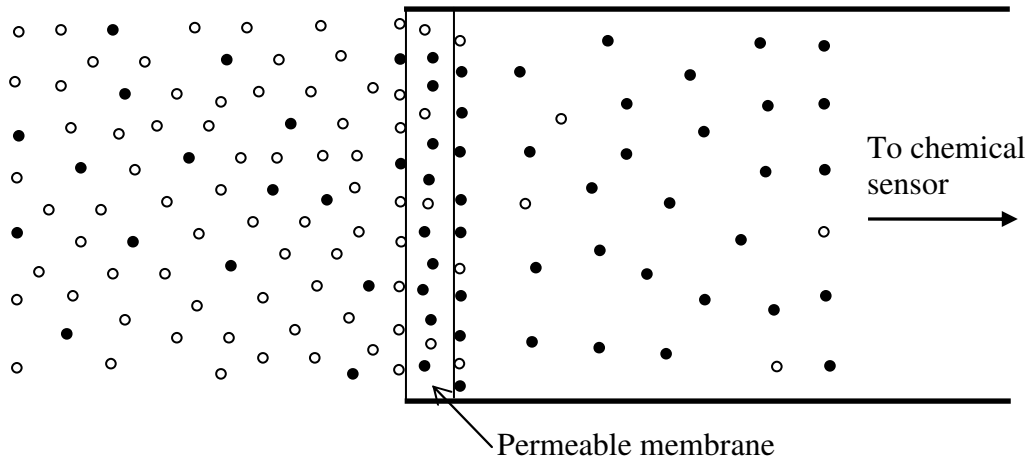

Figure 1.3: The selectively permeable membrane is strong enough to hold the differential pressure and allows selected gases to travel through it faster than others.

1.3.2 Separation Nozzle Method for Isotope Separation

To maintain the system time constant, a preconcentrator that can separate the minor constituents of the gas mixture from the major ones while the gas is flowing at a high speed would be ideal. There is such a technique, referred to as the separation nozzle method, which can concentrate heavier molecules from lighter molecules as long as the heavier ones make up a small fraction of the gas molecules in the vapor mixture.

The separation nozzle method was developed as an alternative method to the gaseous diffusion and centrifuge processes to enrich the light uranium isotope ^{235}U for production of light water reactor fuel [22-25]. This method was characterized by simple technology and the possibility of economic operation. In the separation nozzle process, the pressure gradients and inertial forces in a curved gas flow containing uranium as UF_6 are utilized for separating the uranium isotopes.

This separation principle was first proposed by Dirac for enriching ^{235}U [24] in the early forties. Nevertheless, the results from initial tentative experiments performed on model gas mixtures like pure UF_6 were not very promising: The elementary effect of isotope separation was only very little above of the gaseous diffusion method, which made technique application of such arrangements hardly practical. It was until the early sixties that Becker *et al* achieved the breakthrough in the technology development of the separation nozzle. In their work, a mixture of UF_6 and a light auxiliary gas in a high molar excess, instead of pure UF_6, was used [26] and free expansion was replaced by a guided deflection of the flow along a curved wall [27]. Through these measures, a much higher flow velocity and greater deflection of the flow than in the free expansion of pure UF_6 were achieved. Consequently, the elementary effect of uranium isotope separation was enhanced significantly above that of the gaseous diffusion process, while simultaneously reducing the pressure ratio required for economic operation of the separation nozzles. This revolutionary technology innovation helped reduce the technical expenditure for industrial uranium enrichment by the separation nozzle method to an economically attractive levels [28, 29]. Practical implementation of the separation nozzle method has been fulfilled successfully to enrich the light uranium isotope.

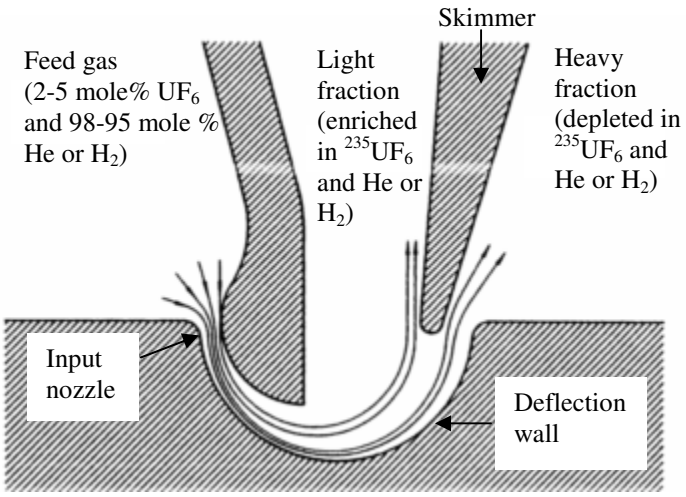

Figure 1.4: Schematic diagram of a slit-type separation nozzle (adapted from [24]).

Figure 1.4 is a cross section of a slit-type separation nozzle. A gas jet containing 2 to 5 mole % of UF_6 and 98 to 95 mole % of H_2 or He is deflected at a fixed curved wall and expanded to roughly half the value of the nozzle inlet pressure, the heavy components of the mixture being concentrated at the deflection wall and the light ones in the inner regions of the flow. At the end of the deflection, the partly separated gaseous mixture is split by a skimmer into a heavy fraction depleted in $^{235}UF_6$ and the auxiliary gas, and a light fraction enriched in $^{235}UF_6$ and the auxiliary gas.

Small size gas separation nozzles were fabricated with stacking of photo-etched metal foils, diamond tool machining, or the LIGA (LIthographic generation in polymer layers that serves as molds for GAlvanoplastic metal deposition) process at the Karlsruhe facility [22]. The work demonstrated that the separation nozzle could operate very efficiently at sub-atmospheric pressures, which is ideal for the miniature chemical sensors such as mass-spectrograph-on-a-chip [10], since no compressor stage would be required. However, the high cost operation and access to specialized equipment X-ray synchrotron

source limit the availability of the LIGA process. A lot of work has been done on developing alternatives to the LIGA process [30-34]. Among these techniques more advances have been achieved in thick photoresist process and deep silicon etching. Figure 1.5 [34] shows a silicon chip with through holes created by deep reactive ion etching (DRIE). MEMS-based devices and microsystems with high-aspect-ratio microstructures have been developed using these techniques for various applications. However, these microfabrication methods have not been explored extensively to develop gaseous microfluidic devices, especially miniature separation nozzle systems.

In the past, nozzle performance at small scale was studied on a few occasions. *Rothe et al.* reported E-beam measurements of temperature and velocity profiles in a nozzle with a 5 mm throat [35]. *Grisnik et al.* investigated nozzles with throat diameters on the order of 650 µm [36]. Each of these test cases was machined through conventional macro-scale fabrication methods and was orders of magnitude larger than what is now

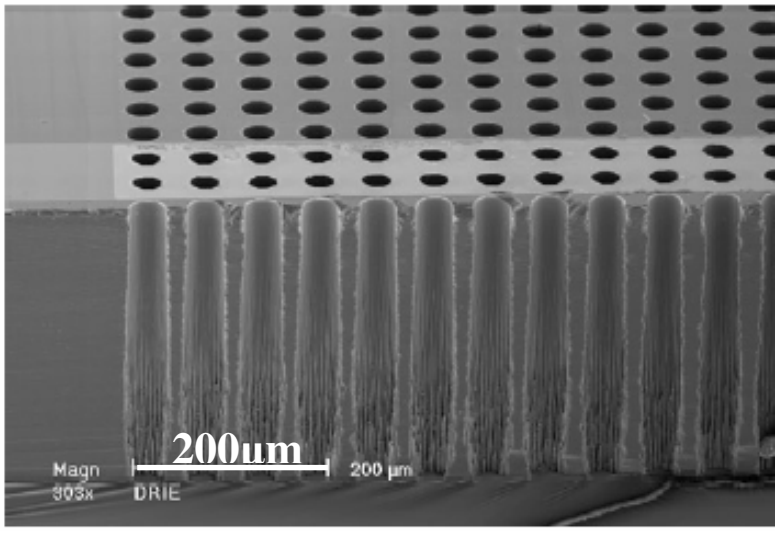

Figure 1.5: SEM micrograph of a 390µm thick silicon chip perforated by DRIE [33].

available through MEMS. In addition, *Bayt et al.* studied viscous effects in supersonic MEMS-fabricated micronozzles, but their research was targeting micropropulsion applications [37]. In this work, we are exploring the separation nozzle method for gas sensing applications.

1.4 Objectives

The primary objective of this thesis research is to develop a fast-response microfluidic gas separation device for environmental sensing applications. Initial studies are performed to analyze the trade-offs with scaling down devices, and assess the limitations associated with microfabrication. These limits are used as a guide to the design of single-stage separation device, serving as the elementary unit of a real-time MEMS-based preconcentrator. This research studies the separation process in the microfluidic gas separation device theoretically through analytical models and computational fluid dynamics (CFD) simulations and experimentally through the gas separation experiments and mass spectrometric gas analysis. The measurement results along with theoretical studies not only form the basis of developing a real-time preconcentrator but also provide important guidelines for designing, fabricating and testing other microfluidic devices for chemical sensing applications.

1.5 Contributions

The analysis and results described herein make the following contribution to the field of MEMS-based concentration techniques:

- A fast-response (i.e., less than 0.1 ms compared to several minutes or more for other commonly used techniques) gas concentration concept has been demonstrated with conventional MEMS techniques and mass spectrometric gas analysis.
- Fundamental fluid dynamics of gas flows in micro-scale converging-diverging nozzles is studied to examine the viscous effect of the microfluidic devices. Mass flow efficiency (i.e., the ratio of the actual mass flow to the theoretical frictionless mass flow) of these ultra shallow microfluidic devices has been found in the range of 0.36 to 0.81, exhibiting strong viscous effects.
- Finite element analysis combined with experimental testing has confirmed that sonic gas flows can be realized in microscale nozzles.
- A straightforward two-mask process flow has been developed for fabricating encapsulated microfluidic devices with through-hole inlets and outlets.
- A reliable packaging technique using micro O-rings and capillaries has been developed for micro-to-macro fluidic interconnection.
- The effects of design parameters such as nozzle width and skimmer distance and the operating condition (i.e., inlet-to-outlet pressure ratio) on the performance of gas separation devices have been characterized with CFD simulation, gas separation experiments, and mass spectrometric analysis.
- Experimental results have demonstrated more than two-fold enrichment of SF_6 molecules diluted in N_2 with a response time on the order of 0.01 ms for a single-stage element.

1.6 Thesis Organization

This chapter has introduced background and motivation of this research. Relevant gas concentration techniques have been reviewed. The objectives of this research have been outlined, followed by a summary of the contributions of this work. The remaining chapters of this thesis are organized as follows.

Chapter 2 presents design, fabrication and testing of linear test structures. A one-dimensional isentropic model and an ANSYS finite element analysis of gas flows in micronozzle are introduced, followed by the details on the device packaging and gas flow tests.

Chapter 3 discusses the design considerations of single-stage separation nozzle systems based on the results from the linear structures. Analysis of the separation process is discussed along with a derivation of an equilibrium model. CFD modeling of the separation process is then introduced along with a discussion of simulation results.

In Chapter 4, fabrication of separation devices is detailed, after which device packaging and mounting is presented.

Chapter 5 is devoted to the device characterization with gas separation experiments and mass spectrometric gas analysis. Details about the setup and mass spectrum evaluation are presented. Measurement results are discussed in comparison to modeling results.

Finally, in chapter 6, the accomplishments of this thesis research are summarized, and some recommendations are made for future work.

CHAPTER 2

LINEAR TEST STRUCTURES

2.1 Introduction

In this chapter, linear test structures designed to characterize the viscous effects in microfluidic devices are presented. First, an isentropic model and an ANSYS finite element analysis of gas flows in micronozzles are introduced to describe the behavior of gas flows in linear micronozzles. Next, device fabrication and packaging are discussed. Finally, gas flow tests are presented along with the comparison between the measurements and model calculations.

As with most commonly used separation/concentration techniques, the separation nozzle method is a continuous process in which the mixture to be separated is injected

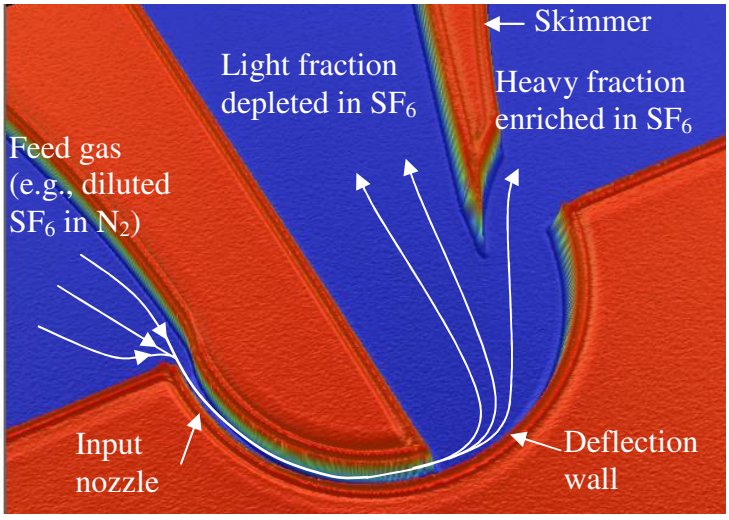

Figure 2.1: Principle of single-stage separation nozzle element. The gas mixture is divided into a light fraction stream depleted in SF_6 and a heavy fraction stream enriched in SF_6 after the separation process.

into a system containing separating elements and then divided into fractions of different compositions [24]. A diagram of a single-stage separation nozzle system is shown in Figure 2.1. The system consists of a curved converging-diverging nozzle, a deflection wall, and a skimmer. When a gas mixture (e.g., SF_6 diluted in N_2) is fed to the device, the components of the mixture are accelerated by expansion in the nozzle and then deflected by the curved channel. The centripetal acceleration associated with the deflection causes a radial pressure gradient and a partial separation of N_2 and SF_6 based on the difference in molecular weight. The heavier SF_6 molecules become concentrated at the periphery of the flow field and a skimmer is used to mechanically separate the stratified gas mixture exiting the curved channel into a heavy fraction, enriched in SF_6, and a light fraction, depleted in SF_6. If the elementary separation process is repeated many times in a cascade arrangement, most nitrogen can be separated from the gas mixture, and SF_6 is concentrated.

2.2 Design of Linear Nozzles

Since the input nozzle is the main component of the gas separation system, it would be useful to study gas dynamics of micronozzles, the fundamentals of which are reviewed in Appendix A. In the first phase of this research, we have designed linear test structures (i.e., linear micronozzles of different dimensions) because their characteristics can be described with sufficient accuracy by analytical models and finite element analysis. Figure 2.2 shows a typical linear micronozzle with pressure measurement chambers. In order to achieve high device performance, the gas must be injected into the nozzle with as low an entrance velocity as possible [37]. To accomplish this, a settling

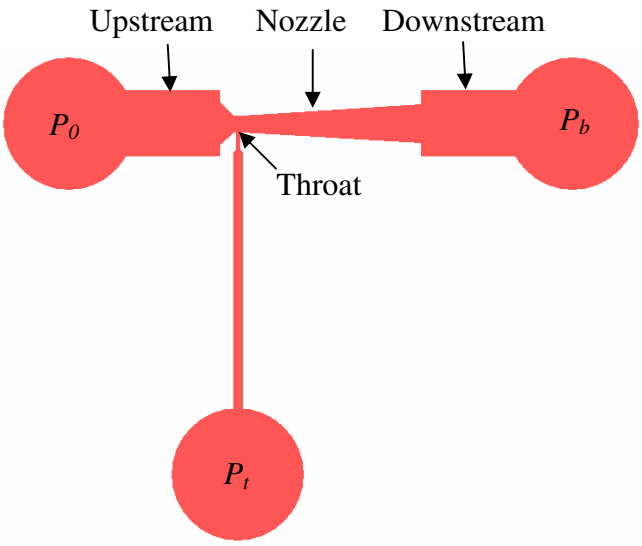

Figure 2.2: Schematic of a linear nozzle with upstream, downstream and throat pressure measurement chambers.

chamber (or plenum chamber) is designed in parallel with and upstream of the nozzle. In addition, a chamber is designed in parallel with and downstream of the nozzle while another is connected to the throat area. These chambers are regions of large volume compared to the nozzle and remain at constant pressures (i.e., P_0, P_d *and* P_t, respectively) during the operation of the nozzle.

Figure 2.3 shows the design parameters of the linear nozzle, which are based on the designed mass flow input of some miniaturized chemical sensors [9, 10]. Table 2.1 shows the dimensions of two designed nozzles that are examined to determine the sizing of the devices to generate fast gas flows for achieving efficient gas separation. These test structures are also used to measure pressure distributions and mass flow variations to characterize viscous effects in the microfabricated devices. The results of this phase can be used to design single-stage separation nozzle systems.

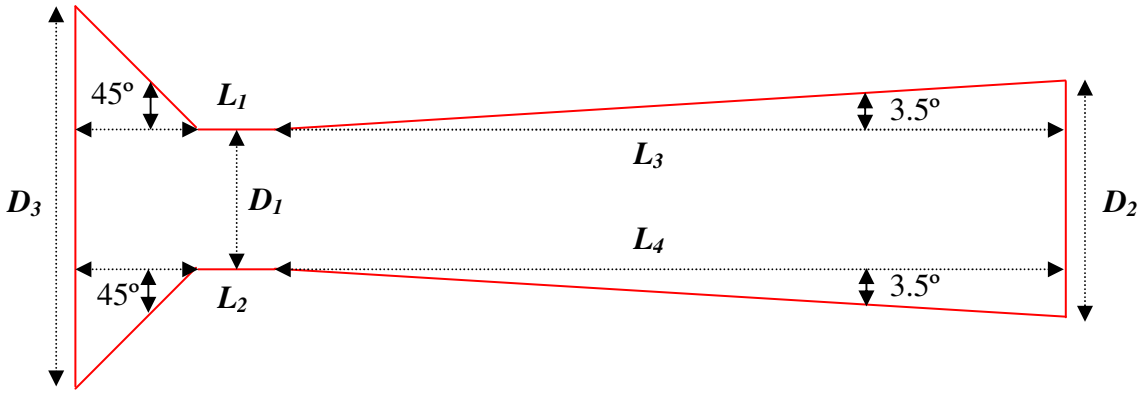

Figure 2.3: Design parameters of the linear nozzle. The exit gas flow speed is determined primarily by the expansion ratio of D_2/D_1 of the contoured nozzle.

Table 2.1: Design parameters of two different linear nozzles.

Design	D_1 (μm)	D_2 (μm)	D_3 (μm)	L_1/L_2 (μm)	L_3/L_4 (μm)	Expansion ratio (D_2/D_1)
1	10.9	18.5	30	6	61.7	1.69
2	36.4	61.6	100	20	205.6	1.69

2.2.1 One-dimensional Isentropic Model

Many of the compressible flows that occur in engineering practice can be adequately modeled by assuming them to be steady and one-dimensional (1-D). Strictly speaking, the equations of 1-D flow are only applicable to flow in a straight pipe or stream tube of constant area. However, in many practical situations, those equations can be applied with acceptable accuracy to flows with a variable area provided that the rate of change of area and the curvature are small enough for one component of the velocity vector to remain dominant over the other two components. For example, although the flow through a converging-diverging nozzle of the type shown in Figure 2.3 is not strictly

one-dimensional, the flow can be calculated with sufficient accuracy in many cases by only considering the variation of the component of the velocity along the nozzle. Such flows in which the flow area is changing but in which the flow at any section can be treated as 1-D, are commonly referred to as "quasi-one-dimensional" flow [38].

An isentropic flow is adiabatic (no heat exchange) and reversible (viscous and other dissipative processes are negligible). Although no real flow is entirely isentropic, there are many flows of great practical importance in which the major portion of the flow can be assumed to be isentropic. In the nozzle flows, the effects of viscosity and heat transfer are restricted to thin layers adjacent to the walls, i.e., are only important in the wall boundary layers, and the rest of the flow can be assumed to be isentropic as indicated in Figure 2.4. Using the 1-D isentropic flow model and applying principles of conservation of mass, momentum and energy, a relationship between the expansion ratio of D_2/D_1 and the Mach number M at the exit of the nozzle with a uniform depth can be derived (the procedure is presented in Appendix A):

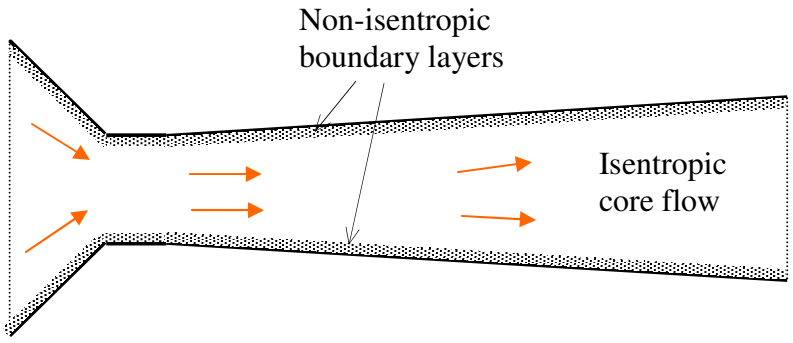

Figure 2.4: Isentropic and non-isentropic flow regions in a converging-diverging nozzle (adapted from [37]).

$$\frac{D_2}{D_1} = \frac{1}{M}\{(\frac{2}{\gamma+1})[1+(\frac{\gamma-1}{2})M^2]\}^{\frac{\gamma+1}{2(\gamma+1)}} \tag{2.1}$$

where D_1 and D_2 are, respectively, the throat width and exit width of the nozzle, and γ is the ratio of specific heats of gas. Similarly, there is a relationship between the inlet-to-outlet pressure ratio and M [38]

$$\frac{p_0}{p_d} = (1+\frac{\gamma-1}{2}M^2)^{\frac{\gamma}{\gamma-1}} \tag{2.2}$$

where P_0 is the inlet pressure (i.e., inlet is assumed to be at stagnation conditions) and P_d is the outlet or downstream pressure. Figure 2.5 shows the variation of the expansion ratio and inlet-to-outlet pressure ratio as a function of M. As indicated in this figure, the

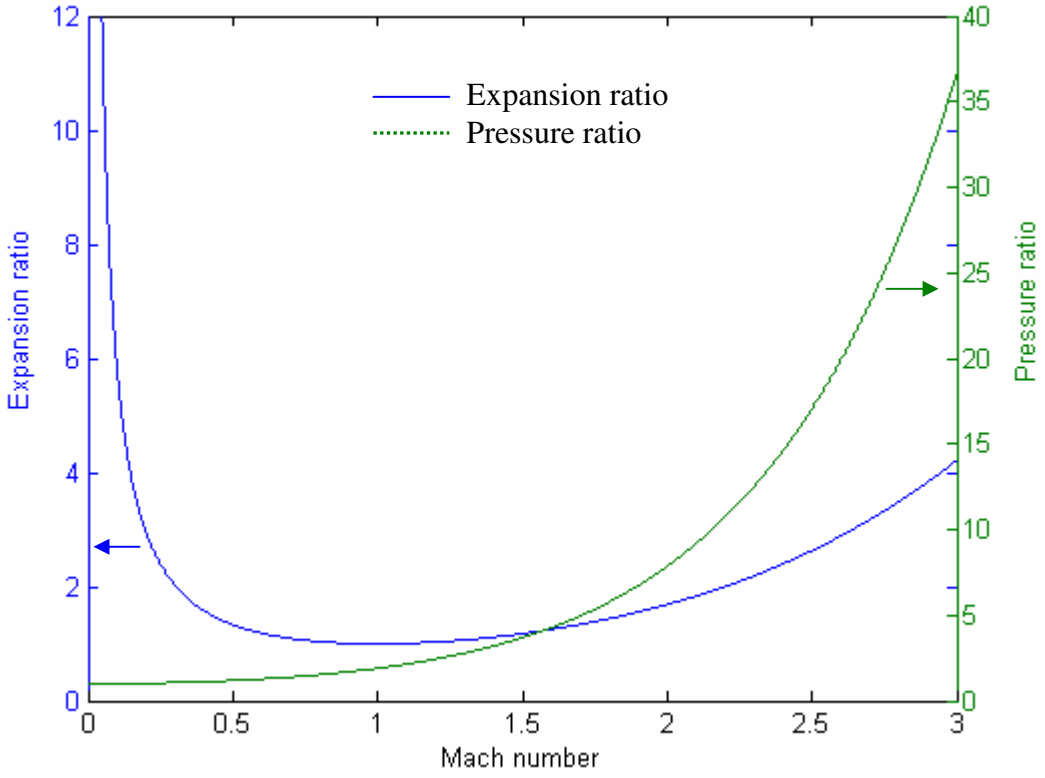

Figure 2.5: Variation of expansion ratio and pressure ratio with Mach number.

expansion ratio of the nozzle should be designed to be about 1.69 with a pressure ratio of around 8 applied across the nozzle if an exit Mach number of 2 needs to be achieved for the gas flow.

2.2.2 Finite Element Analysis

ANSYS/FLOTRAN finite element analysis (FEA) was performed to correct and verify the analytical results (i.e., the 1-D isentropic modeling results). In FEA, a nozzle geometrical flow model is meshed into smaller blocks, or elements. The vertices where these elements meet are termed "nodes". The element chosen to model the compressible flow in a converging-diverging nozzle was ANSYS/FLOTRAN FLUID 141. The 4-node quadrilateral element can be used to solve for two-dimensional (2-D) flow, pressure, and temperature distributions in a single-phase viscous fluid. For this element, the ANSYS program calculates velocity components, and pressure from the conservation of three properties: mass, momentum, and energy [39]. Figure 2.6 shows an FEA model based on the design 1 in Table 2.1 with an expansion ratio of 1.69. This model is used to calculate the pressure and velocity distributions of compressible fluid flow in a nozzle. Figure 2.7 shows the Mach number contour in the nozzle with an inlet-to-outlet pressure ratio of 8 and a reference pressure (i.e., the outlet pressure) of one atmosphere. It is shown that an exit Mach number of 1.929 is achieved, which agrees with the results (i.e., $M = 2$) from the 1-D isentropic model. The Mach number at nozzle throat is about 1, which is characteristic of a supersonic gas flow in a nozzle. In other words, it follows that if a subsonic flow is to be accelerated to a supersonic velocity it must be passed through a convergent-divergent passage or nozzle. The convergent portion accelerates the flow up

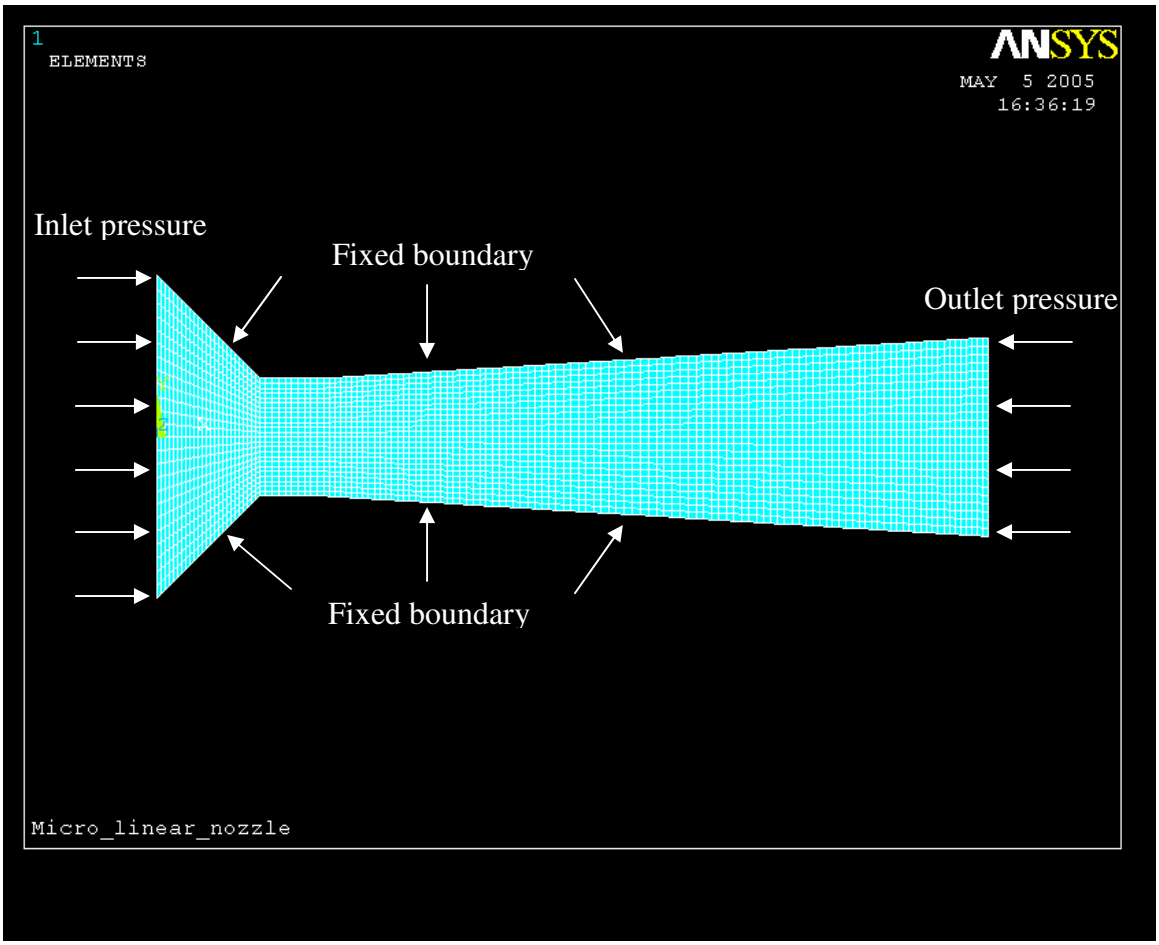

Figure 2.6: ANSYS/FLOTRAN meshed FEA model with applied boundary conditions.

to Mach number of 1 and the divergent portion accelerates the flow to supersonic velocity. The supersonic flow region is normally terminated by a normal shock wave. The shock wave increases the pressure and reduces the velocity to a subsonic value. However, if the inlet-to-outlet pressure ratio is above a critical value (i.e., about 8.0 in this case), the shock wave moves outside the nozzle and the extent of the supersonic flow region increases to the whole divergent region of the converging-diverging nozzle [38].

Figure 2.8 shows the pressure distribution using the same boundary conditions. The throat pressure is evaluated to be around 385.0 kPa above the reference pressure (i.e.,

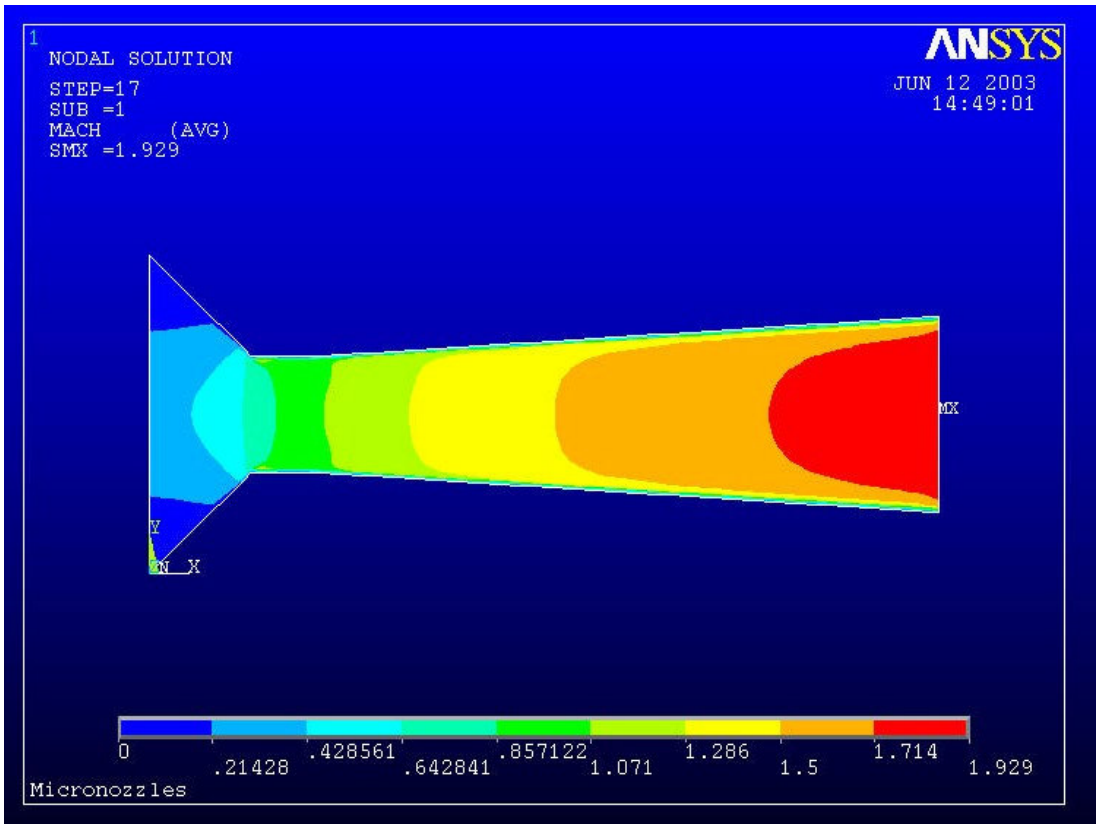

Figure 2.7: Mach number contour of gas flow in the designed C-V nozzle with an inlet-to-outlet pressure ratio of 8.

101.325 kPa). According to the 1-D isentropic model, the throat pressure is 0.528 P_0 [38], which is about 327.0 kPa above the reference. Therefore, FEA results are within 18 % of the 1-D isentropic modeling results. The discrepancy is mainly due to the influence of the device sidewall boundary layers accounted in the FEA.

2.3 Device Fabrication and Packaging

In order to fabricate completely sealed micronozzles for characterizing viscous effects, two different processes with different wafer-level bonding techniques are explored. The first bonding technique is categorized as intermediate-layer bonding. SU-8,

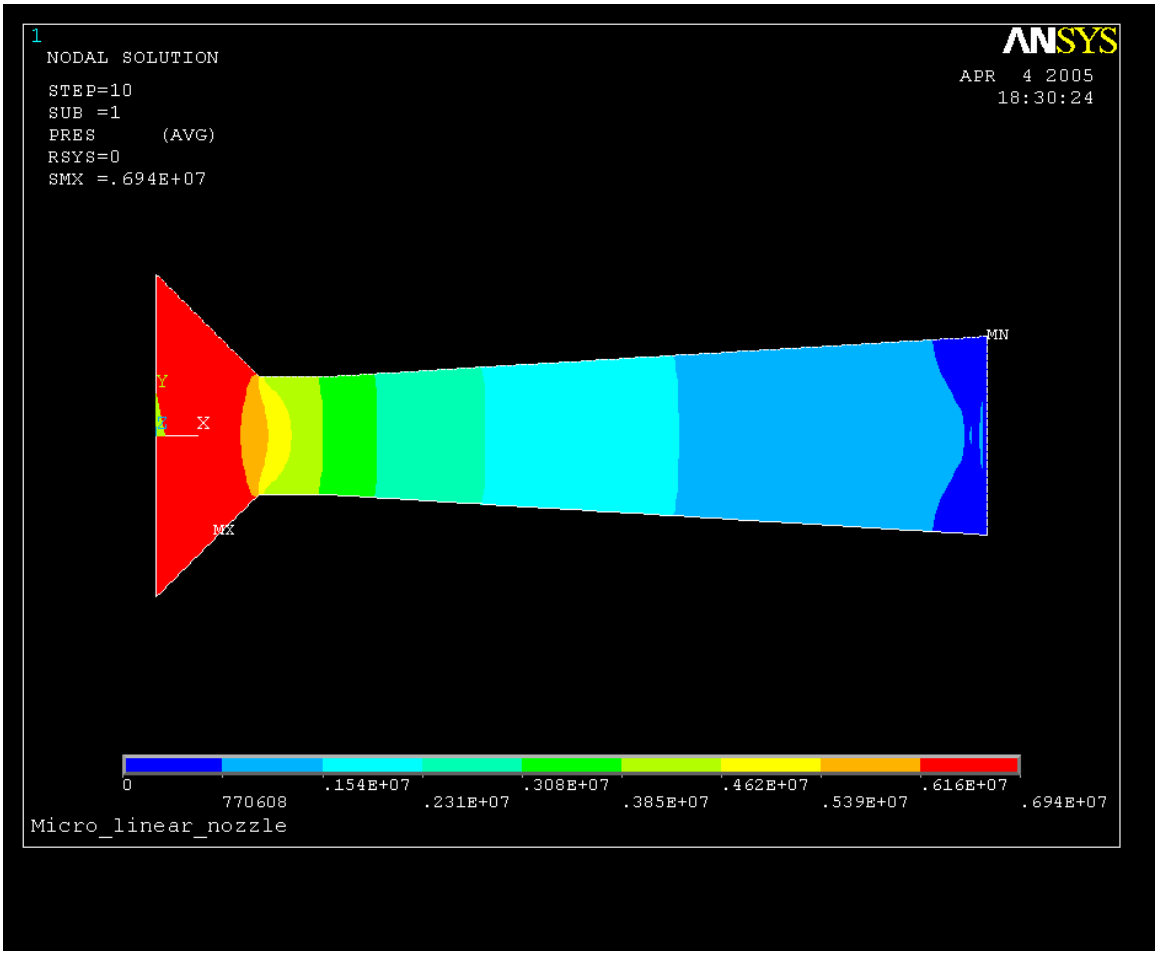

Figure 2.8: Pressure distribution of gas flow in the designed nozzle with an inlet-to-outlet pressure ratio of about 8.

an epoxy based photo-definable polymer, is used as the intermediate bonding layer. SU-8 is selected because it shows low volume shrinkage and high resistance to most wet chemicals after being exposed to ultraviolet (UV) light and a post-exposure bake [40]. The second technique is anodic bonding, which is relatively mature and commonly used in MEMS. The two bonding processes are introduced in the following two sub-sections along with the discussion of the advantages and drawbacks associated with these two methods.

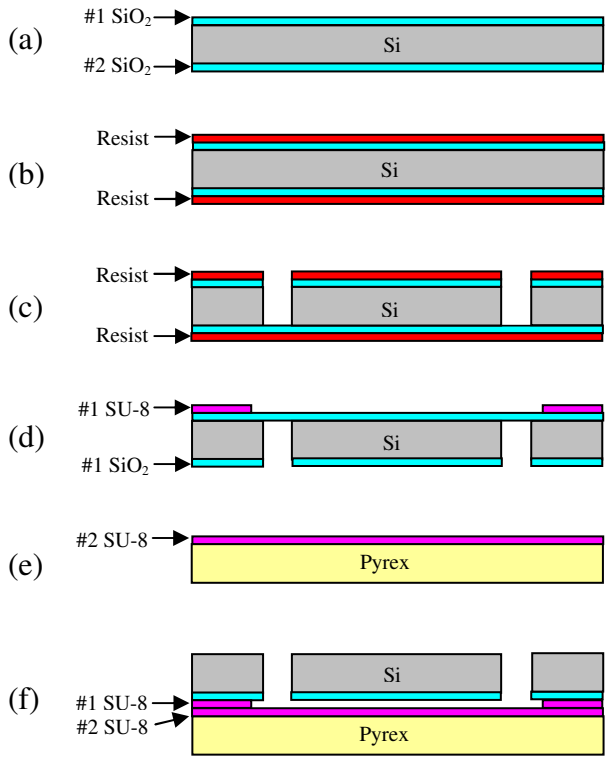

Figure 2.9: Process flow for the fabrication of linear micronozzle using SU-8 bonding.

2.3.1 SU-8 Bonding Process

The process flow is shown in Figure 2.9. The starting material is a silicon wafer with 2 μm thick oxide deposited on both sides (*step a*). Photoresist layers are spun on both SiO_2 layers (*step b*). The backside (unpolished) resist layer is patterned and developed, followed by etching the oxide layer with buffered HF (30-36% Ammonium Fluoride, 4-8% Hydrofluoric acid, and 56-66% distilled water). The combination of resist and oxide is used as the mask for deep reactive ion etching inlet and outlet ports in the silicon substrate (*step c*). After the etch, the resist was stripped, and SiO_2 membranes were formed on the bottom of the ports. Subsequently, a 5-μm thick SU-8

(Microlithography Chemical Corporation) layer is deposited and patterned on the membranes and other oxide areas to create micronozzle structures (*step d*). The SiO_2 membranes are etched away with reactive ion etching (RIE). An SU-8 bonding layer is spun and partially baked on a pyrex wafer (*step e*). The silicon and pyrex wafers are then brought into contact with SU-8 facing SU-8. A blanket exposure through the pyrex wafer followed by a post-bake serve to crosslink and solidify the SU-8 bonding layer (*step f*). Thus, wafer-level bonding is realized to produce sealed micronozzles [41, 42].

Fabricating fully encapsulated micronozzles requireed a selection of wafer-level bonding tests with SU-8 as the intermediate bonding material. The influence of different parameters on the bond quality were investigated. Two methods, direct inspection and crack opening [43], were used to determine the presence of voids and to evaluate the bond strength. The bond interface was first inspected through the transparent pyrex glass wafer to identify the status of sealed nozzles and unbonded areas (including macroscopic and microscopic voids). The crack-opening method consists of splitting two bonded wafers with a razor blade and measuring the equilibrium crack length. This technique is based on the equilibrium of elastic forces of the bent separated part of a pair and bonding forces at the crack tip. The surface energy of the bonded wafers is also evaluated using the crack opening method [43], [44].

Table 2.2 lists the tests performed using different bonding parameters, the resulting unbonded areas, and quantitative evaluations of the bond strength. Figure 2.10 shows sealed linear nozzle structures bonded under three different bonding temperatures (i.e., 48 °C, 55 °C and 75 °C) with 10 μm thick SU-8 bonding layer. The channels were very clear when bonded at 48 °C. Under 55 °C a small amount of SU-8 was found in the

channels while at 75 °C the channels were totally blocked by SU-8. Similar results were found in the experiments using 50 μm thick SU-8 bonding layer. Therefore, it was concluded that SU-8 bonding should be conducted slightly below the glass transition temperature (T_g) of uncrosslinked SU-8 (i.e., 50~55 °C) to prevent SU-8 from obstructing the microchannels. It was also found that introducing an air escape path and applying pressure during bonding could counteract void formation due to outgassing substances and trapped air. In addition, it was observed that the bonding process maintained the dimensions and integrity of the converging–diverging nozzle structures [45]. One potential drawback of SU-8 bonding technique is the relatively low yield of bonded microscale structures. This is mainly due to the voids formed at the bonding interface if bonding is not performed in vacuum. However, this bonding method is relatively simple to implement and less susceptible to particles at the bonding interface than other bonding techniques such as direct bonding. It therefore extends the flexibility of fabricating and packaging microfluidic devices, as evidenced by the published results of developing embedded microchannels which cite this bonding process [46-49].

Table 2.2: Typical examples and evaluation results of SU-8 bonding tests.

No	Material	Layer thickness (μm)	Pre-bake temperature (°C)	Pre-bake time (min)	Bonding temperature (°C)	Post-bake temperature (°C)	Post-bake time (min)	Bond strength (J/m^2)	Amount of unbonded device area (%)	Status of sealed channels
1	SU-8-50[a]	50	95	30	75	95	20	—	90	—
2	SU-8-50	50	95	20	75	95	20	0.55	30	partly blocked
3	SU-8-50	50	95	10	75	95	20	0.56	20	totally blocked
4	SU-8-50[b]	50	95	20	75	95	20	0.42	70	partly blocked
5	SU-8-50	50	95	20	48	95	20	0.51	30	clear
6	SU-8-5	10	95	12	75	95	10	0.55	20	partly blocked
7	SU-8-5	10	95	12	48	95	10	0.43	30	clear
8	SU-8-5	10	95	12	55	95	10	0.44	30	almost clear

[a] Wafers failed to bond together
[b] Without applying pressure using tweezers

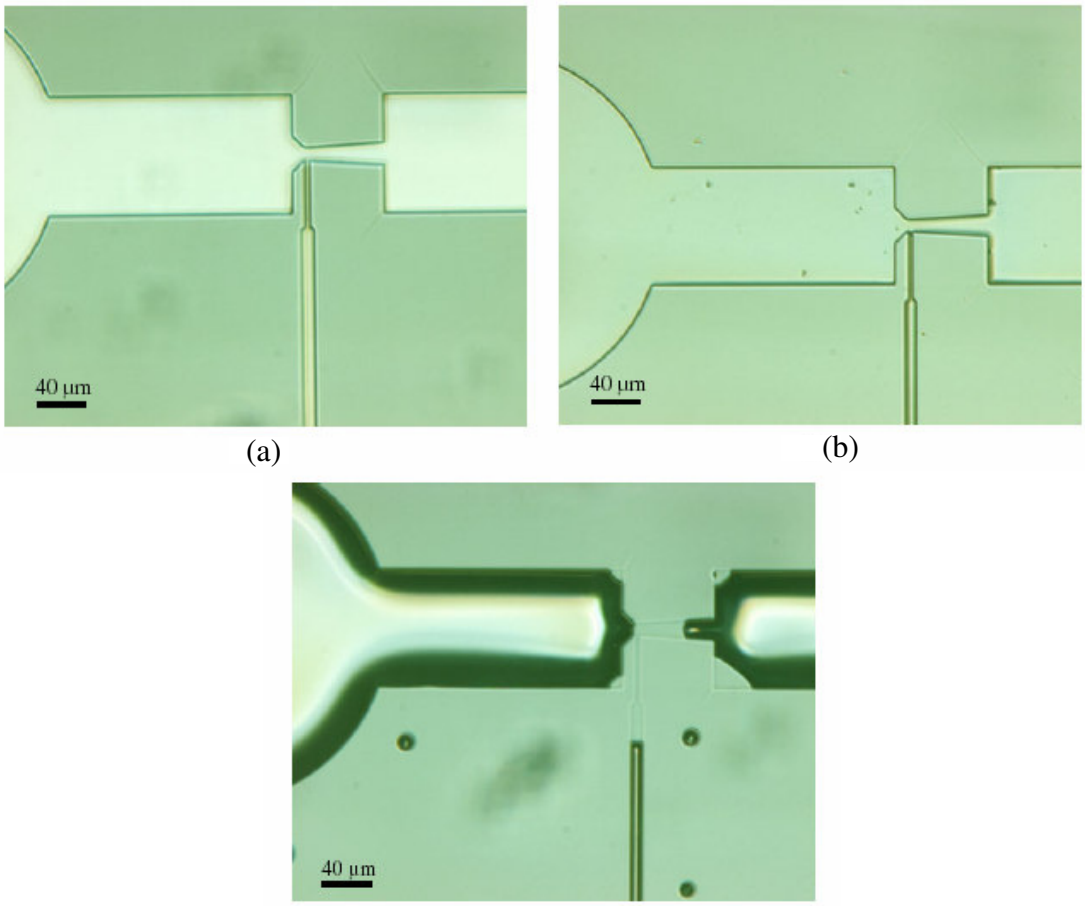

(a) (b)

(*c*)

Figure 2.10: Optical micrographs of sealed nozzle structure using SU-8-5 intermediate layers at different bonding temperatures: (*a*) 48 °C; (*b*) 55 °C and 75 °C.

2.3.2 Anodic Bonding Process

Anodic bonding, a field assisted bonding method, is also used to fabricate micronozzles. Figure 2.11 shows schematically the silicon-to-glass anodic bonding apparatus. The glass wafer is biased as the cathode, and the silicon wafer is the anode. The contacted wafers are heated to 300-500°C while a voltage of approximately 300-700V is applied. Under such a high field and elevated temperature, the mobile sodium ions in the glass migrate away from the bonded interface, leaving behind fixed charge in

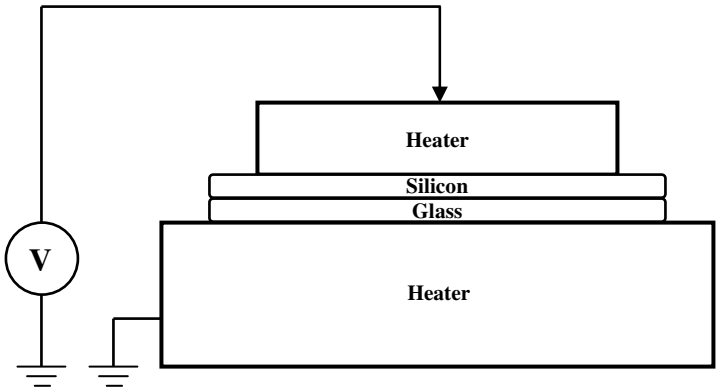

Figure 2.11: Schematic of silicon-to-glass anodic bonding apparatus (adapted from [46]).

the glass that creates a high electric field across the bond interface with image charges in the silicon. The force of attraction between the positively charged silicon wafer and the negatively charged glass surface brings the two surfaces into intimate contact. At the elevated temperature, they can fuse together. Contact is typically initiated at a single point by applying a load, and, as contact is established, it spreads out to cover the rest of the wafer. Bonding time ranges from seconds to minutes and can be monitored by measuring the current in the circuit. When bonding is completed, this current drops to zero. As with silicon-to-silicon direct bonding, this bonding method is very susceptible to interface particulate contaminants [50, 51].

Figure 2.12 shows the process flow for fabricating linear nozzle structures with anodic bonding. The process starts with a silicon wafer with 2 μm thick oxide coated on the backside (*step a*). Reactive ion etching is used to generate linear micronozzle structures on the front side of the silicon substrate (*step b*). Then, a backside (unpolished) resist layer is patterned and developed, followed by etching the oxide layer with buffered HF (*step c*). As in the SU-8 bonding process, the combination of resist and oxide is used

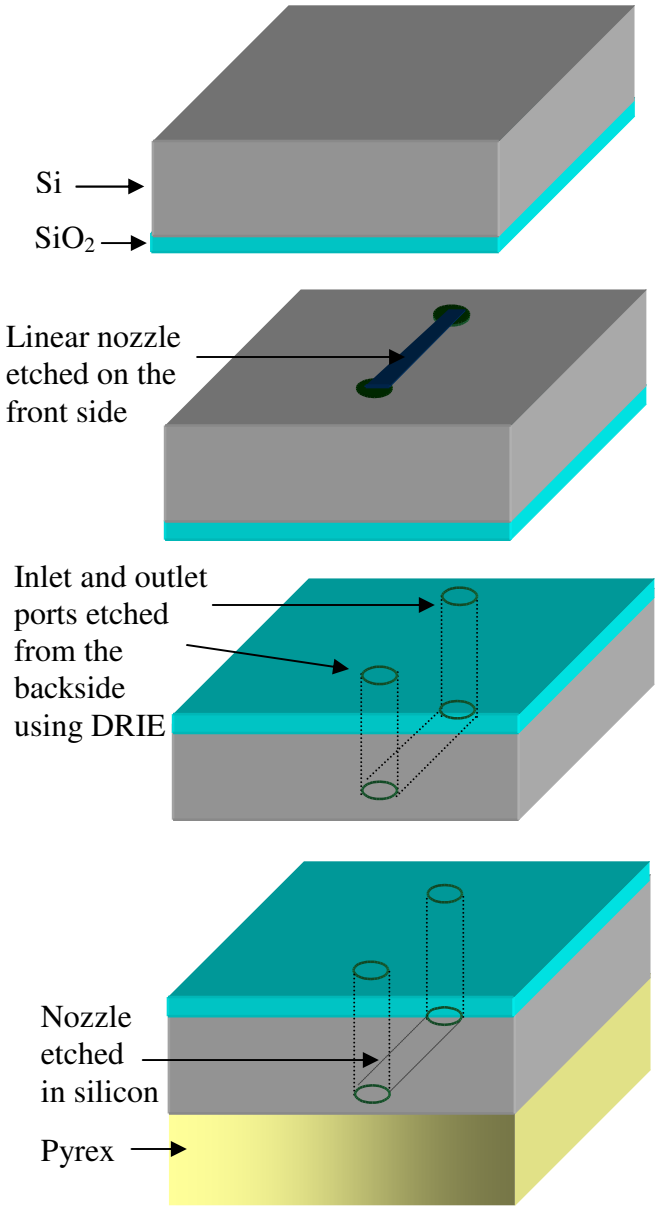

Figure 2.12: Process flow for the fabrication of linear nozzles using silicon-to-glass anodic bonding.

as the mask for deep reactive ion etching inlet and outlet ports in the silicon substrate (*step d*). Finally, the micronozzle structures are sealed using silicon-to-glass anodic bonding (*step e*). This process was done through the collaboration with the Army Research Lab (ARL).

Figure 2.13 shows a microfabricated chip after the anodic bonding. The dark holes shown in the photograph are pressure measurement ports etched through in the silicon substrate using DRIE. The device yield of this process is higher than that of SU-8 bonding as expected. However, this process requires a relatively expensive commercial bonder and is very sensitive to presence of particulates on the surfaces of wafers to be bonded.

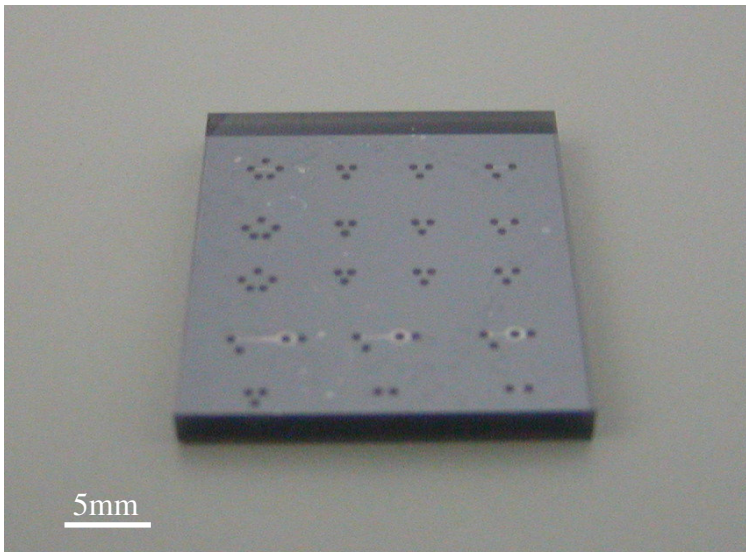

Figure 2.13: Photograph of a microfabricated chip using silicon-to-glass anodic bonding. The holes are the pressure measurement ports etched through in silicon using DRIE.

2.3 Fluidic Interconnection

Once a linear micronozzle was fabricated, it was packaged to interface with instruments for gas flow test. As shown in Figure 2.14, this is accomplished by using capillary needles (400 μm in outer diameter (OD) and 200 μm in inner diameter (ID))

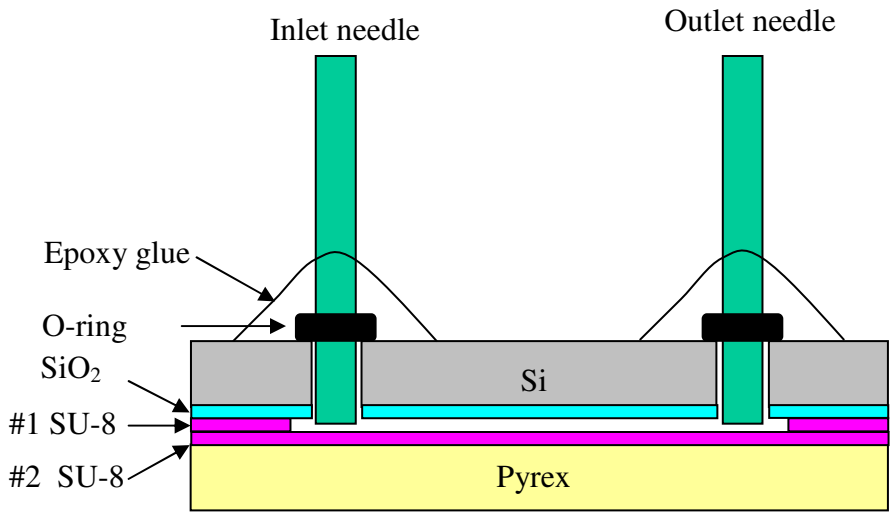

Figure 2.14: Schematic diagram of micro-to-macro interconnection.

and ethylene propylene O-rings (Apple Rubber). The ID of the O-ring is 250 μm, so a snug fit can be obtained after inserting the needle through the O-ring. The penetration depth of the assembly was adjusted, by manually controlling the position of the O-ring, such that the capillary needle did not touch the bottom of the micronozzle. The O-ring can also prevent leakage at the contact points. Since the length of the needle (13.45 mm) was much larger than the penetration depth (i.e., the thickness of the silicon wafer, 500 μm), a probe station was used to hold the needle and to keep it as upright as possible. Following these steps, a droplet of room temperature curing epoxy glue (Devcon) was applied around the interconnection holes to enhance the holding force. As shown in Figure 2.15, the packaged device was then connected with instruments (e.g., flow meters and manometers) through Tygon flexible tubing (2.31 mm in OD and 380 μm in ID, Cole-Parmer Instrument) to conduct gas flow tests. Epoxy glue was also applied in the connection areas between the needle and tubing to improve sealing [41].

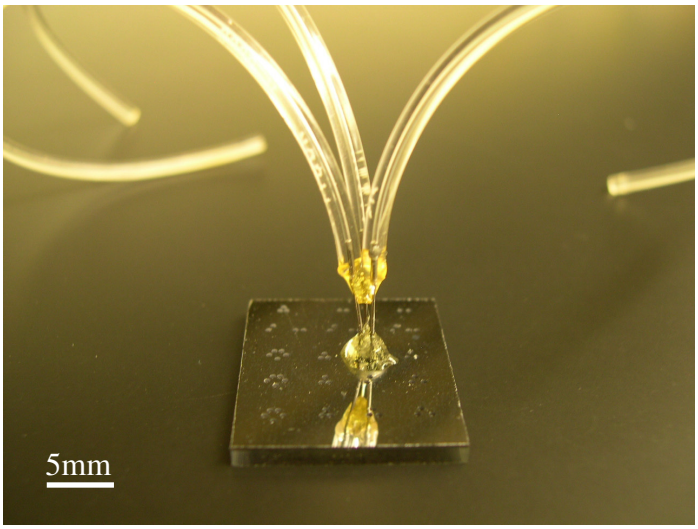

Figure 2.15: Photograph of a packaged nozzle connected with Tygon flexible tubing.

2.4 Gas Flow Test

A gas flow test setup, as shown schematically in Figure 2.16, was designed and implemented to study gas dynamics in micronozzles. In the experiments, working gas (N_2) flows from a regulated high-pressure cylinder (ranging from 13.8 kPa to 413.7 kPa), through a 0.5-μm filter, past a flow controller, into the nozzle and finally through a flow meter. The filter can prevent contamination from entering the nozzle. Upstream and downstream gas flow rates are read from the flow controller and flow meter (Hastings), respectively. Upstream, throat and downstream pressures are monitored using manometers (MKS Instruments). The manometer consists of a variable capacitance sensor and a signal conditioner producing a DC output signal in pressure units. The exit of the device is vented through the flow meter to a vacuum pump or atmosphere.

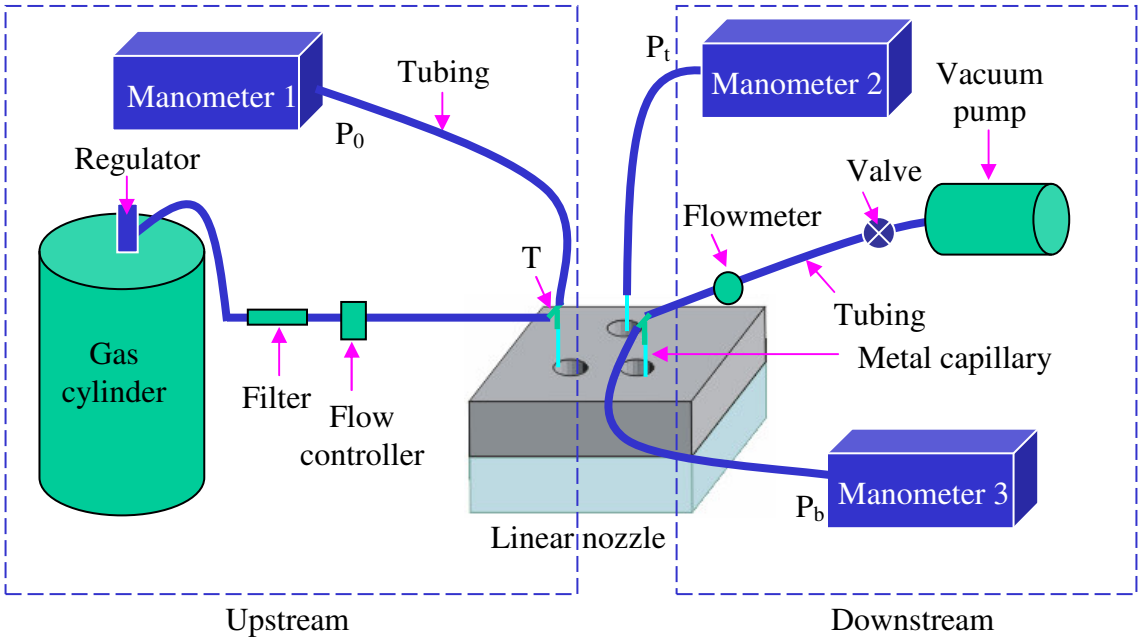

Figure 2.16: Gas flow test setup for testing linear micronozzles. It consists of manometers, a flow controller and flow meters connected with the MEMS device through flexible tubing and fittings.

2.5 Results and Discussion

Gas flow tests were performed to study the fluid dynamics of gas flows in linear contoured micronozzles. First, leakage tests were performed to characterize the bonded wafers with the two different techniques and the seal of device packaging with the micro-to-macro interconnection method. In the tests, the upstream and downstream flow rates of N_2 flowing through the linear nozzle were measured by changing the regulator pressure with a certain increment. As shown in Figure 2.17, the upstream gas flow rate is consistent with the downstream flow rate with increasing regulator pressures up to about 300 kPa for both SU-8 bonding device and anodic bonding device. As indicated by the same mass flow variations, both devices exhibit very similar viscous effects. When the regulator pressure increases further, leaking begins to occur in both devices, which is

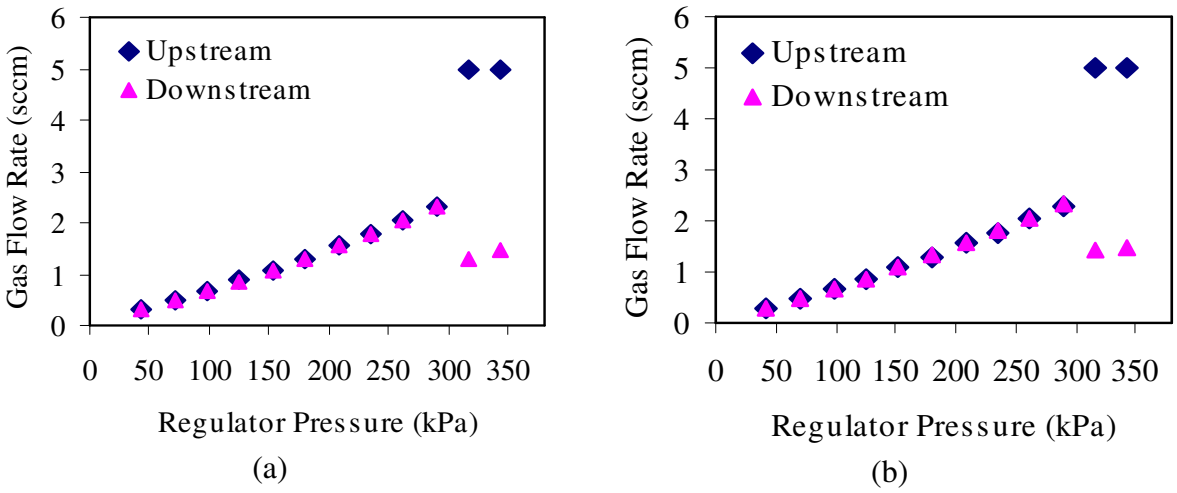

Figure 2.17: A comparison between SU-8 bonding and anodic bonding devices for gas flow rates with increasing regulator pressures: (a) SU-8 bonding nozzle; (b) anodic bonding nozzle.

indicated by the discrepancy between the upstream and downstream gas flow rates. The leak was observed in the contact area between the needle and Tygon tubing where air bubbles appear after soapy water was applied there. This was due to the deformation of the flexible tubing when the pressure inside the tubing was too high. The test results demonstrate that the interconnection method using flexible tubing and epoxy glue can only be used for pressure differentials less than about 300 kPa.

In the following test, the upstream pressure of the nozzle was increased from atmosphere to 300.0 kPa while the downstream pressure was held below 1.35 kPa. Figure 2.18 (a) compares the mass flow measurements with the predictions with the isentropic model and ANSYS numerical simulation for design 1. The discrepancy in the mass flow variation is due to the influence of the sidewall and endwall (i.e., top and bottom) boundary layers. The difference between the numerical calculations with no-slip boundary conditions and the measurements can be attributed to the endwall boundary

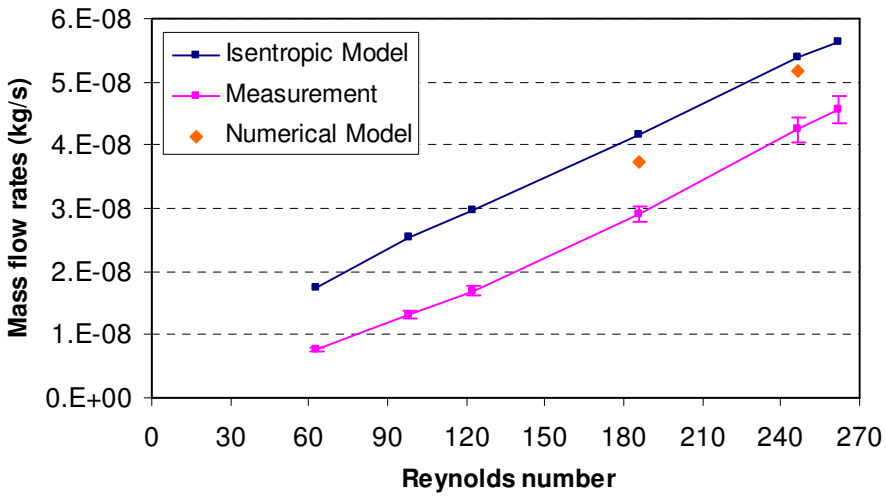

(a)

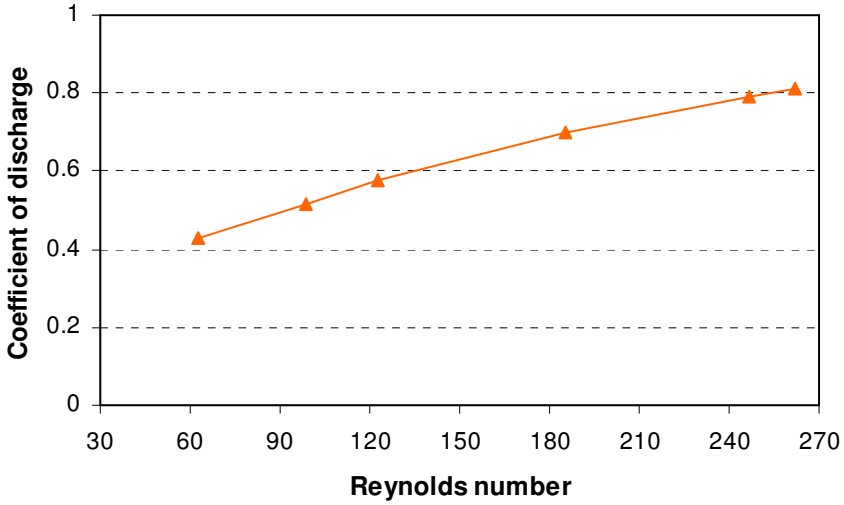

(b)

Figure 2.18: (a) Comparison of mass flow rate between the model predictions and measurements for design 1; (b) effects of the Reynolds number on the coefficient of discharge of the gas flow.

growth, which is not modeled in the 2-D simulation. Figure 2.18 (b) shows the variation of coefficient of discharge as a function of the Reynolds number of the gas flow. The coefficient of discharge, or mass flow efficiency, is the ratio of the actual mass flow to the theoretical mass flow. This quantifies the blockage associated with the boundary layers [37]. As the inlet pressure of the nozzle is reduced, and hence the Reynolds

number is reduced, the mass flow efficiency becomes lower due to the increase in viscous losses, which is caused by increased influence of the boundary layers developed on the internal surfaces of nozzle [45].

Figure 2.19 shows variations of coefficient of discharge versus inlet pressure for the two designs in Table 2.1. As shown from this figure, design 2 exhibits slightly stronger viscous effects than design 1. This is probably due to the slightly stronger influence of the endwalls of design 2, though design 2 has the very similar length-to-width ratio and depth as design 1, leading to identical theoretical flow resistances [50].

Figure 2.20 compares measured throat pressures with theoretical predictions using the isentropic model for design 1; both of them increase with rising inlet pressure. The disparity is due to the viscous effects in the nozzle: the gas velocity near the throat wall is

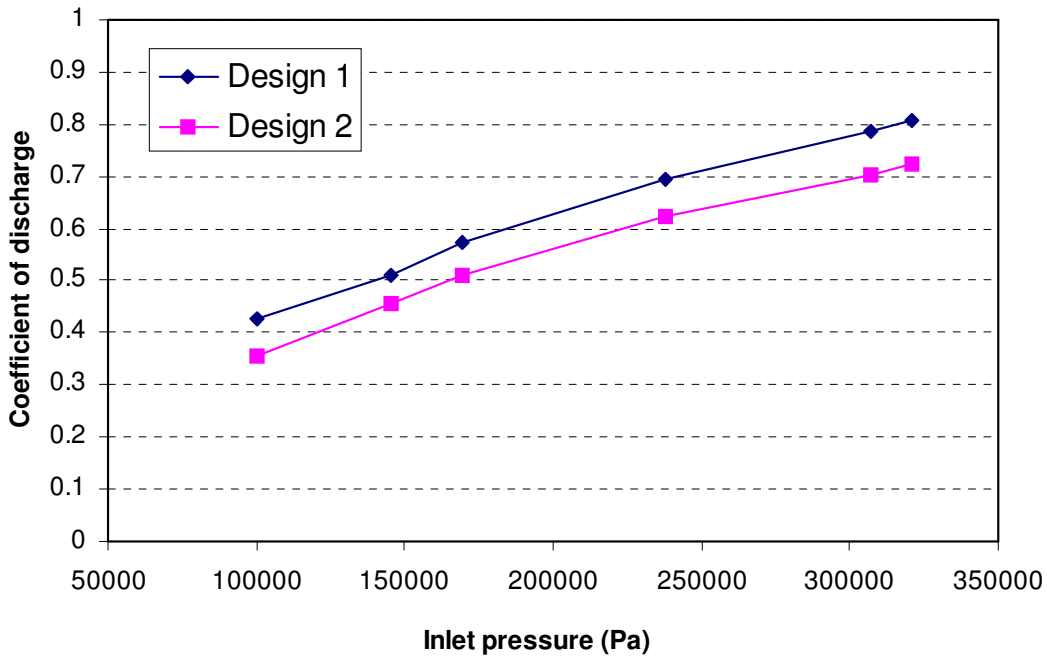

Figure 2.19: Effects of inlet pressure on the coefficient of discharge for the two designs.

very slow, leading to the increase in pressure. Figure 2.21 shows the effects of downstream pressure (P_d) on the mass flow rate for design 1. The upstream of the nozzle is kept at one atmosphere (P_0) and the downstream of the nozzle is connected to a

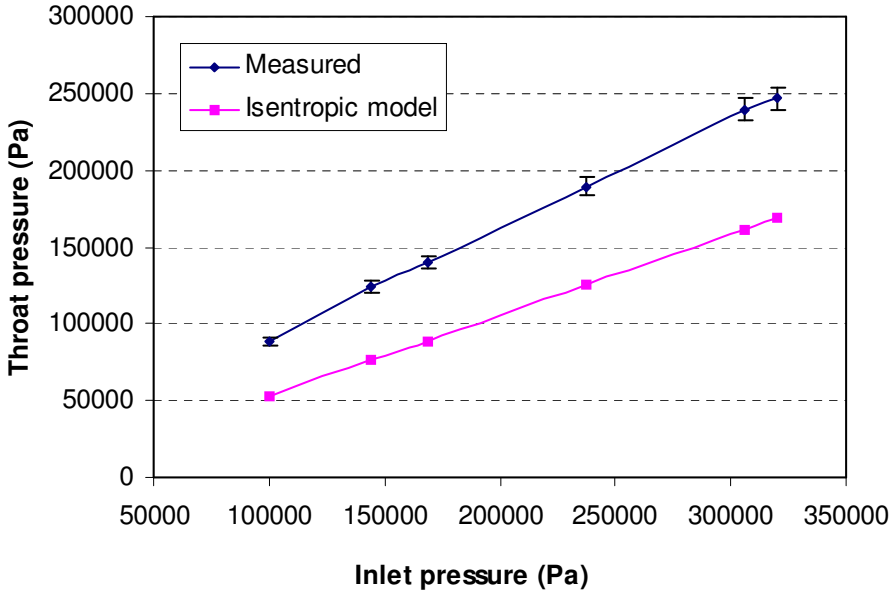

Figure 2.20: Comparison of measured and calculated throat pressure as a function of inlet pressure.

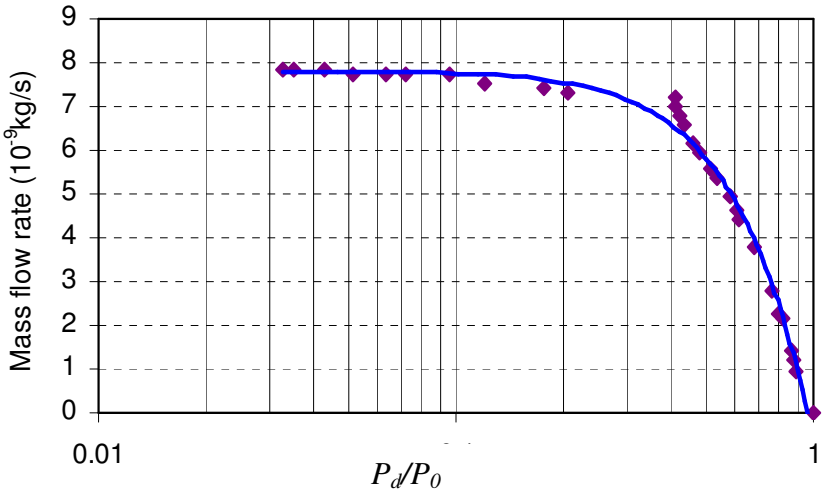

Figure 2.21: Effects of downstream pressure P_d on the mass flow rate. The inlet pressure P_0 is kept at one atmosphere while the downstream pressure P_d varied.

vacuum pump that can alter P_d via a valve. When P_d is nearly the same as P_0, the flow remains subsonic throughout and the mass flow rate increases with decreasing P_d/P_0. However, when the downstream pressure is decreased to a critical value, mass flow rate is unaffected by changes in P_d/P_0. Under these circumstances, when changes in the downstream pressure cannot effect conditions upstream of the throat, and therefore have no effect on the mass flow rate through the nozzle, the nozzle is said to be "choked." Therefore, a Mach number of 1 has been reached at the throat of nozzle [38].

2.6 Summary

The design, fabrication and testing of linear test structures were addressed in this chapter. A 1-D isentropic model was introduced to describe the behavior of gas flows in linear micronozzles. This analytical model can be used conveniently to calculate the Mach number and pressure distribution for given device geometric parameters with certain accuracy. ANSYS FEA was conducted to validate the analytical model, and a relatively good agreement was observed for the Mach number distribution in the nozzle. With respect to the pressure distribution, FEA results are within 18 % of the isentropic modeling results. The discrepancy is obviously due to the viscous effects of the device accounted in the FEA while the isentropic model is frictionless in nature.

Two processes were explored to fabricate the micronozzles, and their respective advantages and disadvantages have been identified. Following the device fabrication, details about the device packaging and testing were presented. The experimental results demonstrated that a sonic flow was reached at the throat area of the nozzle. It is also noted that the throat pressure measurements agree roughly with the model predictions.

The viscous effects in the micronozzles were characterized by comparing the measured mass flow rates to the theoretical predictions using the isentropic model. The nozzle mass flow efficiency was measured to be in the range of 0.36-0.81, increasing with rising Reynolds number as a result of the decreasing influence of boundary layer.

CHAPTER 3

DEVICE DESIGN AND MODELING

3.1 Introduction

The previous chapter on the linear test structures has laid the foundation for developing gas separation nozzles. In this chapter, the diffusion and flow processes in the separation nozzle are described, followed by the discussion of design considerations of a single-stage separation nozzle system. Finite element analysis is then conducted to predict the separation efficiency of the design device.

3.2 Theory: Separation Nozzle Method

The basic principles of separation nozzle were reviewed in Section 2.1. This section is devoted to the description of separation flow processes. In a physical analysis of the separation process of separation nozzle systems, certain parameters are used in analogy with those employed in other enrichment techniques. These parameters, in a general way, take into account the fact that the results obtained from analyzing the elementary separation process can be applied to a multi-stage system [23-26]. They describe the concentration change achieved in a single separation element and the splitting of mass streams. The shift in concentrations between the light and the heavy fractions is characterized by the separation factor *A*. For a simple binary gas mixture, *A* is defined as

$$A = \frac{\theta_l (1-\theta_h)}{\theta_h (1-\theta_l)} \tag{3.1}$$

where θ_l and θ_h are the light component and heavy component partial cuts, respectively. The partial cut θ_i of a component i is defined below in (3.2) as the percentage of its throughput in the separation element, which is withdrawn in the light fraction stream

$$\theta_i = \frac{\dot{m}_{i,light}}{\dot{m}_{i,light} + \dot{m}_{i,heavy}} \tag{3.2}$$

where $\dot{m}_{i,light}$ and $\dot{m}_{i,heavy}$ are the mass flow rates of component i in the light fraction and heavy fraction, respectively.

3.2.1 Equilibrium Separation

In the microscale separation nozzle, a gas mixture passes through a centrifugal field with a high speed. Because of the extremely short period of flow time of the mixture through the device, no equilibrium distribution of the components of the mixture can be established. As a consequence, the diffusion streams caused by pressure and concentration gradients cannot fully compensate each other at each point. Nevertheless, some fundamental aspects of the separation process can be described by the limit case of equilibrium separation such as the distribution of molecular species in a steady-state cylindrical flow.

For a simplified cylindrical flow with concentric stream lines which is split into two partial streams at a point r, θ_i can be calculated directly by radial integration over the flux profile [24]. At thermal equilibrium, θ_i is shown to be

$$\theta_i(r) = \frac{\exp[(r/r_0)^2 \frac{\gamma}{2} \frac{M_i}{\overline{M}} Ma_m] - 1}{\exp[\frac{\gamma}{2} \frac{M_i}{\overline{M}} Ma_m] - 1} \tag{3.3}$$

where r_0 is the radius of the deflection wall, γ is the ratio of specific heats of the mixture, M_i is the molecular mass of the component, $\overline{M}$ is the average molecular mass of the mixture, and Ma_m is the peripheral Mach number of the mixture (i.e., the ratio of the gas velocity to the speed of sound in the gas). The derivation of this equation is detailed in Appendix B. This simplified equilibrium model can be used to describe some fundamental aspects of the separation process. For example, the separation factor of the mixture A (as obtained from evaluating θ_i for both the light and heavy components) is predicted to increase with Ma_m as a result of the increasing separating pressure diffusion stream.

Because of the limited flow time of the mixture in the centrifugal field, and the spatial change of the centrifugal forces, the resultant non-equilibrium effects become so significant that the standard diffusion equations and the Navier-Stokes equations cannot accurately describe the diffusion and flow processes in the gas separation device. Monte-Carlo calculations have been used to derive some qualitative information about the different behavior of the components of a mixture [52, 53]. However, more research efforts are needed to study the non-equilibrium effects quantitatively by solving the Boltzmann equation for a strongly perturbed velocity distribution in a gas mixture flow [24]. In this work, the concentration effects of micro separation nozzles are examined with finite element analysis (FEA) and experimental means such as gas separation experiments and mass spectrometric gas analysis.

3.2.2 Diffusion Processes

The process of mixture component separation in the separation nozzle is determined by the diffusion of the components, which permeate the stream surfaces of the mixture, when the flow is deflected. As a result of the curvature of the stream surfaces, a component of the pressure gradient is developed which is normal to the direction of flow, and pressure diffusion causes the light component to be transported to the concave side and the heavy component to the convex side of a mixture stream surface. In the course of deflection, an increasing concentration gradient is also established at the stream surface, which increases the concentration diffusion streams directed opposite to the pressure diffusion streams. While the heavy component is concentrated increasingly at the periphery of the centrifugal field with the increasing angle of deflection, the molar fraction gradients of the heavy component can become so high in this region that the remixing concentration diffusion streams may exceed the separating pressure diffusion streams [24].

The differential equation for the spatial development of the partial cut θ_i is obtained by regarding the transport of the component i through an elementary area of a stream surface of the gas mixture. If it is assumed for simplification that the molar stream surfaces of the mixture correspond to concentric cylinders in the separation nozzle, it holds that where L_i is the throughput of the component i per unit length of the nozzle, j_i

$$\partial \theta_i = \frac{1}{L} j_i r \partial \phi \tag{3.4}$$

the radial component of the flux, and $r\partial\phi$ the elementary area. The flux j_i results from the motion of the heavy component relative to the stream surface of the mixture.

The calculation of j_i is based on the binary diffusion equation

$$j_i = -\nu D[\nabla N_i - (\Delta M / \overline{M})N_i(1 - N_i)(1/p)\nabla p] \tag{3.5}$$

where ν is the total number density, D the diffusion coefficient, ΔM the mass difference, N_i the molar fraction of the component, and p the static pressure. This equation contains only the term describing concentration and pressure diffusions. The influence of thermal diffusion can be neglected because of the low temperature gradients in the separation nozzle and because of the small thermal diffusion factor [24]. The diffusion processes can be described quantitatively by solving the diffusion equation numerically, which is the focus of Section 3.4.

3.3 Design of Separation Element

A single-stage separation nozzle system is designed on the basis of the results from the linear test structures presented in Chapter 2. Figure 3.1 shows the schematic of the designed separation system with inlet and outlet ports for gas sample injection and collection. As illustrated in the close-up view of the separation element, the flow is confined by a curved nozzle formed by the deflection wall and the inner wall, then deflected by the curved wall, and finally splits into two fractions by the skimmer. Also shown in Figure 3.1 are some critical design parameters such as the nozzle throat width a, exit width w, radius of curvature of the deflection wall r_0, and skimmer distance f (i.e., the width of the channel formed by the skimmer and the deflection wall).

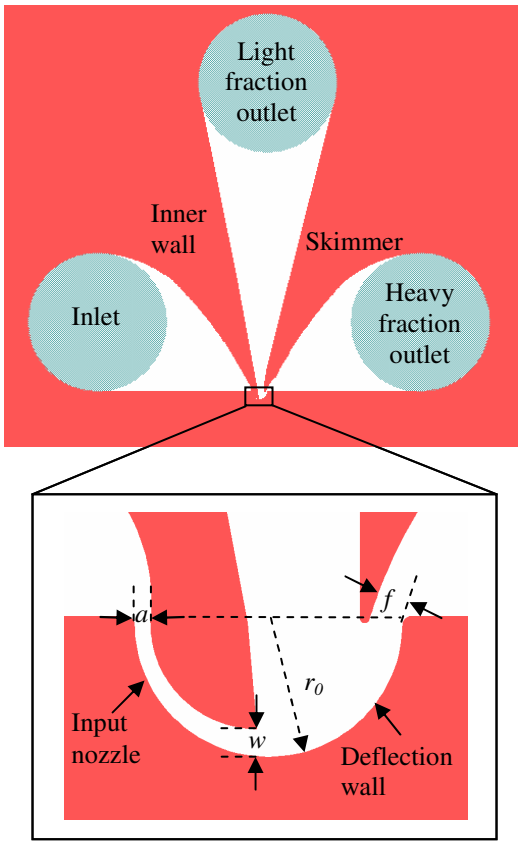

Figure 3.1: Schematic of the single-stage separation nozzle system and close-up of the separation element with the critical design parameters.

Previous studies [22, 23] on the uranium isotope separation proved that finite values for mixture separation were only found in the transition flow regime between the continuum flow and free molecular flow. Normally, the Knudsen number *Kn* is used to characterize the gas flow regime

$$Kn = \frac{\lambda}{d} \tag{3.6}$$

where λ is the mean free path of gas flow and the characteristic dimension used as a basis below is the nozzle depth *d*.

The mean free path λ can be estimated from the following equation [38]:

$$\lambda = \frac{1.26\mu\sqrt{RT}}{P_t} \tag{3.7}$$

where μ is the coefficient of viscosity of the gas mixture, R is the gas constant, T is the gas temperature, and P_t is the throat pressure that can be estimated from Figure 2.19 for inlet pressure ranging from 1 to 3 atm. Consequently, the nozzle depth d is designed to be 5 μm, so Kn can be controlled between 0.005 and 0.05, which is located in the slip flow regime [54].

There is a relationship between the nozzle throat width a and theoretical mass flow rate $\dot{m}$ using an isentropic flow model (i.e., a frictionless adiabatic model) [38]:

$$a = \frac{\dot{m}}{d\sqrt{\gamma P_0 \rho}}\left(\frac{2}{\gamma+1}\right)^{-\frac{\gamma+1}{2(\gamma-1)}} \tag{3.8}$$

where ρ is the gas density. By changing the inlet pressure P_0 from 1 to 3 atmospheres, while keeping the outlet pressure at one atmosphere, the mass flow rate is controlled in the range from 0 to 2 standard cubic centimeters per minute (sccm), which is comparable to that of some existing miniature chemical sensors [9, 10]. Also, the viscous effects in the microscale device need to be taken into account. Based on the measurements of the mass flow efficiency of the linear structures, which ranges from 0.36 to 0.81 for different dimensions (Figure 2.18), two different nozzle widths, 3.6 μm and 18.0 μm, are designed. The expansion ratio (i.e., the ratio of exit width w to throat width a) of the input nozzle is still designed to be 1.69 as linear nozzles, so an ideal exit Mach number as high as 2 can be obtained for the gas flow in the nozzle.

In general, the skimmer distance *f* is influenced by the operating conditions such as the inlet pressure and the pressure expansion ratio (i.e., inlet-to-outlet pressure ratio) if a certain percentage of throughput of heavy gas molecules is withdrawn in the heavy fraction after the separation process. Two skimmer distances, 1/3 r_0 and 1/6 r_0, are designed to examine their effect on the separation efficiency and distribution of gas flow between the light fraction and heavy fraction. Table 3.1 lists the characteristic parameters of the three designed devices.

Table 3.1: Geometric parameters of the three designed separation nozzles.

Device	Radius of deflection wall (μm)	Nozzle throat width (μm)	Skimmer distance (μm)
1	120	18.0	20.0
2	120	18.0	40.0
3	120	3.6	20.0

3.4 Computational Fluid Dynamics Modeling

A computational fluid dynamics (CFD) model was developed to assess the performance of the designed device and verify the experimental results presented in Chapter 5. The CFD model was based on solving the Euler equations and Maxwell-Stefan diffusion equation numerically. The bulk of this work was carried out by Mr. Jonathan Day for his M.S. thesis research under the guidance of Prof. Christopher Cadou and in direct collaboration with Prof. Reza Ghodssi and myself. Because of the importance of this numerical simulation for better understanding the underlying physics

of the device operation, this section reviews its key aspects such as the governing equations, boundary conditions, solution method, and key modeling results. The reader can refer to [55] for a more comprehensive and in-depth description of this numerical study.

3.4.1 Governing Equations

The flow field in the device is determined by the device geometry and boundary conditions. As discussed in Section 3.3, the gas flow in the device should be controlled in the slip flow regime, thus effects of the small dimensions (i.e., velocity slip at the walls) on the development of the boundary layer are of particular interest. As discussed in Section 3.2.2, it is the radial pressure gradient that drives the pressure diffusion process responsible for stratifying the mixture flow. And it is known that the radial pressure gradient is proportional to the square of the gas velocity [24]. Therefore, examining the effects of the device dimensions on the boundary layer growth is very important [55].

The flow processes in the device are described by the 2-D time-invariant, compressible Euler equations [52] plus the equation of state for an ideal gas [57].

$$\left(\vec{u}\cdot\vec{\nabla}\right)\rho+\rho\vec{\nabla}\cdot\vec{u}=0 \tag{3.9}$$

$$\left(\vec{u}\cdot\vec{\nabla}\right)\vec{u}+1/\rho\vec{\nabla}\rho=1/\rho\,\vec{F} \tag{3.10}$$

$$\left(\vec{u}\cdot\vec{\nabla}\right)p+\gamma p\vec{\nabla}\cdot\vec{u}=\left(\gamma-1\right)\left(Q-\vec{u}\cdot\vec{F}\right) \tag{3.11}$$

$$p=\rho RT \tag{3.12}$$

where $\vec{u}$ is the velocity vector, γ is the ratio of specific heats (C_p/C_v) for the gas mixture, Q is a net heat generation per unit volume (equal to zero here) and $\vec{F}$ is a body force

vector (also equal to zero here). Equation (3.9) corresponds to conservation of mass, (3.10) represents conservation of momentum, (3.11) stands for conservation of energy, and (3.12) represents the ideal gas law.

As discussed before, the diffusion of heavier particles to the outer wall and lighter particles to the inner wall of the device is driven by the radial pressure gradient associated with the turning of the gas flow. However, there is also a reverse diffusion process opposing separation which is driven by the concentration gradient. The balance between pressure, concentration, and thermal diffusion is given by the generalized Maxwell-Stefan diffusion equation [57] for a two-component mixture

$$J_A^* = -cD_{AB}\left[x_A \nabla \ln a_A + \frac{1}{cRT}\left[(\phi_A - \omega_A)\nabla p - \rho\omega_A\omega_B\left(g_A - g_B\right)\right] + k_T \nabla \ln T \right] \tag{3.13}$$

where J_A^* is the diffusive flux, c is the concentration, D_{AB} is the diffusion coefficient, x is the mole fraction, a_A is the activity of component A, T is the temperature, ϕ_A is the volume fraction of A, ω_A is the mass fraction of A, g is the body force per unit mass, and k_T is the conductive heat transfer. The activity of the species is defined by the following equation [58]:

$$d\overline{G}_\alpha = RTd \ln a_\alpha \tag{3.14}$$

where $\overline{G}_\alpha$ is the partial molar Gibbs free energy, and d is the differential operator.

By converting the flux into a time derivative and making the assumptions that it is a binary mixture of N_2 and SF_6 and that the external force and temperature diffusion terms are negligibly small relative to the pressure and concentration diffusion terms, the diffusion equation (3.13) can be simplified as:

$$\rho\frac{\partial w_1}{\partial t}+\nabla\cdot\left(-\rho w_1 D_{12}\left(\nabla x_2+\left(x_2-w_2\right)\frac{\nabla p}{p}\right)\right)=-\rho\bar{u}\cdot\nabla w_1 \qquad (3.15)$$

Finally, the requirement that all of the gas samples within the device be either SF_6 or N_2 yields

$$w_2=1-w_1 \qquad (3.16)$$

The above equations (3.9-3.12, 3.15, 3.16) completely define the flow field within the computational domain set by the separation nozzle geometry.

3.4.2 Boundary Conditions

Figure 3.2 demonstrates schematically the computational domain used for the numerical model. The localities of the boundary conditions are the inlet, the light and heavy fraction outlets, and all of the other walls including the deflection wall and the skimmer.

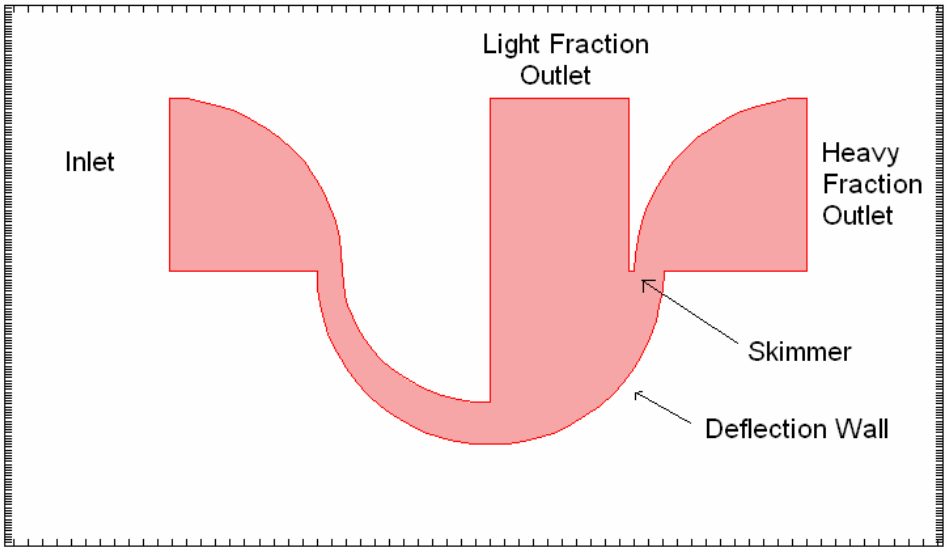

Figure 3.2: Computational domain used for the numerical model.

The boundary conditions for the device were set as no material flux through the wall (3.17) and velocity at the wall (3.18). Perfect slip is assumed (i.e., there is no shear stress at the wall).

$$\vec{n} \cdot \vec{N} = 0; \vec{N} = -\rho w_1 \sum_{k=1}^{2} D_{1k} \left(\nabla x_k + \left(x_k - w_k \right) \nabla p / p \right) + D^T \nabla T / T + \rho w_1 \vec{u} \tag{3.17}$$

$$\vec{n} \cdot \vec{u} = 0, \quad \vec{t} \cdot \left(-p\vec{I} + \eta \left(\vec{\nabla} \vec{u} + \left(\vec{\nabla} \vec{u} \right)^T \right) \right) \vec{n} = 0 \tag{3.18}$$

where $\vec{n}$ is a unit vector normal to the surface and pointing into the enclosed volume, $\vec{t}$ is a unit vector that is tangent to the surface, and $\vec{I}$ is the identity vector.

Conditions at the inlet were set as follows: the mass fractions of SF_6 and N_2 were 5% and 95% (corresponding to 1 mole% SF_6 of and 99 mole% N_2), respectively. The Mach number at the inlet was 0.2 in the x-direction and 0 in the y-direction. The non-dimensional fluid density was 1 and the non-dimensional inlet pressure varied from 1 to 3 atm. The outlet boundary conditions were set as follows: the convective mass flux is normal to the exit area (3.19), and the non-dimensional pressure is equal to 1 atm along the exit plane.

$$\vec{n} \cdot \vec{N} = 0; \quad N = -\rho w_1 \sum_{k=1}^{2} D_{1k} \left(\nabla x_k + \left(x_k - w_k \right) \nabla p / p \right) + D^T \nabla T / T \tag{3.19}$$

3.4.3 Solution Method

A commercially available software FEMLAB was utilized to solve the governing equations using a finite element method. The software is especially suitable for this application because it allows the user to input any governing equations in symbolic form

and therefore control exactly which parts of the governing physics are included and excluded.

Like some other CFD simulation tools, FEMLAB allows the user to describe the computational domain, generate the finite element mesh, and apply boundary conditions. Figure 3.3 shows the finite element mesh for the model with an unstructured grid of triangular elements. FEMLAB uses adaptive gridding so the meshes for each set of flow conditions are different. One major benefit of the adaptive meshing method is the increased ability to converge to a solution as the initial conditions at each mesh update are more accurate. Also fewer grid points are required as they are judiciously located, which reduces the memory requirements for the model. Furthermore, the adaptive meshing algorithm [59] regenerates the mesh by increasing the number of grid points at the locations of the highest error values.

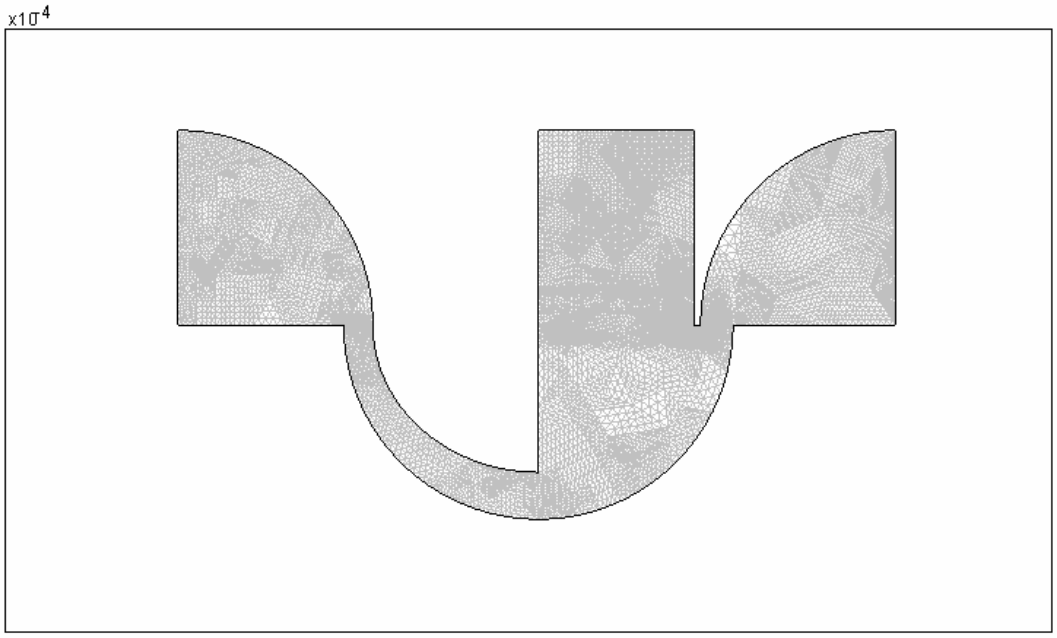

Figure 3.3: Finite element mesh for the model geometry.

The software also allows the user to specify different types of boundary conditions at each location which is either external or internal to the model geometry. The available boundary conditions are dependent upon the equations being solved. For the Euler equations, the boundary conditions can be inflow/outflow, slip/symmetry, and no conditions. For the Maxwell-Stefan diffusion equation, the available boundary conditions are no flux, convective flux, and fixed mass fraction. In this study, only the external boundary conditions are imposed. The specific boundary conditions utilized were previously discussed in Section 3.4.2.

The software provides a variety of solvers such as linear and non-linear, direct and iterative, steady-state and time-dependent, and parametric solvers. FEMLAB also offers the capability to solve for the weak, general, or coefficient solution form [60]. Since the problem under consideration is a highly non-linear steady-state problem, an iterative, steady state non-linear solver is used. This solver uses an affine invariant form of the damped Newton method to solve a linearized form of the governing equations.

3.4.4 Results

The device geometry has an impact on the specific flow field generated by creating several key features within the flow field regardless of the applied boundary conditions. As shown in Figure 3. 4, the device geometry can be broken into three main sections: the converging/diverging section, the expansion/deflection wall section, and the skimmer section.

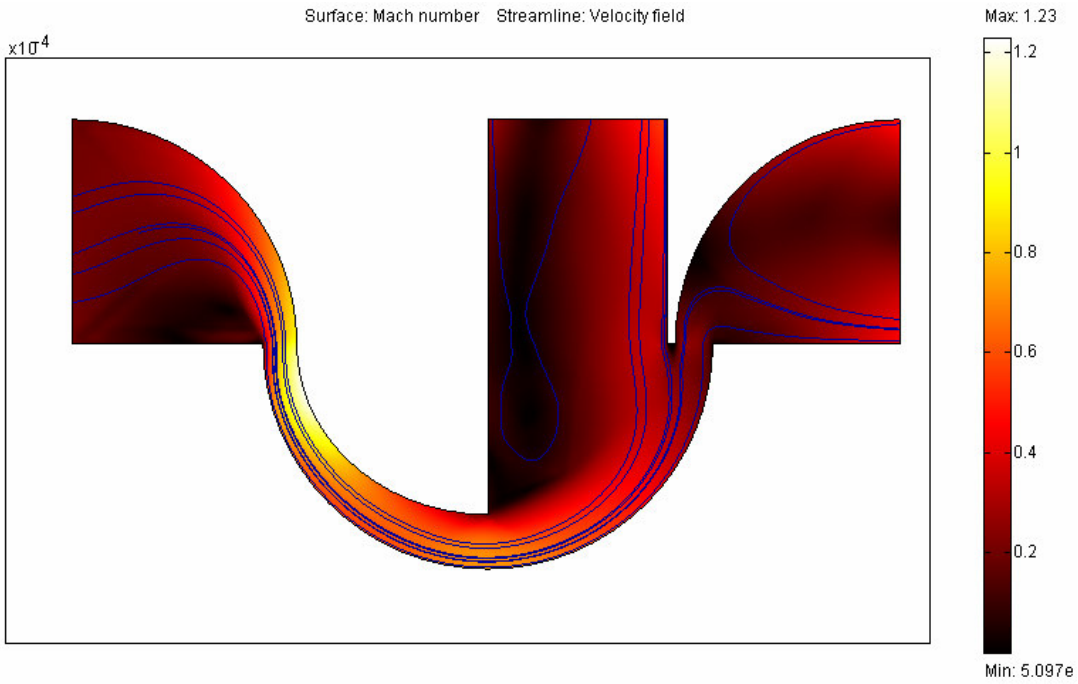

Figure 3.4: Simulated flow field in the device at a pressure ratio of 1.75.

The converging segment on the left is where the gas sample enters the device and is compressed into the diverging portion. A key feature of the flow is the recirculation region along the straight wall; it is generated as the straight wall can be considered as a forward step in the flow field. The second flow feature within the converging/diverging section is the shock wave generated at the nozzle throat; the location of the shock wave is correctly determined by the computational model.

The expansion/deflection wall section is regarded as a backward step in the flow field. The nature of a backward step generates a recirculation region along the curved wall behind the step. This recirculation region can be demonstrated by the streamlines in Figure 3.4.

The skimmer section is conceptually comprised of two flow features: a wedge-shaped tip (i.e., the skimmer itself) and a backward step (the heavy fraction outlet). The

interaction of these two features generates a unique situation in which there are two possible flow modes. The first mode has the flow hitting the skimmer straight on as shown in Figure 3.4. In this mode, there is little interaction between the two flow features and therefore they can be treated as two separate entities.

In the second flow mode, there is a significant interaction between the two flow features as shown in Figure 3.5. The flow in this case is dominated by the redirection of the flow prior to hitting the skimmer and therefore the angle of attack is no longer zero. The change in the angle of attack between the flow direction and the skimmer creates two significant changes in the flow pattern. The first feature is the splitting of the recirculation zone created within the expansion region into two separate counterflowing vortices. The second feature is the lack of the redirection of the flow within the heavy fraction. Instead, the flow continues along the curved wall to the exit. This relocates the

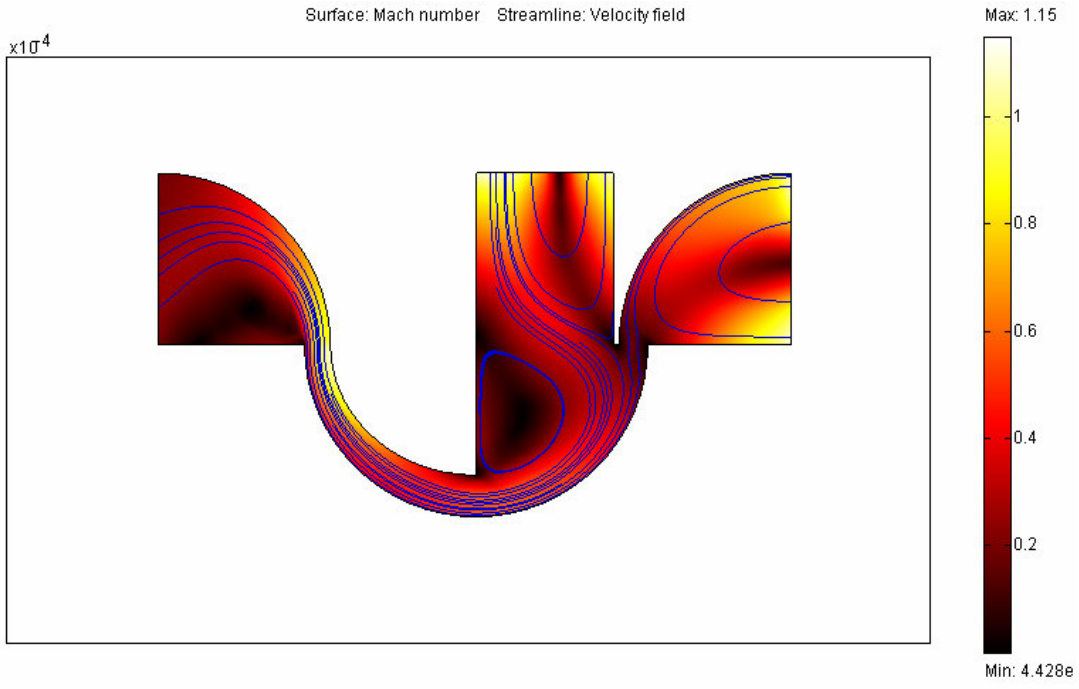

Figure 3.5: Second flow mode in the device at a pressure ratio of 2.

recirculation region within this area to the flat wall. The effects of these changes in the flow structure are higher flow velocities within both exit regions and an increase in the separation efficiency.

The two flow modes were achieved within the computational model through the use of two solution methods. The first mode is achieved through the use of the weak solution mode for the governing partial differential equations (PDEs). The second mode is obtained through the use of the general solution mode for the governing PDEs. The difference between the two modes is the weak solution guarantees the use of an exact Jacobian [55].

A. Pressure Distribution

The pressure distributions in the flow field are shown in Figure 3.6 (a)-(c) for three different pressure ratios. For relatively low pressure ratios (less than 1.75), the pressure wave remains intact throughout the expansion region. However, the pressure gradients are low and therefore do not generate as high of a diffusive flux, as illustrated in Figure 3. 6 (a). At high pressure ratios (larger than 2.5), the pressure wave becomes wider than the skimmer distance and therefore the separation effects are not fully realized due to the spreading out of the high pressure region as depicted in Figure 3.6 (c). At a pressure ratio of approximately 2, an optimum combination of high pressure gradient and a contained pressure wave matching the skimmer width is achieved, as shown in Figure 3.6 (b).

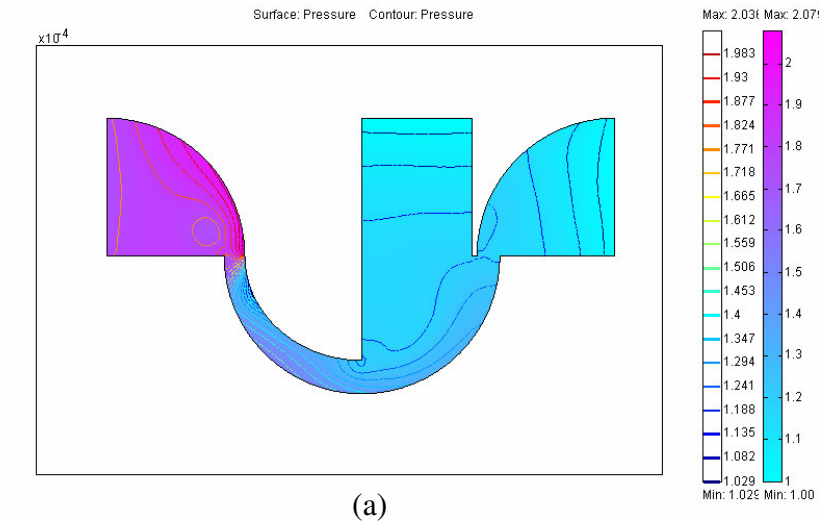

(a)

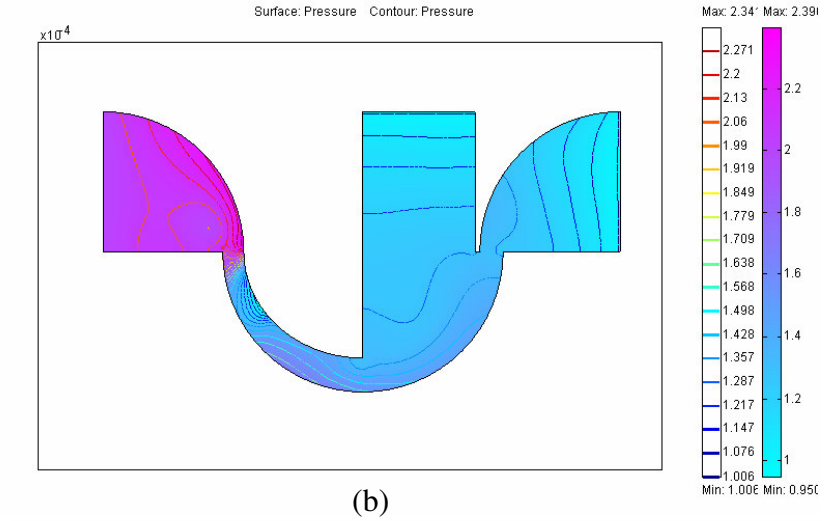

(b)

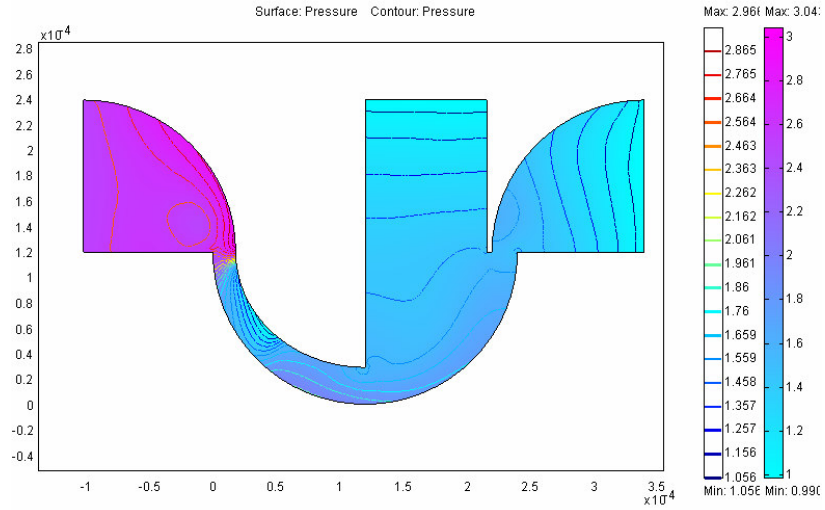

(c)

Figure 3.6: Pressure distributions in the flow field for three different pressure ratios: (a) 1.75, (b) 2.0, and (c) 2.5.

B. Mass Flux Distribution

The SF_6 and N_2 mass flux distributions, shown in Figure 3.7 (a)-(b), demonstrate the key features in providing a separated flow. As shown in all three curved sections, SF_6

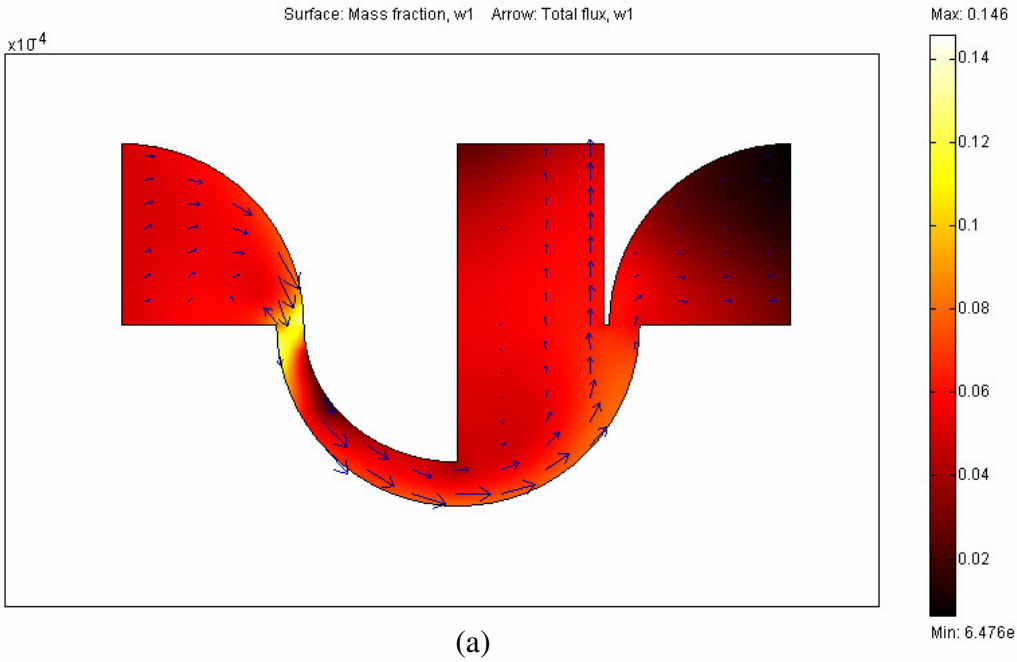

(a)

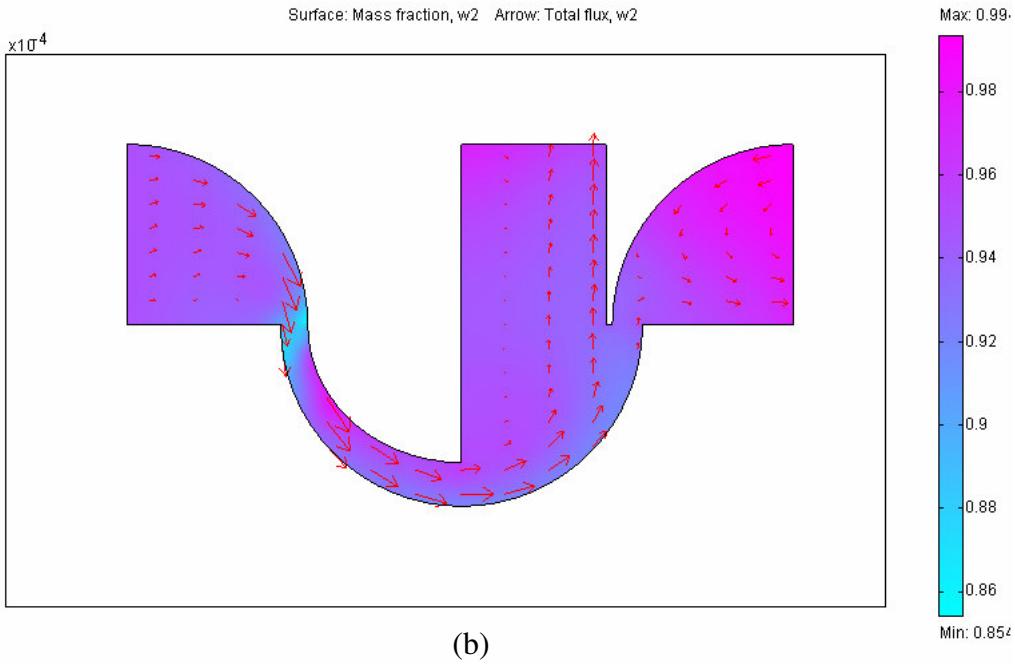

(b)

Figure 3.7: Mass flux distribution of SF_6 (a) and N_2 (b) for the pressure ratio of 2.0.

flux moves steadily to the outer wall while N_2 is pushed into the center of the flows field. High SF_6 diffusive flux also occurs at the nozzle throat, as shown in Figure 3.7 (a). The switching of radial directions at the nozzle throat requires SF_6 to jump across the nozzle throat. The deformation of the shock is due to this high flux region which could be manipulated to increase the overall separation efficiency of the device.

C. Separation Factor

The separation factor *A* is the key parameter in characterizing the performance of the device. *A* was defined previously in Equation (3.1). In this numerical study, *A* is computed from the computational results by taking a cut along the flow path at the heavy and light fraction exits, respectively, and recording the mass fraction fluxes of N_2 and SF_6 along this cut at 2000 equally spaced locations. This data was then used to calculate the total mass flow rates of SF_6 and N_2 through the light and heavy fraction streams by integrating the flow data with a MATLAB script.

Figure 3.8 shows the computational analysis of separation factor for device 1 (Table 3.1). The two model curves shown are the separation factor that is calculated depending upon the flow mode achieved. As shown in Figure 3.8, the second flow mode creates significantly higher separation factors. It is believed that this flow mode is only achieved under specific inlet conditions. Combining the two flow modes shows the potential maximum separation factor if a jump in flow modes is achieved around a pressure ratio of 2.0. The pressure profiles shown in Figure 3.6 (a)-(c) reveal that the cause of the peak in the separation factor is the movement of the competing effects of the dispersion of the pressure wave towards the inner wall and the increasing pressure

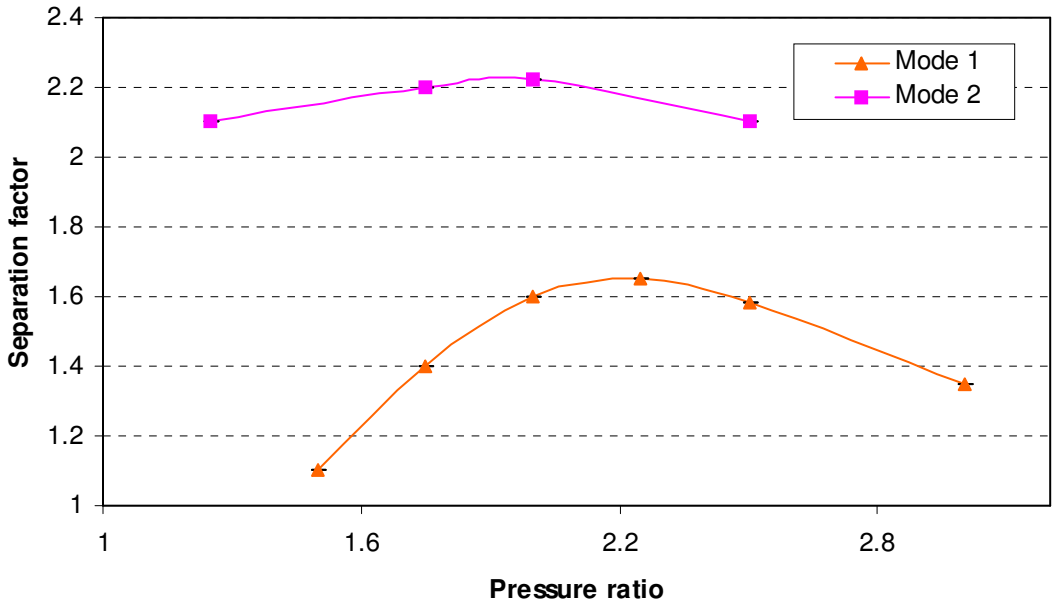

Figure 3.8: Variation of separation factor with pressure ratio for the two flow modes.

gradient causing higher diffusion rates. At the pressure ratio of approximately 2, an optimum combination of high pressure gradient and a contained pressure wave matching the skimmer width provide the peak in the separation factor.

D. Residence Time

As aforementioned, the most notable advantage of the separation nozzle method is its fast response when compare to other commonly used concentration approaches. The time required for transit of a gas sample through the separation nozzle is governed by the residence time. As shown in Figure 3.9, the calculated residence time decreases as a result of the increase in the mean flow velocity through the device when the pressure ratio is increased. The desirable device response time should be less than 1 ms which is easily met by even the maximum simulated residence time of about 12 μs.

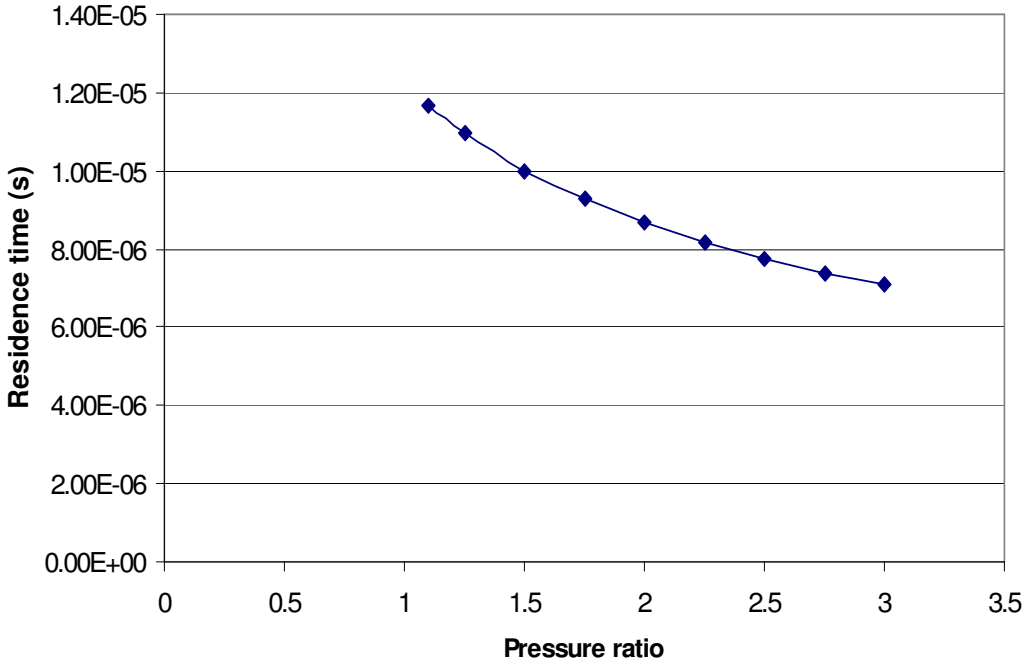

Figure 3.9: Residence time of gas flow in the device as a function of pressure ratio.

3.5 Summary

In this chapter, the basic theory of separation nozzle method has been reviewed, and separation and diffusion processes in the device were discussed. Design considerations of the single-stage separation nozzle systems based on the results from the linear test structures have been addressed, and three different designs with varying throat widths of input nozzle and skimmer distances were presented. A numerical model based on the compressible Euler equations and Maxwell-Stefan diffusion equations has been introduced to study the separation nozzle flows. The CFD analysis reveals the dependence of the separation factor on the inlet-to-outlet pressure ratio, and predicts the response time of the designed device. These simulation results can be used to verify the experimental data from device testing (presented in Chapter 5) and provide insight into the understanding of the diffusion and flow processes in the gas separation device.

CHAPTER 4

DEVICE FABRICATION

4.1 Introduction

Fabrication of MEMS devices is based on the technology originated from the microelectronics industry and enhanced with specialized techniques generally called micromachining [46]. Commonly used MEMS fabrication techniques include bulk micromachining, surface micromachining, wafer-level bonding, LIGA, and micro-electro-discharge machining (EDM). A typical MEMS device can be realized by using any of these processes or some combined processes. In this research work, bulk micromachining and wafer-level bonding are utilized to fabricate the gas separation devices, and therefore are discussed in detail below.

Bulk micromachining has been broadly applied in the fabrication of MEMS sensors, actuators, and structures. Bulk micromachining is used to selectively remove silicon or other materials from substrates to form membranes on one side of a wafer; or to make a variety of trenches, holes, or other structures [61]. The etching approaches used in bulk micromachining can be categorized as wet etching and dry etching.

In wet bulk micromachining, features are sculpted in the bulk of materials by isotropic or anisotropic wet etchants [62]. Commonly used wet etchants are potassium hydroxide (KOH), ethylenediaminepyrochatechol (EDP), tetramethylammonium-hydroxide (TMAH) for silicon etch, buffered HF for silicon dioxide etch, phosphoric acid for silicon nitride etch, etc. Wet etching offers advantages of low cost, high selectivity, fast etch rate, and smooth etched surface. However, it is relatively hard to control etch

rate and achieve submicron features using wet etching. The need for better critical dimension (CD) control and environmental issues drive a switch from wet to dry etching.

Dry etching covers a family of methods by which a substrate is etched in the plasma or vapor phase, physically by ion bombardment, chemically by chemical reactions through reactive species at the surface, or by combined physical and chemical mechanisms [62]. Besides the better CD control, dry etching can be highly directional and realize good production-line automation. Most common dry etching methods include reactive ion etching (RIE), plasma etching (PE), ion beam etching (IBE), etc. Frequently used etch gases are xenon difluoride (XeF_2) for isotropic silicon etch, carbon tetrafluoride (CF_4) for silicon dioxide etch, and sulfur hexafluoride (SF_6) plus oxygen (O_2) for silicon and silicon nitride etch. Recently developed DRIE technique presents an attractive solution to the fabrication of high-aspect-ratio microstructures [63], realization of through-wafer interconnections [34], and post-CMOS processes [64]. In this work, RIE is used to etch separation nozzle structures in silicon, and DRIE is employed to realize through wafer fluidic interconnections.

Another important MEMS fabrication technique is wafer-to-wafer bonding, which has been extensively used to fabricated microstructures such as microchannels [65] and to package MEMS devices such as pressure sensors [66]. Wafer-to-wafer bonding is an additive approach, complimentary to bulk and surface micromachining techniques. The bonding processes often involve alignment of the substrates.

Three types of wafer bonding are commonly used in MEMS device fabrication: direct bonding, intermediate-layer bonding and anodic bonding. The direct bonding method relies on forces that naturally attract surfaces together when they are very smooth

and flat. Direct bonding offers advantages of ease of operation and less thermal expansion mismatch problems using the same or similar substrate materials. However, in direct bonding, voids are easy to form at the bond interface due to particles, protrusions on the wafer surface, or trapped air. In addition, high-temperature anneal (i.e., 800-1200°C) employed in direct bonding precludes its use with wafers having sensitive structures such as integrated circuits.

Intermediate-layer bonding involves the application of bonding materials between the two substrates to be bonded. A wide range of intermediate layers have been used for wafer-lever bonding in microstructure fabrication. These approaches include: eutectic, solder, low melting temperature glasses (including glass frits), and thermal compression (using soft metal thin films or polymers) [66]. The SU-8 bonding process described in Section 2.3.1 falls into this category. Advantages of this type of bonding include low temperature, flexible choice of substrates, tolerance to contaminants, low cost, etc. However, intermediate-layer bonding has potential disadvantages of limited temperature stability and long-term stability as well as relatively low bond strength and yield [67].

Anodic bonding, as introduced in Section 2.3.2, is a field-assisted method, eliminating the high-temperature steps employed in direct bonding. This approach is less susceptible to the presence of particles and structures on the wafers than direct bonding. On the other hand, it has a higher bond strength and yield than intermediate-layer bonding since chemical bonding is presumed to occur at the interface that fuses the wafers together [66]. Therefore anodic bonding is adopted in this work to fabricate sealed gas separation devices.

4.2 Processing

Fabrication of gas separation devices is relatively straightforward, including two lithographic steps and two dry etches. As shown schematically in Figure 4.1, the process begins with a silicon wafer having a 2-µm layer of oxide on the backside. The first step involves spinning and patterning a 1.5-µm layer of photoresist on the front side of the wafer, followed by etching 5 µm deep separation nozzle patterns in silicon with RIE. A 6-µm masking layer of photoresist is then spun and patterned to define the inlet and outlet ports, after which the exposed backside oxide is etched with buffered HF. The combination of the patterned photoresist and oxide serves as the etch mask for generating through holes in the silicon substrate with DRIE. Following this step, the resist and oxide are stripped, and the silicon wafer is anodically bonded to a pyrex wafer to seal the microfluidic channels. Finally, metal capillaries are inserted into the inlet/outlet ports to realize fluidic interconnection. Details of each process step are described in subsequent sections below.

4.2.1 Wafer Cleaning

A standard clean consists of rinsing the wafer with acetone, methanol, isopropanol alcohol (IPA) successively. This sequential rinse is repeated two or three times followed by drying with compressed nitrogen. Moisture adsorbed on the wafer surface is removed by baking the wafer on a hotplate at 120°C for 10 minutes. The standard clean process is performed before every lithographic step.

If a wafer is to be subjected to a high temperature process such as chemical vapor deposition (CVD) and anodic bonding, it must be cleaned with RCA cleaning procedures.

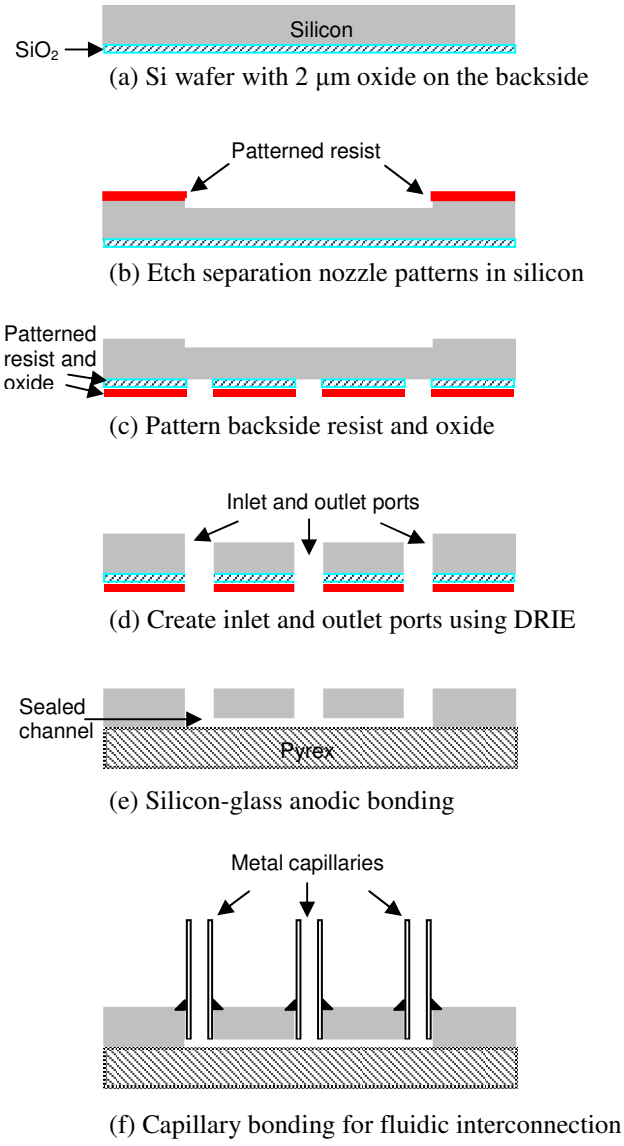

Figure 4.1: Fabrication process for single-stage separation nozzle including microfluidic interfacing.

The first step is to remove all organic coatings in a strong oxidant, like a 7:3 mixture of concentrated sulfuric acid and hydrogen peroxide (generally called “piranha”). Then a 5:1:1 mixture of water, hydrogen peroxide, and ammonium hydroxide is used to remove organic residues. Because this step can grow a thin oxide on silicon, it is necessary to insert the wafer to dilute hydrofluoric acid to remove this oxide. The HF dip is omitted

when cleaning wafers with intentional oxide on them. Finally, ionic contaminants are removed with a 6:1:1 mixture of water, hydrochloric acid, and hydrogen peroxide.

4.2.2 Photolithography

Photolithography is used to transfer patterns from masks to photoresist layers. As shown in Figure 4.1, the whole fabrication process requires two photoresist patterning steps: 1) definition of the separation nozzle structures on the front side of the wafer, and 2) definition of inlet and outlet ports on the backside of the wafer.

The photoresist patterning is performed on a contact aligner (model: EV620 by Electronic Visions Co.). The front side photolithography is as follows. The wafer is cleaned using the standard clean process. Next, the wafer is baked on a hotplate at 120°C for 10 minutes. Then hexamethyldisilazane (HMDS) (MicroSi, Inc.), an adhesion promoter, is dispensed onto the wafer. After wetting the wafer surface for 60 seconds, HMDS is spun at 3000 rpm for 60 seconds followed by spin-coating Shipley 1813 (Shipley Co., Marlborough, MA) at 3000 rpm for 60 seconds. A 60 second softbake at 100°C on a hotplate is performed to remove solvents in the resist and promote adhesion of the resist layer to the wafer. After softbake, the resist is exposed using an exposure dose 187 mJ/cm^2. The exposure is followed by development in Shipley 352 developer (Shipley Co., Marlborough, MA) for 30 seconds. After checking the resolved patterns under a microscope, the wafer is hard baked on a hotplate at 120°C for 10 minutes to remove residual solvents and anneal the resist film for improving the hardness of the film. Finally the thickness of the resist was measured to be 1.62 ± 0.02 μm with a stylus profilometer (model: Tencor P1 by KLA-Tencor Co.).

The backside photolithography is very similar to the front side one except that a thicker photoresist layer is used to serve as an etch mask for DRIE in the following step. The backside lithography is as follows. After wafer clean and application of HMDS, AZ 9245 (Clariant Co., Somerville, NJ) is spun on the wafer at 2500 rpm for 60 seconds. After a 120 second softbake at 110°C on a hotplate, the resist is exposed using an exposure dose 250 mJ/cm^2. In this step, a double-sided alignment scheme is used to align the inlet and outlet ports to the reservoirs of the separation devices patterned on the front side [62]. Figure 4.2 illustrates the double-sided alignment scheme including the following key steps:

1) The image of alignment marks of the mask is stored electronically;
2) The alignment marks on the backside of the wafer are brought in focus;
3) The position of the wafer is adjusted by translation and rotation to align the marks to the stored image.

The exposure is followed by development in AZ 400K developer (Clariant Co., Somerville, NJ) for 30 seconds. This resist does not need hard bake. Thickness of the resist was measured to be 6.28 ± 0.07 μm. It is important to note that for this second mask, which defines the inlet and outlet ports, it is critical to align the ports with the reservoir patterns defined by the first mask in order to realize the fluidic interconnection, as will be discussed later on in Section 4.2.6.

4.2.3 Reactive Ion Etching

After the separation nozzle patterns are obtained in the front side photoresist using photolithography, this resist layer is used as an mask to transferred the patter into silicon.

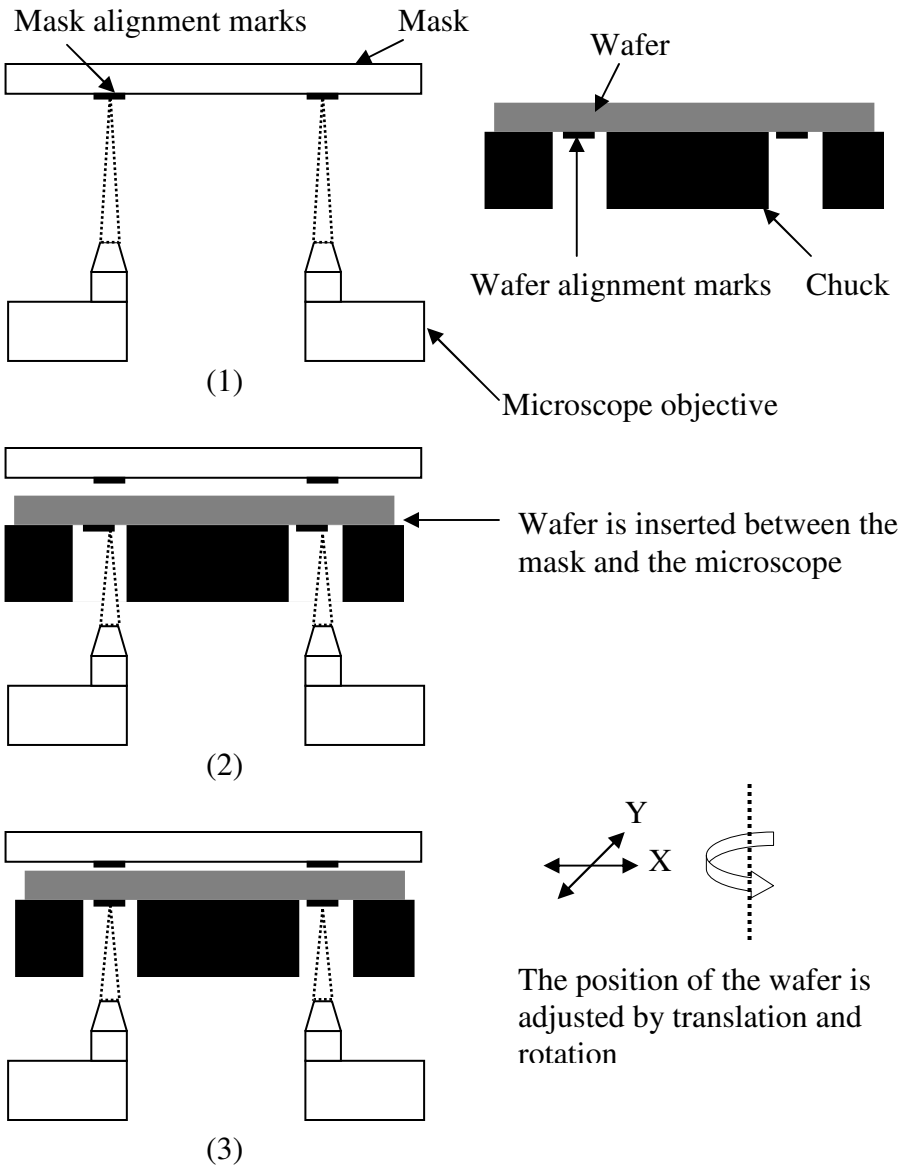

Figure 4.2: Double-sided alignment scheme (adapted from [62]).

This patter transfer was accomplished by reactive ion etching (RIE) using SF_6 and O_2 plasma. The process parameters were pressure of 50 mTorr, flow rates of 40 sccm and 20 sccm for SF_6 and O_2, respectively, and radio frequency (RF) power of 100 W. Test wafers were used to characterized the etch rate and selectivity of silicon to photoresist (hard baked Shipley 1813). Figure 4.3 shows the measured depth of etched structures on

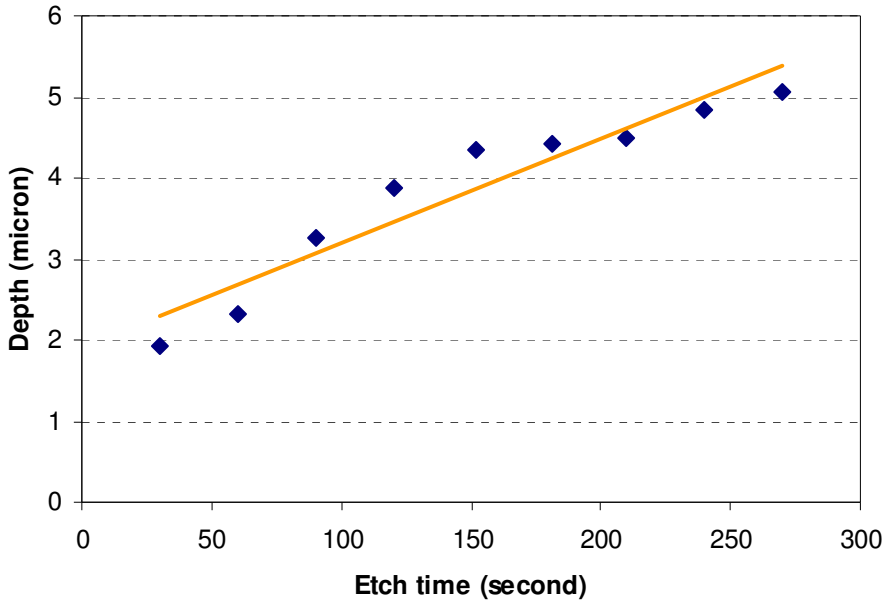

Figure 4.3: Depth measurements of etched structures as a function of time.

a test wafer before stripping the resist. Subsequently, the resist layer was stripped with acetone and the depth of the etched structure was measured again to be 4.27 µm. Therefore, the silicon etch rate and the selectivity to photoresist were estimated to be 0.95 µm/min and 5.5, respectively.

Based on the characterization results, 5 µm deep separation nozzle structures were etched onto a silicon substrate, as shown in Figure 4.4. Using an optical profilometer (model: Veeco WYKO NT1100 Optical Profilometer), the average surface roughness of the etched structure was measured to be less than 20 nm, which is desirable for reducing the viscous effect of gas flow in the device.

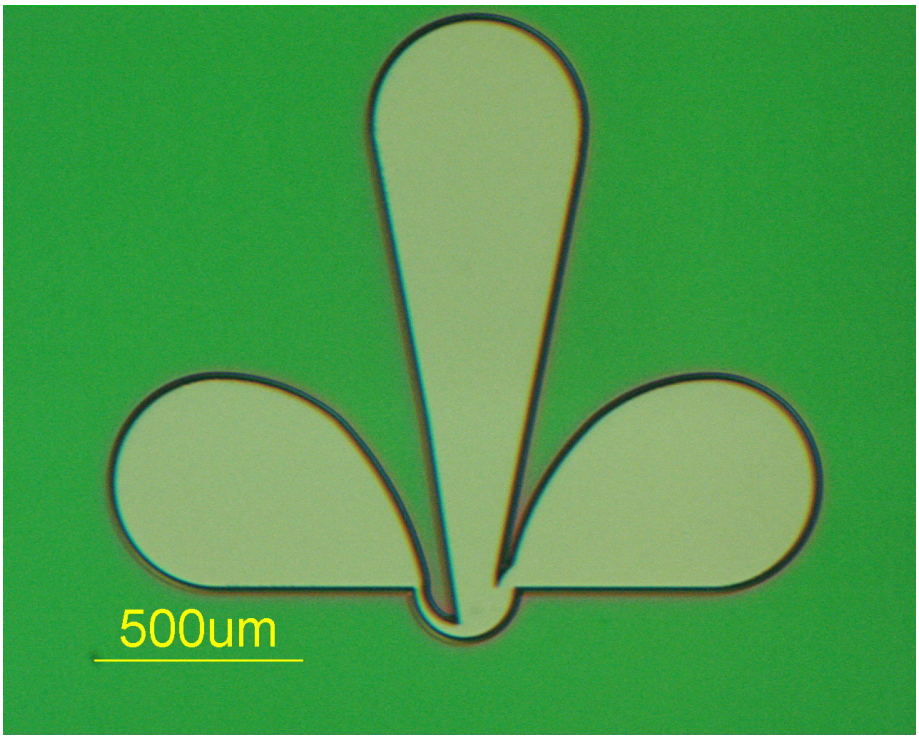

Figure 4.4: Optical micrograph of an etched separation nozzle before stripping the photoresist mask.

4.2.4 Deep Reactive Ion Etching

After the backside lithography as introduced in section 4.2.2, the patterns formed in the photoresist AZ9245 was transferred into the underlying SiO_2 layer to obtain a hardmask suitable for deep reactive ion etching (DRIE). The pattern transfer of the photoresist mask into SiO_2 was accomplished by wet etching using buffered HF (5:1 ratio of 40 wt% ammonium fluoride to 49 wt% hydrofluoric acid). The combination of the patterned photoresist and oxide serves as the etch mask for generating through holes in the silicon substrate using a DRIE system (model: Surface Technology Systems (STS) Advanced Silicon Etch ICP DRIE System).

This DRIE system can provide high aspect ratio etching of single crystal silicon using inductively coupled plasma (ICP) RIE. ICP RIE uses the magnetic field arising from the RF voltage to further excite electron cloud and reactive ions and to increase density of ions and neutrals which increases etch rate. By using the licensed "Bosch process" (i.e., a combination of alternate SF_6 etch and C_4F_8 protection process cycles), high etch rate and high directionality silicon etch is realized [62]. Furthermore, by cooling the wafer chuck to liquid nitrogen temperatures (77K) and using a helium gas flow under the wafer for efficient heat transfer, wafer temperature can be maintained at cryogenic temperatures during etching [61]. The cooling mechanism results in condensation of reactant gases and protects the sidewalls from etching which renders a more anisotropic process [62]. Characteristic parameters of the DRIE Process in the STS system are listed in Table 4.1.

Table 4.1: Process parameters of the STS DRIE system (adapted from [62] and [68]).

SF_6 flow	130 sccm
O_2 flow	13 sccm
C_4F_8 flow	85 sccm
Etch cycle	10 s
Passivation cycle	6.5 s
Pressure	3-30 mTorr
Process chamber temperature	45 ± 1°C
Etch rate	3-4 μm/min
Selectivity to photoresist	~100 to 1
Selectivity to SiO_2	~100 to 1

A handle wafer was used in DRIE to prevent the leak of helium flow. After dispensing several drops of Shipley 1813 on the silicon handle wafer, the device wafer was put on the top of the handle wafer followed by a 5 minute bake on a hotplate at 120°C. Then the bonded assembly was put in the DRIE system, and etching holes (500 μm in diameter) through a 500 μm thick silicon wafer took about 200 minutes. Finally the handle wafer was separated from the device wafer by soaking them in acetone for about 30 minutes.

4.2.5 Anodic Bonding

After DRIE, the device wafer was anodically bonded to a pyrex wafer to seal the etched separation nozzle structures. Before bonding, both wafers were cleaned using RCA cleaning procedures without HF dip to remove organic and ionic contaminants. The pyrex wafer has a nominal mean surface roughness less than 1.5 nm. The surface of the silicon wafer to be bonded with the pyrex wafer was inspected with a atomic force microscope (model: Veeco Dimension 3000 AFM). Figure 4.5 shows the measured surface roughness of the wafer. The mean roughness *Ra* is 0.214 nm, which is desirable for anodic bonding. The anodic bonding was performed on EVG501 Bonder (Electronic Visions Co.), as shown in Figure 4.6. The process parameters used were bonding temperature T= 400 °C, bias voltage 500 V, contact force 500 N, and bonding time 60 minutes. After anodic bonding, the bonded wafers were diced with a dicing saw into several dies. Figure 4.7 shows a microfabricated chip with a close-up view of the curved nozzle structure. The dark holes shown in the photograph are inlet and outlet ports etched through in the silicon substrate using DRIE.

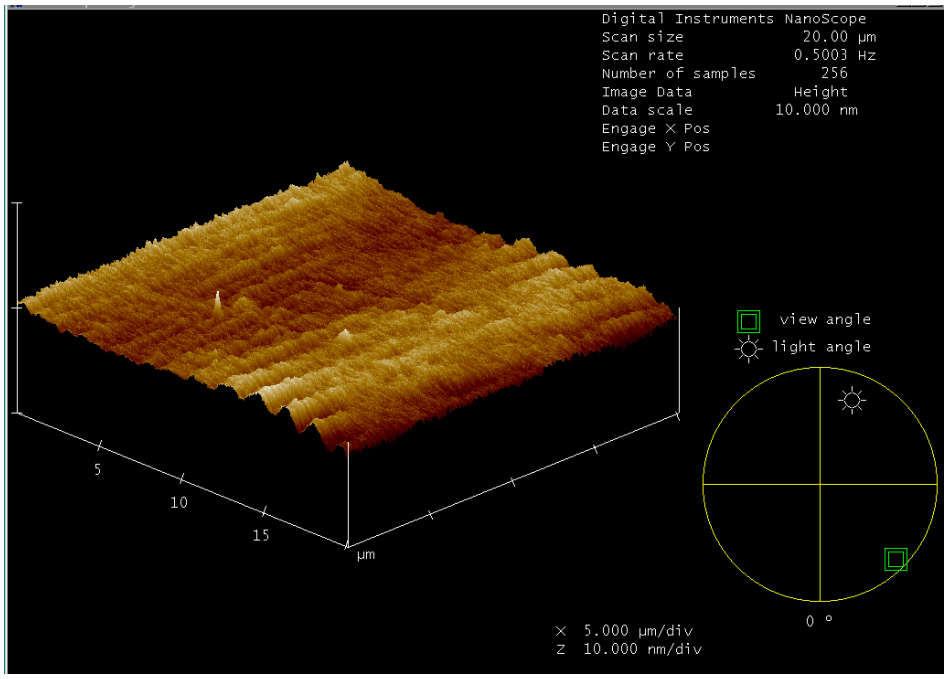

Figure 4.5: AFM micrograph of a device wafer surface before anodic bonding.

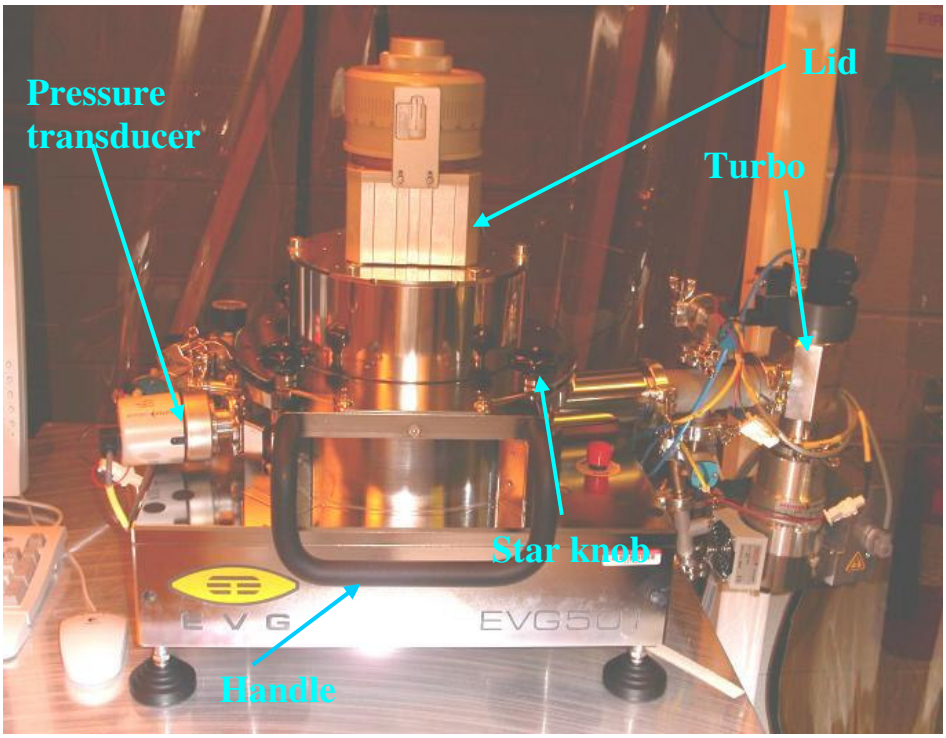

Figure 4.6: EVG501Bonder used for silicon-to-glass anodic bonding.

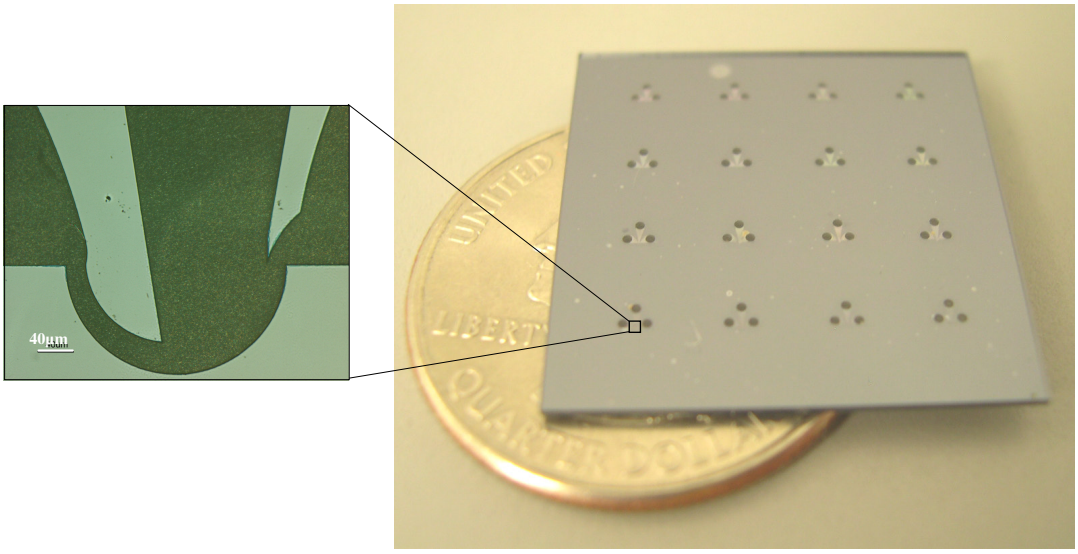

Figure 4.7: Optical micrograph of a microfabricated chip after silicon-to-glass anodic bonding with a close-up view of a single-stage separation nozzle.

4.2.6 Packaging and Mounting

Once the devices are fabricated, they are packaged to realize microfluidic interfacing and prevent leak and contaminants. As shown schematically in Figure 4.1(f), metal capillaries are inserted into the inlet/outlet ports of device and fixed with O-rings and epoxy (not shown) by following the same procedures used for linear test structures as mentioned in Section 2.3. After packaging, the devices are mounted onto a test setup for conducting gas separation experiments. As shown in Figure 4.8, Tygon flexible tubing and fittings are used to connect the device with testing instruments such as flow meter, flow controller, and manometer. The test setup and testing procedures will be discussed in detail in Chapter 5.

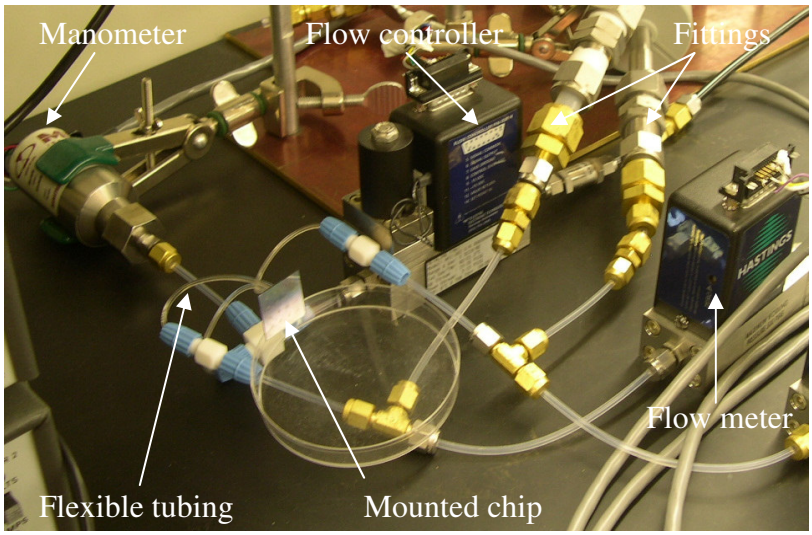

Figure 4.8: View of mounted chip on the test setup.

4.3 Summary

After reviewing some commonly used MEMS fabrication techniques, this chapter presents the process for fabricating the gas separation devices with nozzle throat width as small as 3.6 μm. Device processing consists of a front side photolithography step and a dry-etch step using SF_6 and O_2 plasma to define the separation nozzle structures in silicon. During these steps, test wafers are used to characterize the etch rate of RIE and selectivity of silicon to photoresist; therefore the depth of the etched patterns can be control with precision. A double-sided alignment mechanism is employed to align the inlet and outlet patterns on the backside of the wafer to the reservoirs of the separation devices etched on the front side of the wafer, followed by a DRIE step to generate the ports through the wafer. The microfluidic nozzle structures are then sealed by silicon-to-glass anodic bonding. Finally, the fluidic interconnection techniques developed for the linear test structures are used to interface the gas separation devices with the testing instruments for conducting gas separation experiments.

CHAPTER 5

DEVICE CHARACTERIZATION

5.1 Introduction

In this chapter, the experimental characterization of gas separation devices is presented. First, apparatus and procedures for gas separation experiments are described and mass flow measurements are discussed. Next, the basic principle of mass spectrometry and the corresponding setup for gas analysis are presented. Characterization results using different operating conditions are discussed for various designs. The experimental results are compared to finite-element simulations, and the performance of these devices is evaluated.

5.2 Gas Separation Experiment

Gas separation experiments were conducted to examine the effect of operating conditions (e.g., pressure ratio and gas species) and geometric parameters (i.e., the nozzle width *w* and the skimmer distance *f*) on the separation factor of the fabricated devices. As a proof-of-concept, two different inert gas mixtures, 1 mole% SF_6/99 mole% N_2 and 1 mole % SF_6/99 mole % Ar, were used in the experiments. The mean molecular weigh (MW) of the first mixture is very close to that of air while MW of SF_6 is close to that of some organic contaminants such as trichloroethylene and naphthalene [8], which mimics the working environment of generic miniature chemical sensors. The second mixture was used to study the influence of the mass difference between the heavy component and light component of the mixture on the concentration effect.

5.2.1 Experimental Setup

As shown schematically in Figure 5.1, the setup for conducting gas separation experiments was implemented by modifying the gas flow test setup used for testing linear structures (Figure 2.16). Two 10-cm^3 sample cylinders (SS-4CD-TW-10, Swagelok, Solon, OH), were connected downstream of the device to collect separated gas samples [69]. Figures 5.2 (a) and (b) show the sample cylinder and the gas separation setup, respectively. The inlet pressure P_0 is changed from 1 to 3 atm while the outlet pressures (including the heavy fraction and light fraction ones) are kept at 1 atm, all of which are monitored using manometers (MKS Instruments Baratron 722A and 622A, respectively). The pressure measurements are read simultaneously by a LabVIEW program that is interfaced with a data acquisition device (DAQ) connecting the manometers with a computer. This data acquisition scheme is detailed in Appendix C. Following the separation experiments, the composition of the separated gas samples collected in the cylinders was determined using mass spectrometry. The details of the mass spectrometric setup and gas analysis will be discussed in Section 5.3.

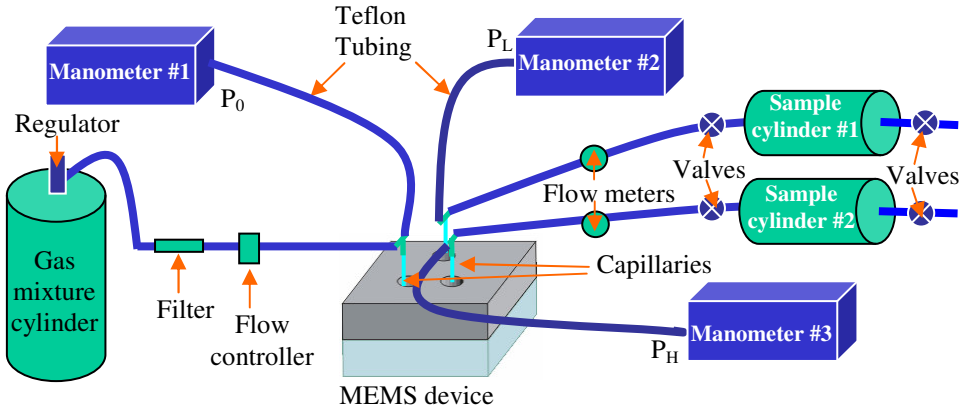

Figure 5.1: Schematic of setup for gas separation experiments.

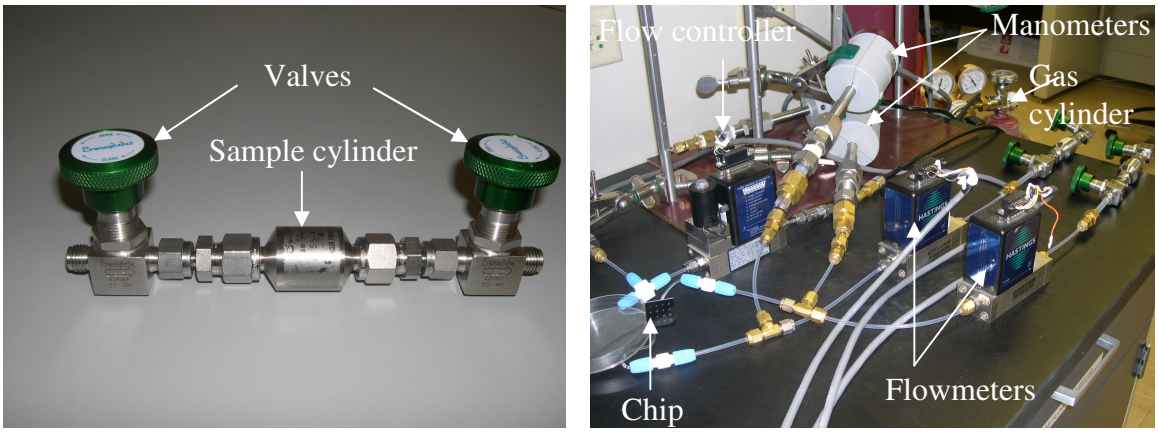

(a) (b)

Figure 5.2: (a) Photograph of a stainless miniature sample cylinder with two stainless bellow valves connected at both ends; (b) the assembly is attached to the setup for gas separation experiments.

5.2.2 Mass Flow Test

As mentioned in Chapter 3, in a separation nozzle system, the total gas stream passing through the centrifugal field is split into a heavy fraction and a light fraction. The gas flow distribution between the heavy and light fractions can be estimated by calculating the partial cuts of the light and heavy components using Equation (3.3), which is repeated below as Equation (5.1).

$$\theta_i(r) = \frac{\exp[(r/r_0)^2 \frac{\gamma}{2} \frac{M_i}{\overline{M}} Ma_m] - 1}{\exp[\frac{\gamma}{2} \frac{M_i}{\overline{M}} Ma_m] - 1} \tag{5.1}$$

Figure 5.3 compares the measured mass flow percentage of the heavy fraction stream with the model calculations for devices 1 and 2, which have different f/r_0 ratios as shown in Table 3.1, which is repeated here as Table 5.1 for the purpose of convenient

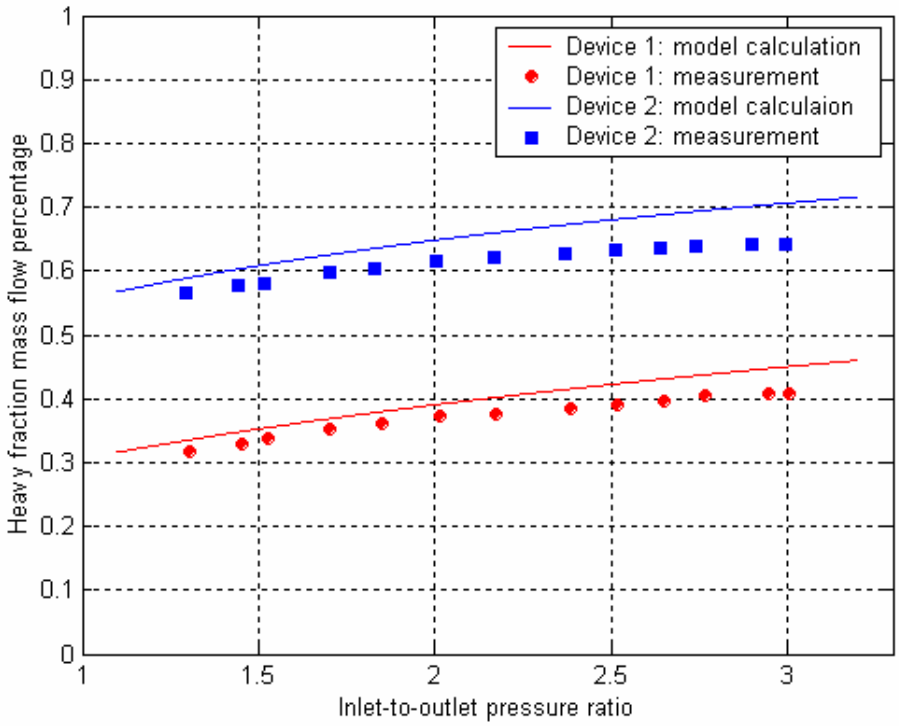

Figure 5.3: Measured mass flow percentage of heavy fraction compared with model calculations for devices 1 and 2 with different f/r_0 ratios, 1/6 and 1/3, respectively.

reference. It is seen that the measurements initially agree well with the equilibrium model, and then deviate slightly from the theoretical predictions as the inlet-to-outlet pressure ratio increases. This is attributed to the increasing width of pressure wave relative to the skimmer distance with rising pressure ratio, as discussed in Section 3.4.

Figure 5.4 compares the estimated residence time from the mass flow measurements with the numerical simulations (Figure 3.10). In the test, the total mass flow rate of device 1 was measured to be from 0.05 to 0.52 sccm, which corresponds approximately to an nozzle exit velocity ranging from 5.9 to 45.4 m/s without considering the thickness of boundary layer of gas flow in the device. With the known

device dimensions, the residence/flow time of the mixture in the centrifugal field is estimated to be less than 0.1 ms. As shown in Figure 5.4, the estimates become gradually close to the numerical predictions with the increasing pressure ratio. This is probably due to the weakening influence of boundary layer with the increasing Reynolds number as the pressure ratio is increased. From both the measurements and simulations, it is demonstrated that high-speed gas separation can be realized through the device.

Table 5.1: Geometric parameters of the three designed separation nozzles.

Device	Radius of deflection wall (μm)	Nozzle throat width (μm)	Skimmer distance (μm)
1	120	18.0	20.0
2	120	18.0	40.0
3	120	3.6	20.0

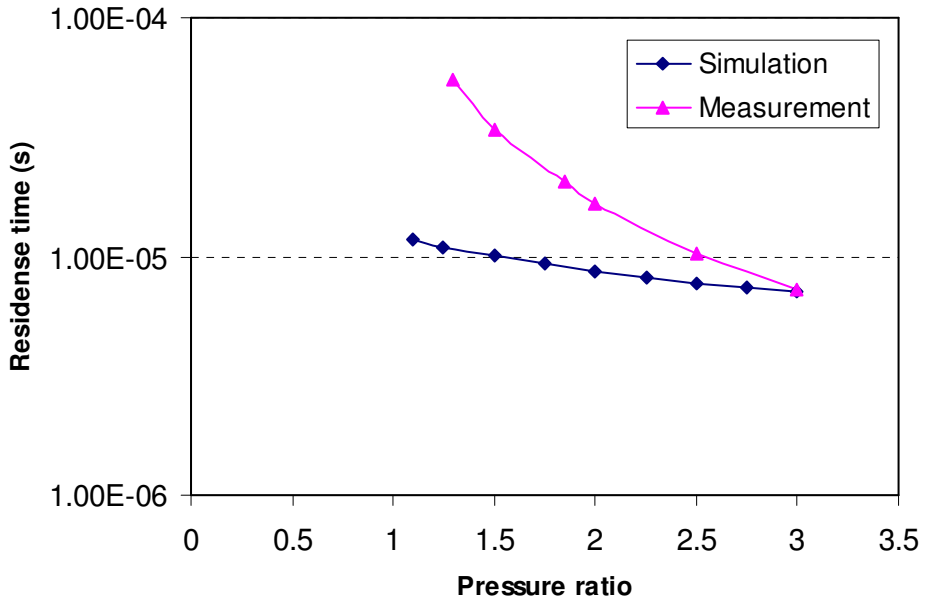

Figure 5.4: Simulated residence time versus pressure ratio in comparison with the estimate from the mass flow measurements.

5.3 Mass Spectrometric Gas Analysis

5.3.1 Principle of Mass Spectrometry

Mass spectrometry is used to analyze separated gas samples. The operating principle of a quadrupole mass spectrometer is shown in Figure 5.5 [70]. It is composed of an ion source, a separation system, and an ion detector. First, injected gas molecules are ionized by impact electrons (an electron energy level of 70-110 eV). The ion beam extracted from the ion source is diverted into the quadrupole separation system containing four rod-shaped electrodes. The cross sections of the four rods form the circle of curvature for a hyperbola so that the surrounding electrical field is nearly hyperbolic. Each of the two opposing rods exhibits equal potential, this being a DC voltage and a superimposed high-frequency AC voltage (i.e., $V_0+V\cos\omega t$). The voltages applied induce transverse oscillations in the ions traversing the center, between the rods. The electrical field Φ inside the separation system is

$$\Phi = (V_0 + V\cos\omega t).(x^2 - y^2)/r_0^2 \tag{5.2}$$

where x and y are the coordinates of the ion traveling in the field, r_0 is the radius of the cylinder which can be inscribed inside the system of rods. It is demonstrated that there are stable and unstable ion paths. With the stable paths, the distance of the ions from the separation system center line always remains less than r_0 (passage condition). With unstable paths, the distance from the axis will grow until the ion ultimately collides with a rod surface; the ion will be neutralized, thus becoming unavailable to the detector [74]. In other words, only the ions with a certain mass to charge ratio (m/q) can pass through the separation system and then be detected.

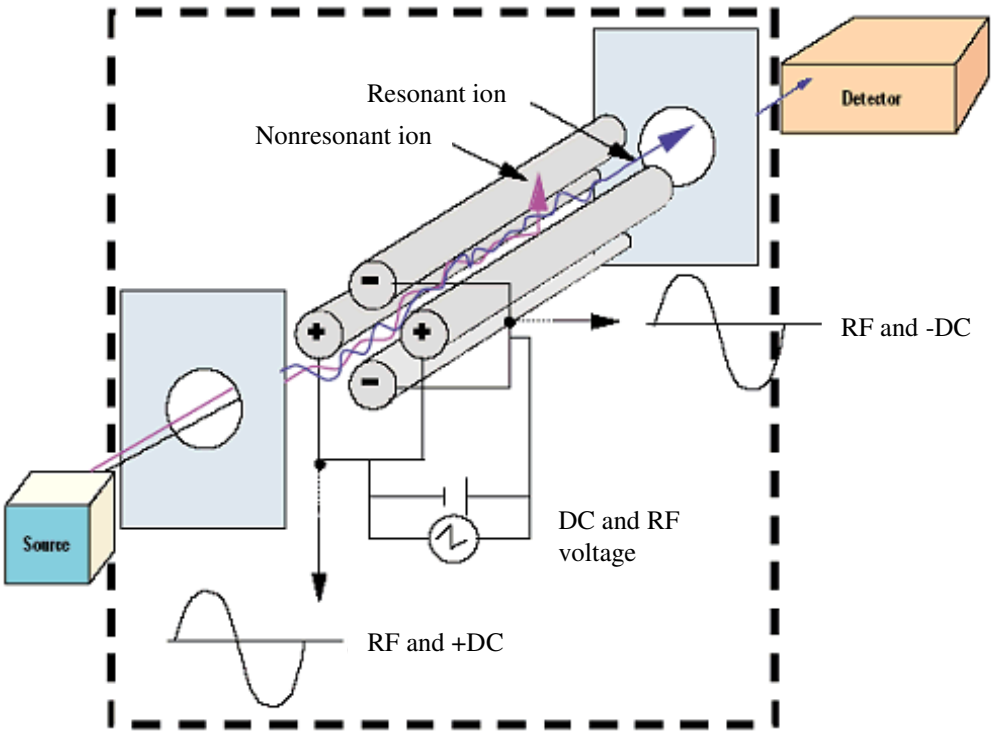

Figure 5.5: Operating principle of a quadrupole mass spectrometer (adapted from [70]).

After leaving the separation system, the ions will meet the ion trap or detector, which, in the simplest instance, will be in the form of a Faraday cup [74]. Figure 5.6 (a) illustrates schematically the basic configuration of a Faraday ion trap connected with the output of the separation system and an electrical amplifier while Figure 5.6 (b) shows a flanged-mounted Faraday cup. The ions that impinge on the detector will be neutralized by electrons from the ion trap. After electrical amplification, the measurement signal is ion current, corresponding to the "ion emission stream". To achieve greater sensitivity, a secondary electron multiplier pickup (SEMP) can be employed in place of the Faraday cup [74].

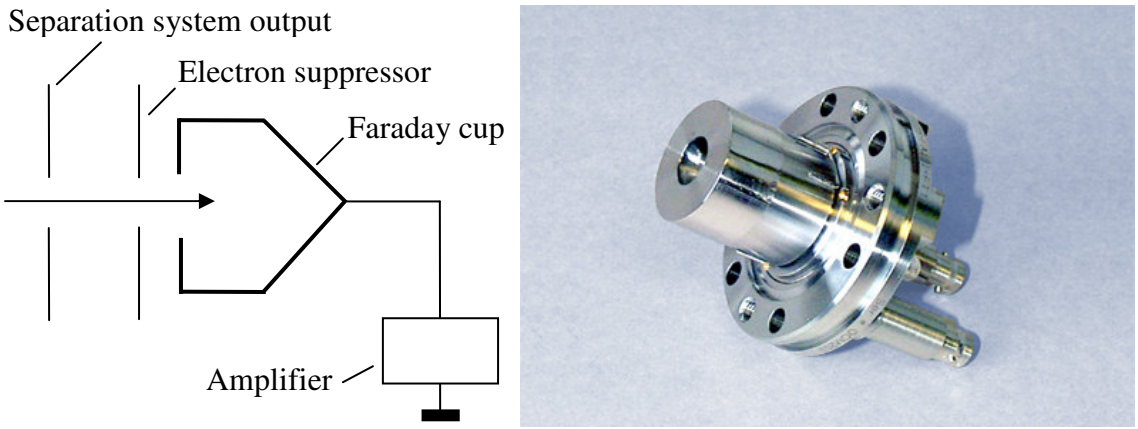

(a) (b)

Figure 5.6: (a) Principle of the Faraday cup; (b) Photograph of a flanged-mounted Faraday cup [71].

5.3.2 Evaluation of Mass Spectra

In the mass spectrometric gas analysis, an electron energy of 70-110 eV was used to ionize gas molecules. At this energy level, in a high vacuum, the interaction between electrons and molecules leaves some ions with so much extra energy that they break up to give ions of smaller mass. This fragmentation is characteristic for a given substance [72]. For example, SF_6 molecules are often broken down into 13 different fragment patterns, some of which are of negligible intensity compared to the highest fragment peak, in this case, at mass 127, as illustrated in Figure 5.7 [73]. Consequently, in the experiments, the six strongest fragments (i.e., masses 127, 89, 108, 129, 51, and 70) are counted to evaluate the concentration of SF_6 in the mixture.

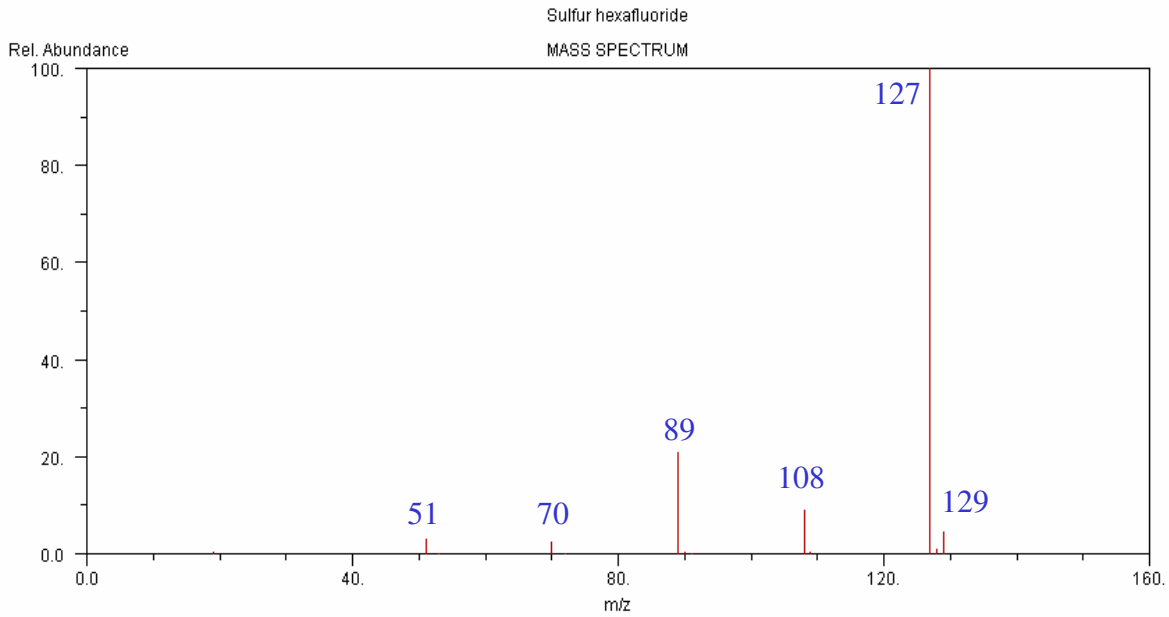

Figure 5.7: Standard mass spectrum of SF_6 (adapted from [66]). Six fragments (i.e., masses 127, 89, 108, 129, 51, and 70) are of significant intensity and counted to evaluate the ion abundance of SF_6.

5.3.3 Experimental Setup

A mass spectrometric gas analysis setup was implemented to characterize the separation effect of the developed single-stage devices. As shown in Figure 5.8, the setup consists of a mass spectrometer (Transpector CIS TS200, Inficon, East Syracuse, NY) with a mass range of 200 atomic mass units (amu), a vacuum chamber, a turbomolecular pump, and a mechanical pump (not shown in the figure). The sample cylinder is connected to the vacuum chamber through a 1-μm orifice to control the gas flow, so the vacuum can be maintained at a desirable level for effective electron ionization.

Before measuring the separated gas samples, the mass spectrometer was calibrated for using pure SF_6. Figure 5.9 displays the six strongest SF_6 fragment peaks after calibration. Before calibration, these peaks were either of irregular shape or off their

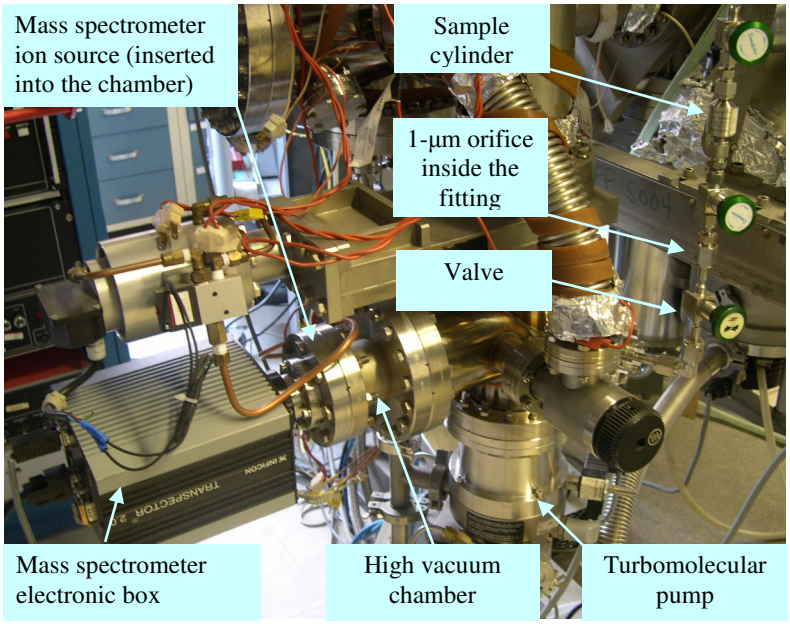

Figure 5.8: Setup for mass spectrometric gas analysis. The sample cylinder is connected to the vacuum chamber through a 1-µm orifice to control the gas flow, so the vacuum can be maintained on a desirable level for effective electron ionization.

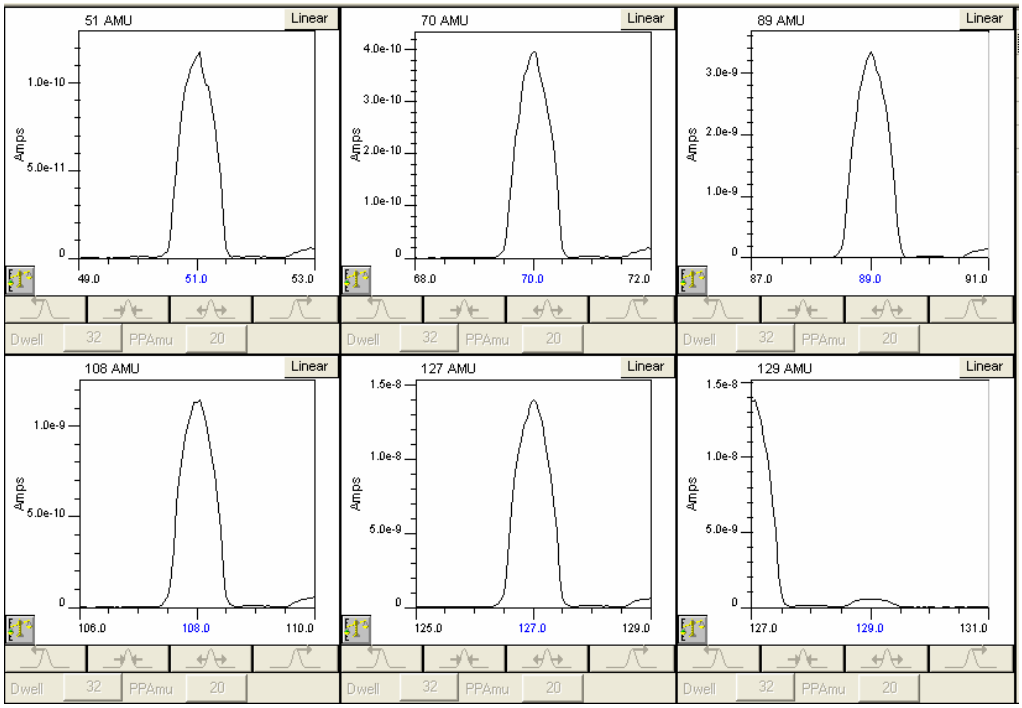

Figure 5.9: The six strongest fragment peaks of SF_6 are shown properly after manually calibrating the mass spectrometer.

proper mass positions. In practice, differing ionization rates for individual gases need to be taken into account by standardization against nitrogen. In the next calibration step, the relative ionization probability (RIP) of SF_6 in relationship to nitrogen is measured with a known mixture of SF_6/N_2 (i.e., 1 mole% SF_6 and 99 mole% N_2). The RIP of SF6 was determined to be 2.33, which was quite close to the value of 2.30 published in [74]. Once the mass spectrometer was calibrated, it was employed to analyze the separated gas samples to characterize the performance of the fabricated devices.

5.4 Results and Discussion

5.4.1 Characterization of Separation Effect

Figure 5.10 compares the mass spectra of (a) SF_6 and (b) N_2 between the heavy fraction and light fraction streams [75]. Device 2 in Table 5.1 was used in the gas separation experiment with an inlet-to-outlet pressure ratio of 2. The molar fraction of SF_6 in the heavy fraction stream is increased by about 33 % relative to the gas mixture before separation, as seen from the increased total ion abundance of the SF_6 fragments while the ion abundance of main N_2 fragments (i.e., masses 14, and 28) remains relatively unchanged with deduction of fragmentation patterns of N_2 contributed by the residual air trapped in the sample cylinder.

The separation factor was obtained by evaluating the partial cuts of SF_6 and N_2, as defined in Equation (3.1), which is repeated here as Equation (5.3):

$$A = \frac{\theta_l (1-\theta_h)}{\theta_h (1-\theta_l)} \tag{5.3}$$

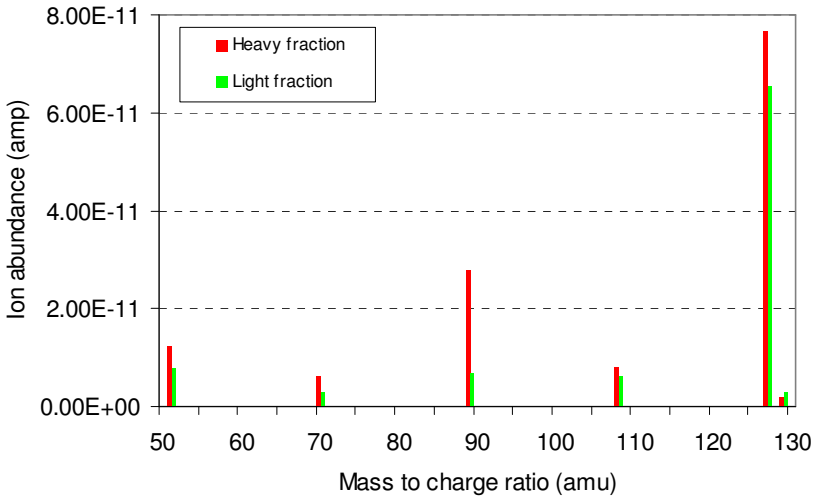

(a)

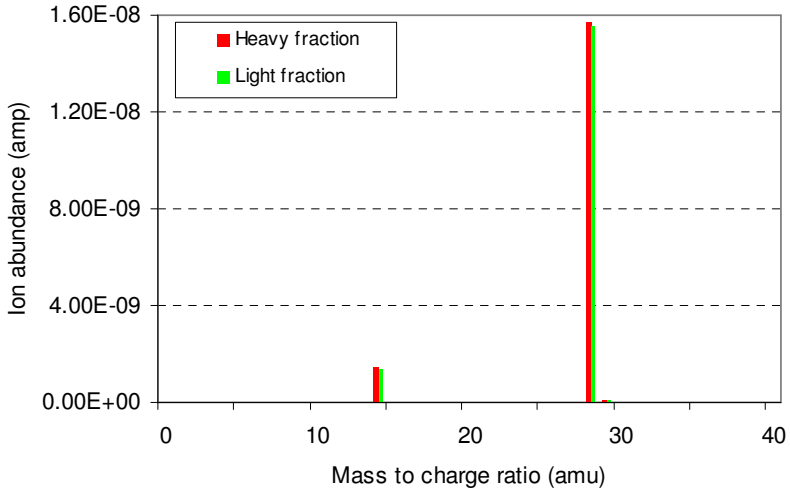

(b)

Figure 5.10: Comparison of mass spectra of (a) SF_6 and (b) N_2 between the heavy fraction stream and light fraction stream. Noticeable enrichment of SF_6 is achieved in the heavy fraction, as seen from the increased total ion abundance of the SF_6 fragments while N_2 is kept the same as indicated by the ion abundance of main N_2 fragments (i.e., masses 14 and 28).

The partial cut of SF_6 or N_2 as defined in Equation (3.2) is evaluated by comparing the ion abundance of SF_6 or N_2 between the heavy fraction and light fractions streams. Figure 5.11 compares measured separation factor (A) to the finite element simulations and analytical predictions using (5.1) and (5.3) for design 1 as listed in Table 5.1. The

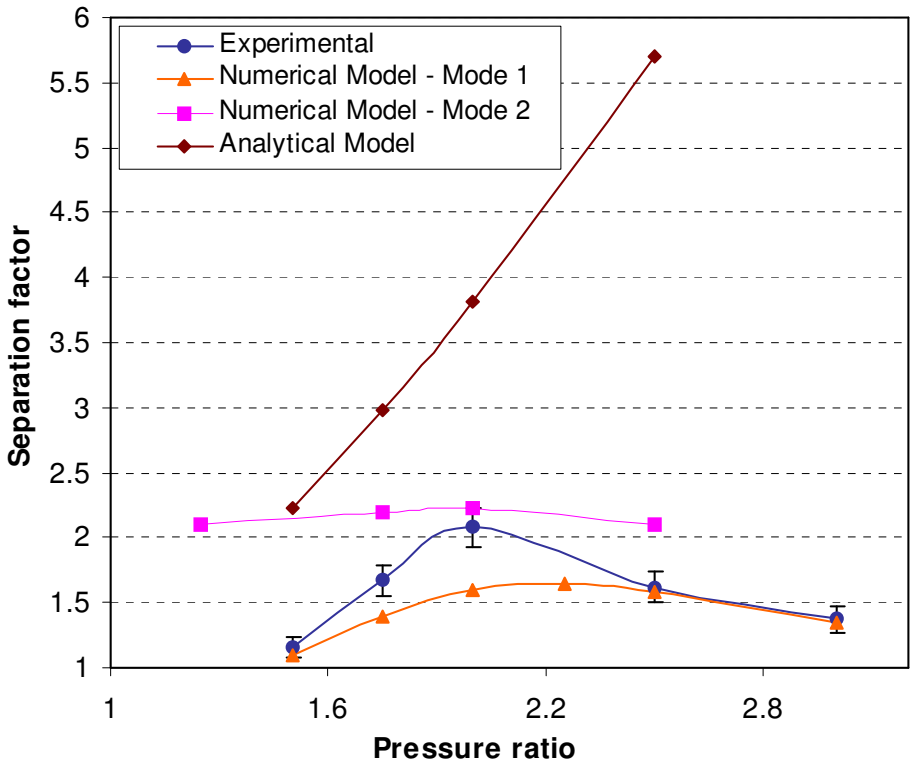

Figure 5.11: Comparison of the experimental determinations of the separation factor with the predictions of the analytical and numerical models.

experimental and numerical curves show that *A* initially rises with increasing pressure ratio, passes through a maximum, and then drops. The peak separation factor occurs at a pressure ratio of approximately 2.0, which is attributed to the optimum combination of high pressure gradient and a contained pressure wave matching the skimmer, as explained in Section 3.4. The analytical model shows the monotonic increase of A with pressure ratio because the equilibrium separation is proportional to the Mach number and in turn the pressure ratio for the isentropic mixture flow. The measurement uncertainties primarily originate from two sources: the first one is the fluctuation of the ion abundance measurement of gas molecule; the second source is the interference of the trapped air in the sample cylinder to the analysis of the mass spectra of the separated gas samples.

Figure 5.12 shows the measured A of the N_2/SF_6 mixture versus pressure ratio for all of the three designs in Table 5.1. It is seen that all curves exhibit a peak. Besides the explanation above, another way to explicate the variation of A with pressure ratio is the competition between the separating pressure diffusion and remixing concentration diffusion. The dependence of A on the pressure ratio, on the one hand, is determined by the increasing separating pressure diffusion as a result of the increasing pressure ratio. On the other hand, the remixing azimuthal transport increases as a result of higher molar fraction gradients of SF_6 molecules associated with increasing inlet pressure. When the remixing concentration diffusion streams exceed the separating pressure diffusion streams at high inlet pressures, A begins to drop. It is evident from the data that controlling the inlet pressure is critical for efficient separation of gas mixtures if the

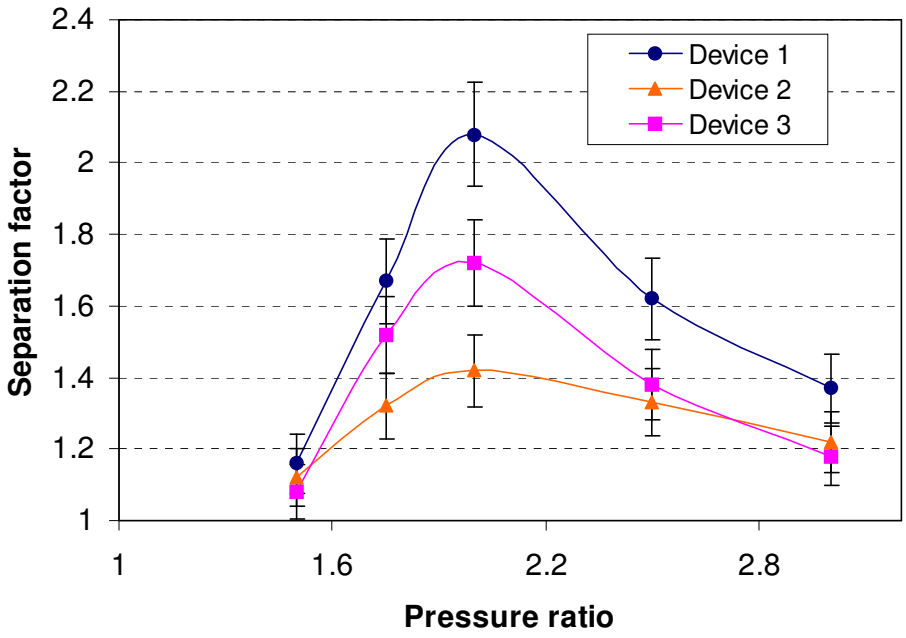

Figure 5.12: Separation factor A of the mixture of 99 mole % N_2 and 1 mole % SF_6 versus pressure ratio for the three designed devices.

outlet pressure is kept constant. This observation is consistent with the results from the separation experiments using the gas mixture of H_2/C_7F_{14} [24], as illustrated in Figure 5.13.

Also worth noting from Figure 5.12 is that device 1 shows strongest concentration effect among the three designs. At the inlet pressure of two atmospheres, corresponding to the highest A, SF_6 molar fraction of the heavy fraction stream is evaluated to be 2.14 ± 0.15 mole%. In comparison to device 3, the increased a/r_0 ratio of device 1 leads to a relatively long radial transport path for gas molecules and therefore stronger separation effect. It should be noted that a/r_0 ratio cannot not be designed arbitrarily big as the geometry and dimension of the input converging-diverging nozzle

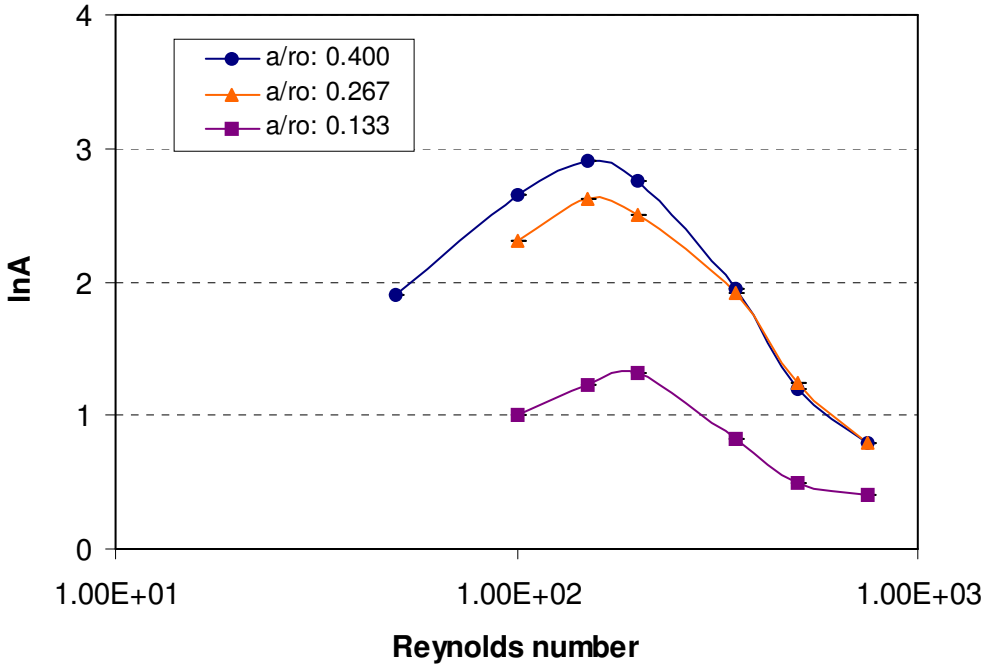

Figure 5.13: Separation factor A of an H_2/C_7F_{14} mixture (95 mole% H_2 and 5 mole% C_7F_{14}) versus Reynolds number Re for various normalized widths a/r_o of the standard separation nozzle (adapted from [24]).

must be maintained to accelerate the gas flow efficiently. The lowest concentration efficiency shown by device 2 is mainly due to its increased skimmer distance. Since heavy molecules are pushed more closely towards the deflection wall than light ones, a smaller skimmer distance *f* is preferred to obtain enriched heavy molecules in the heavy fraction stream. However, considering the trade-off between the separation factor and mass flow percentage of the heavy fraction stream, *f* should be designed carefully, especially for a multi-stage gas concentration device (i.e., a cascade of single-stage separation elements).

As indicated in Equation (5.1), the separation effect of the separation nozzle is dependent on the mass difference between the heavy and light components of a gas mixture. In order to characterize the influence of the mass difference on the separation factor, another gas mixture of 1 mole% SF_6 and 99 mole% Ar was used for the gas separation experiments. Figure 5.14 compares the mass spectra of (a) SF_6 and (b) Ar between the heavy fraction and light fraction streams. It is shown that in the heavy fraction stream the total ion abundance of SF_6 fragments is increased while that of Ar fragments is decreased, demonstrating the enrichment of SF_6 molecules diluted in Ar. It should be noted that one of the main SF_6 fragments, Mass 129, is not shown in Figure 5.14 (a) due to its negligible abundance.

Figure 5.15 compares the separation effects of device 1 and device 3 at different pressure ratios for the two gas mixtures N_2/SF_6 and Ar/SF_6. As shown in Figure 5.15, both devices exhibit weaker separation effect for the mixture Ar/SF_6 than for N_2/SF_6. This is attributed to the smaller mass difference between Ar (MW of 40 amu) and SF_6 (146 amu) than that between N_2 (28 amu) and SF_6 that results in weaker pressure

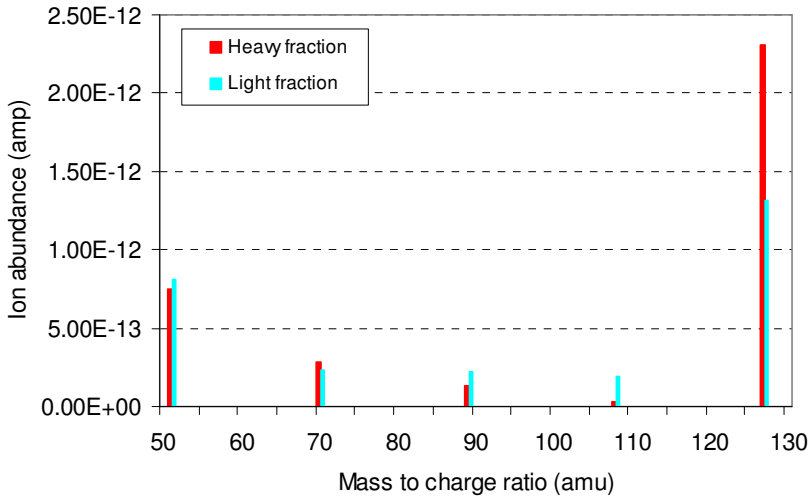

(a)

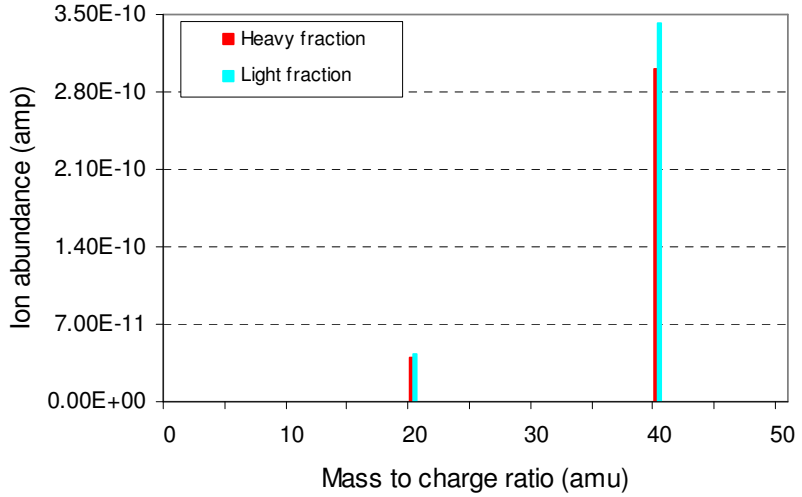

(b)

Figure 5.14: Comparison of mass spectra of (a) SF_6 and (b) Ar between the heavy fraction stream and light fraction stream using the gas mixture SF_6/Ar. SF_6 is enriched in the heavy fraction, as indicated from the increased total ion abundance of the main SF_6 fragments and decreased abundance of the main Ar fragments (i.e., masses 20 and 40).

gradients established in the flow field. In addition, the mean MW of the Ar/SF_6 mixture is larger than that of N_2/SF_6, therefore the gas velocity of Ar/SF_6 is relatively small with the same pressure ratio. This observation is consistent with the theoretical prediction by

Equation (5.1). Also worth noting from Figure 5.15 are the shorter error bars for Ar/SF_6 curves than those for N_2/SF_6 ones. This is because of the very small concentration of Ar in air. The contribution of Ar from residual air trapped inside the sample cylinder is negligible as compared to that from the separated gas sample, which improves the measurement accuracy.

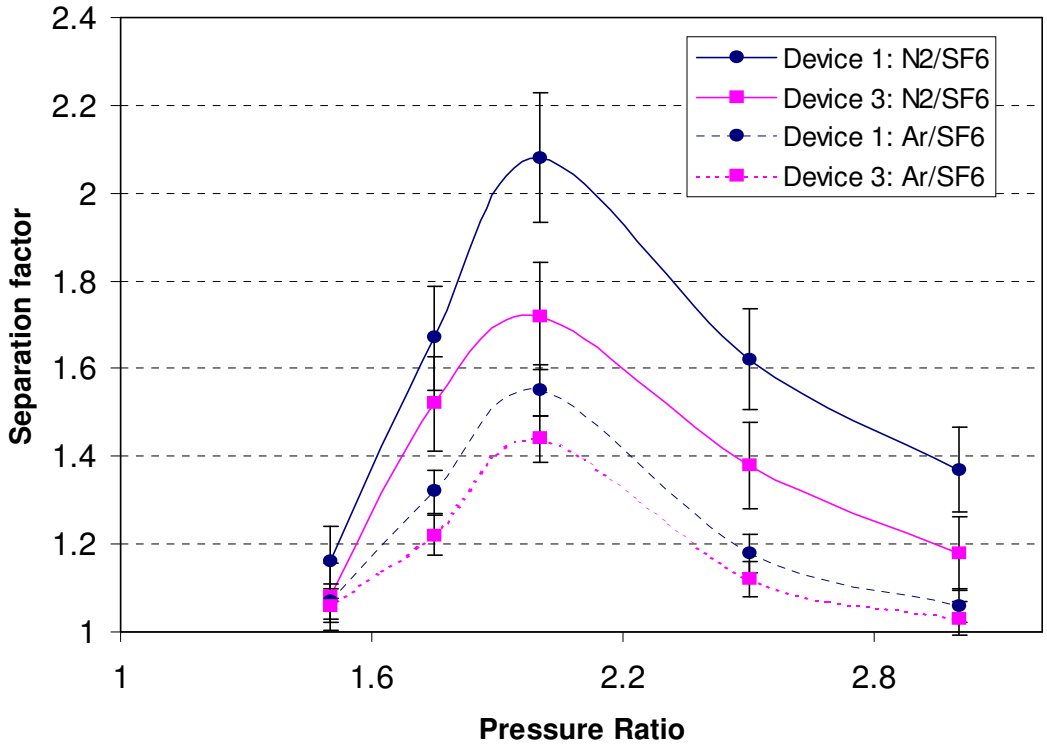

Figure 5.15: Variation of separation factor *A* of mixtures N_2/SF_6 and Ar/SF_6 as a function of pressure ratio for device 1 and device 3.

5.4.2 Evaluation of Device Performance

While the results above demonstrate fast concentration of heavy gas molecules, the concentration effect indicated by the separation factor of the single-stage separation elements is much lower than that of the commonly used chemical affinity methods such

as sorbent beds or permeable membranes (i.e., concentration factor is in the range of 10-10000) [17, 18]. However, the single-stage elements can be cascaded to form a multi-stage preconcentrator whose concentration efficiency is ideally enhanced exponentially with the number of the cascading stages. Therefore, the concentration effect of the cascaded system can be controlled by adjusting the number of single-stage elements. Further investigation is needed to characterize the influence of operating conditions such as pressure ratio on the concentration effect since larger pressure losses and more complicated non-equilibrium effects are anticipated in the multi-stage device.

It should also be noted that the gas separation device has a potential drawback of poor selectivity when applied to separating a gas mixture of multiple components with similar molecular weights. Therefore, the gas separation device developed in this research is best suited to serve as a real-time preconcentrator for a miniaturized sensor with a good selectivity (e.g., a mass-spectrometer-on-a-chip) to detect/analyze trace amounts of volatile chemical compounds in air, which is very common in environmental monitoring.

5.5 Summary

This chapter first presented the mass flow measurements compared with theoretical predictions. Then the basic principle of mass spectrometry, the configuration of the developed mass spectrometric system as well as the analysis of separated samples were discussed. The operation of the three designed devices was characterized using two different gas mixtures. The experimental results demonstrated more than two-fold enrichment of SF_6 in the heavy fraction stream by a single-stage separation device. The

effects of the design parameters (i.e., the nozzle width and skimmer distance) and the operating condition (i.e., the inlet-to-outlet pressure ratio and mass difference of the heavy and light components of the gas mixture) on the device performance were examined experimentally and compared to the simulation results. Finally, issues related to cascading the single-stage separation elements into a real-time preconcentrator were discussed for environmental sensing applications.

CHAPTER 6

CONCLUSION

6.1 Introduction

This chapter summarizes the accomplishments of this PhD dissertation research by reviewing the contributions of each chapter. Future work on developing a multistage separation nozzle based preconcentrator is discussed. Finally, an outlook for developing a on-chip chemical detection microsystem is given along with a brief description of its pumping and sensing modules.

6.2 Summary of Current Research

This PhD research is devoted to the design, fabrication and characterization of micronozzles for gas sensing applications. The feasibility of separation nozzle based preconcentration has been demonstrated. Compared to the chemical affinity methods, this approach overcomes the limitations associated with the absorption/desorption or permeation of molecules being concentrated. Therefore, system response time can be enhanced greatly. Although the separation nozzle method was originally developed to enrich uranium isotopes for production of light water reactor fuel, none have utilized it for chemical sensing applications. This dissertation research is summarized below by highlighting the significant contributions of each chapter.

After a brief introduction of MEMS technology and microfluidic devices, Chapter 1 presents a comprehensive review of existing gas concentration techniques as well as their advantages and drawbacks. Based on the information provided by the literature, the

separation nozzle method is proposed to concentrate gas molecules of interest for environmental sensing applications where the objectives of this research are outlined.

Linear test structures, which are designed to characterized viscous effects in microfluidic devices, are discussed in Chapter 2. A 1-D isentropic model and an ANSYS CFD model are introduced to describe the behavior of gas flows in linear micronozzles. Two processes are explored to fabricate the micronozzles, and their respective advantages and disadvantages are identified. Following the device fabrication, details about the device packaging and testing are presented. The experimental results demonstrate that a sonic flow is reached at the throat area of the nozzle. The viscous effects in the micronozzles are characterized by comparing the measured mass flow rates with the theoretical predictions using the isentropic model.

Chapter 3 reviews the basic theory of separation nozzle method. An equilibrium model is derived to describe the separation and diffusion processes in the separation nozzle system. Design considerations of single-stage separation nozzle systems based on the results from the linear structures are addressed. CFD modeling based on the compressible Euler equations and Maxwell-Stefan diffusion equation is conducted to study the separation nozzle flows. The simulation results reveal the relationships between the separation factor and the pressure ratio, and enhance the physical understanding of device operation.

In Chapter 4, commonly used MEMS fabrication techniques are reviewed. The fabrication process for the gas separation devices is presented with emphasis on the characterization of each step. Specifically, during RIE etch step, test wafers are used to characterize the etch rate of RIE and selectivity of silicon to photoresist; therefore the

depth of the etched patterns can be control with precision. After fabrication, device packaging and mounting is presented. These developed fabrication and packaging techniques for the linear test structures and micro separation nozzles can be easily extended to produce other microfluidic devices and realize fluidic interconnection.

Chapter 5 presents the apparatus for gas separation experiments and mass spectrometric gas analysis. The effects of the design parameters and the operating conditions on the performance of gas separation devices are characterized experimentally and compared to the numerical simulation results. Both demonstrate more than two-fold enrichment of SF_6 in the heavy fraction stream with a response time on the scale of 0.01 ms for a single stage separation device.

Base on the research results summarized above, it is demonstrated that micro separation nozzles are suitable for fast gas concentration. This PhD dissertation research has laid the groundwork for developing separation nozzle based real-time preconcentrators to enhance the sensitivity of miniature chemical sensors. The presented experimental techniques and theoretical models in this dissertation can be extended to develop other microfluidic devices.

6.3 Future Work

The current study focuses on the design, fabrication and testing of linear micronozzles and single-stage separation nozzle systems. Future work will include the development of multi-stage versions for real-time concentration applications, as shown schematically in Figure 6.1. The feed gas, entering on the left, flows through the separation nozzle stages and finally to the outlet on the right. The light fraction streams

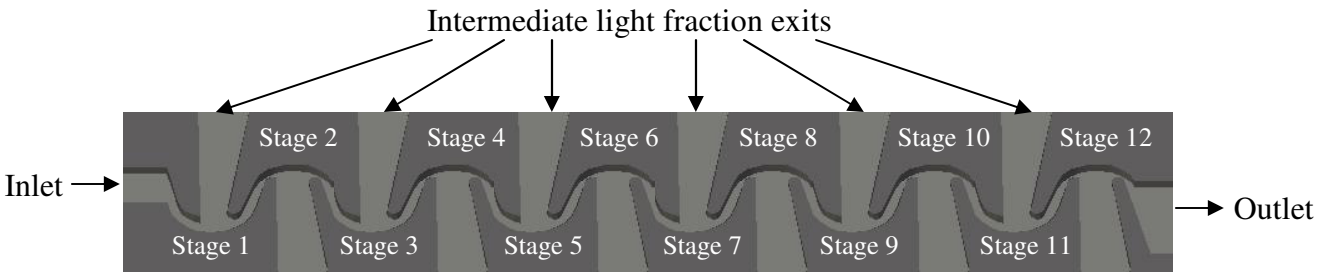

Figure 6.1: Schematic of a multi-stage separation nozzle system.

leave the separation elements at the top and bottom exits while the heavy fraction stream, passing through the whole length of the separation system with concentrated species, exits the system through the outlet. Further investigations on cascading the separation elements to minimize pressure losses due to the curved flows and viscous effects are required to understand their influence on the concentration efficiency. Another worthwhile investigation is a study of the experimental apparatus to determine if the two simulated flow modes discussed in Section 3.4.4 are actually realized within the device.

Moreover, research effort can be made to explore the feasibility of developing a on-chip chemical detection scheme that incorporates gas sampling, preconcentrating and sensing into a system for real-time and quantitative determination of chemical vapors. The microsystem mainly consists of a sampling pump, a separation nozzle-based preconcentrator, and an array of conducting polymer chemically sensitive resistors as an electronic nose, as illustrated conceptually in Figure 6.2 (not showing the encapsulating glass cover with an inlet for injection of gas samples and circuits for the micropump and sensor array). The sampling and sensing modules of the microsystem will be described briefly below.

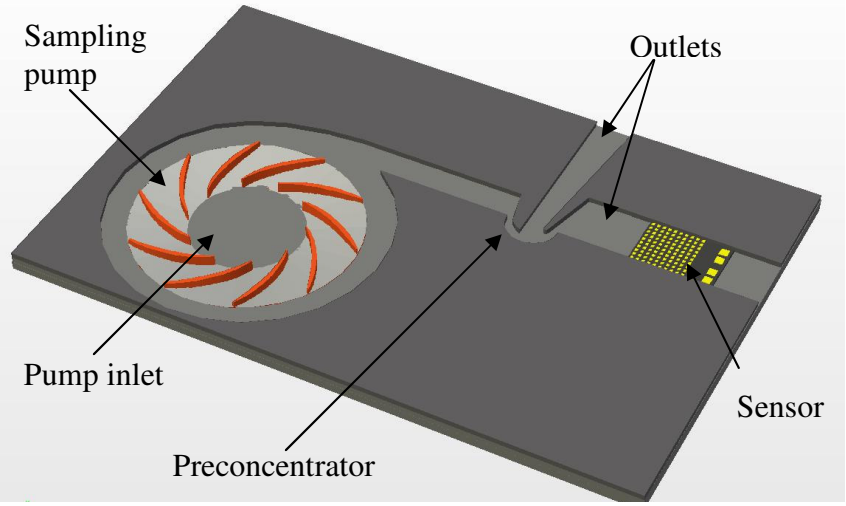

Figure 6.2: Conceptual schematic of the main modules of the proposed on-chip chemical detection system.

The sampling micropump consists of a rotor supported by microball bearings and driven by an integrated variable capacitance micro motor with power electronics. Flow is produced by a pressure difference between the input and output of the pump by spinning the rotor at high speeds up to 100,000 rpm. One of the key parameters to consider in designing such a pump is the geometry of the rotor. Current designs are limited by planar silicon fabrication causing low mass flow efficiencies. Researchers at MSAL have developed a fabrication technology over the past five years that allows for arbitrary 3-D shaping of the silicon [76]. This will be utilized in the design of the rotor geometry for highly increasing the performance of the micropump. Researchers at MSAL have also investigated the microball bearing technology and low-*k* polymer-based dielectrics that enable the development of the integrated variable-capacitance micromotor [77]. Currently, the micropump is being investigated by Mr. Mike Waits at MSAL and the Army Research Lab for his PhD research.

The so-called electronic nose sensing mechanism is comprised of an array of sensors that individually respond to vapors, producing a distinguishable response pattern for each analyte [78-81]. Specifically, when a conducting polymer film is exposed to a gaseous vapor, some vapor molecules enter the film and cause the film to swell. This vapor-induced film swelling increases the electrical resistance of the film by decreasing the number of connected pathways of the conducting component in the film [92]. Compared to other chemical detection techniques such as microcantilevers, surface acoustic wave (SAW) microsensors and metal-oxide thick films [8, 62], this proposed module is relatively simple and readily fabricated and operated. The electronic nose technology is discussed more in Appendix D.

This proposed integrated chemical detection microsystem is inherently miniaturized and mass-producible, hence it can serve as a reliable template for developing a portable or handheld instrument for trace detection of volatile and semi-volatile chemical vapors, and is expected to form the basis for developing integrated, massively distributed sensor networks that would provide enhanced surveillance capabilities and human protection.

APPENDIX A

BASIC THEORY OF COMPRESSIBLE FLUID FLOW

A.1 Introduction

In this appendix, the basic theory of compressible fluid flow is reviewed. First, the compressibility of a fluid is introduced. Next, the fundamental assumptions of gas dynamics are discussed. Finally, gas flow behavior in converging-diverging nozzles is discussed with emphasis on the Mach number distribution.

A.2 Compressibility

The compressibility of a fluid is defined as the measure of the change in density of the fluid caused by a specified change in pressure. Specifically, gases are highly compressible whereas most liquids have a very low compressibility [38]. In a compressible fluid flow, there are usually changes in pressure associated with changes in the velocity in the flow. These pressure changes will induce density changes that will have an influence on the flow. If these density changes are important, the temperature changes in the flow associated with the velocity changes also influence the flow. In other words, when compressibility is important, the temperature changes in the flow are usually significant. Classical incompressible fluid mechanics deals with the situations in which the effects of the changes in density and temperature are negligible. In some cases, however, those density and temperature changes have a very significant influence on the flow. The study of fluid flows where compressibility effects are important is known as gas dynamics [38].

A.3 Fundamental Principles and Aspects of Compressible Flow

The flow field is basically described by knowing the values of the following variables at all points in the flow field: velocity (V), pressure (P), density (ρ), and temperature (T). Therefore, in order to describe the flow field, four equations involving these four variables must be obtained [38]. These equations are derived by applying the following principles [82]:

- Conservation of mass (continuity equation)
- Conservation of momentum (Newton's second law of motion)
- Conservation of energy (first law of thermodynamics)
- Equation of state

The principle of conservation of mass requires that the rate at which mass enters through the left hand of the control volume be equal to the rate at which mass leaves through the right hand face of the control volume, as shown in Figure A.1. Therefore,

$$\rho_1 V_1 A_1 = \rho_2 V_2 A_2 \tag{A.1}$$

where A is the cross-sectional area of the duct at the section considered.

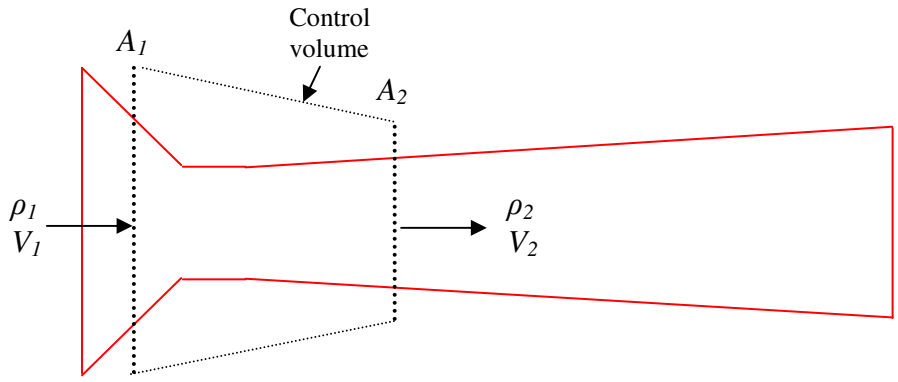

Figure A.1: A converging-diverging nozzle with two cross sections A_1 and A_2.

The equation of state gives

$$P_1/(\rho_1 T_1) = P_2/(\rho_2 T_2) = R = \Re/m \tag{A.2}$$

where $\Re$ is the universal gas constant that has a value of 8314.3 J kg^{-1} $mole^{-1}$ K^{-1}, m is the molar mass, and R is the gas constant for a particular gas. The universal gas constant $\Re$ is defined in terms of Boltzmann's constant k (1.3807×10^{-23} J K^{-1}) as

$$\Re = k N_A \tag{A.3}$$

where N_A is Avogadro's number (i.e., 6.0220×10^{23} $mole^{-1}$), the number of atoms needed such that the number of grams of a substance equals the atomic mass of the substance.

Another assumption is also adopted in the study of compressible fluid flow. That is, the specific heats at constant pressure and constant volume, c_p and c_v, are both constants. In this case, the gas is calorically perfect. The specific heat is the amount of heat per unit mass required to raise the temperature by one degree Celsius. The ratio of the two specific heats is

$$\gamma = c_p / c_v \tag{A.4}$$

It should also be recalled that:

$$R = c_p - c_v \tag{A.5}$$

While a calorically perfect gas has specific heats that are constant, a thermally perfect gas has specific heats that depend only on temperature and are thus nor necessarily constant. In addition, the gravitational, magnetic and electrical effects on the flow field are negligible. This assumption is quite justified for neutral gas flows [38].

The compressibility effects become important in a gas flow when the velocity in the flow is high. The ratio of the gas velocity to the speed of sound in the gas determines when compressibility is important. This ratio is termed the Mach number, M, i.e.,

$$M = V / a \tag{A.6}$$

where a is the speed of sound. If $M < 1$ the flow is said to be subsonic, whereas if $M > 1$ the flow is said to be supersonic. If the Mach number is near 1 and there are regions of both subsonic and supersonic flow, the flow is said to be transonic. If the Mach number is very much greater than 1, the flow is said to be hypersonic. Hypersonic flow is normally associated with flows in which $M > 5$. The speed of sound in a perfect gas is given by

$$a = \sqrt{\gamma R T} \tag{A.7}$$

The speed of sound in a gas depends, therefore, only on the absolute temperature of the gas.

A.4 Convergent-Divergent Nozzle

The nature of the flow that exists in the convergent-divergent nozzle can be explained by considering how the flow changes as the back pressure P_b is decreased while the upstream pressure P_0 is kept at one atmosphere. When P_b is nearly the same as P_0, the flow remains subsonic throughout and the mass flow rate increases with decreasing P_b/P_0. However, when the downstream pressure is decreased to a critical value, mass flow rate is unaffected by changes in P_b. Under these circumstances, when changes in the downstream pressure cannot effect conditions upstream of the throat, and therefore have no effect on the mass flow rate through the nozzle, the nozzle is said to be "choked." In this case, a Mach number of 1 has been reached at the throat.

As the back pressure is reduced below the critical value, a region of supersonic flow develops just downstream of the throat. This region of supersonic flow is terminated by a normal shock wave. The shock wave increases the pressure and reduces the velocity to a subsonic value. The flow in the nozzle under these circumstances is as shown in Figure A. 2. In real flows, if the nozzle of relatively small size and the boundary layer consequently relatively thick, a complex wave system can actually occur near the end of the supersonic flow region as a result of the interaction of the shock wave with the boundary layer. However, even in such cases, the characteristics of the flow can often be adequately modeled by assuming a normal shock wave. As the back pressure is further reduced, the extent of the supersonic flow region increases, the shock wave moving further down the divergent portion of the nozzle until outside the nozzle [38].

Consider a gas flow through the converging-diverging nozzle as shown in Figure A.1. The governing equations include the continuity equation (obtained by applying the principle of conservation of mass to the flow through the nozzle) as shown in Equation (A.1) and the energy equation (assuming that the flow is adiabatic, i.e., if there is no heat transfer to or from the flow):

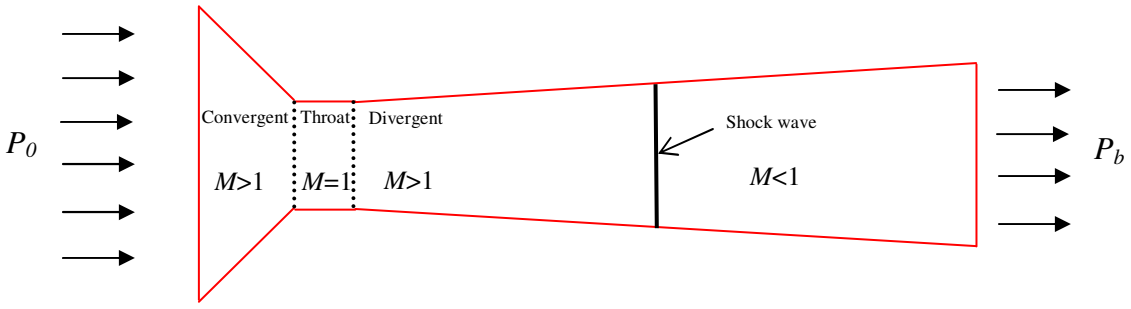

Figure A.2: Flow in a convergent-divergent nozzle (adapted from [38]).

$$C_p T_2 + \frac{V_2^2}{2} = C_p T_1 + \frac{V_1^2}{2} \tag{A.8}$$

Substituting (A.4), (A.5) and (A.7) into (A.8) yields:

$$V_2^2 + \frac{2}{\gamma - 1} a_2^2 = \frac{2}{\gamma - 1} a_1^2 \tag{A.9}$$

Using (A.6) and (A.9), the energy equation gives:

$$(\frac{a_2}{a_1})^2 = [1 + (\frac{\gamma - 1}{2}) M^2]^{-1} \tag{A.10}$$

In isentropic flow, the momentum equation (obtained by applying the principle of conservation of momentum to the flow through the nozzle) leads to the same results as the energy equation [38]. In addition to the above two equations, the isentropic relation (as discussed in Section 2.2.1) apply at all points, that is

$$\frac{P_2}{P_1} = (\frac{\rho_2}{\rho_1})^{\gamma} \tag{A.11}$$

Using (A.10) and (A.11) gives

$$(\frac{\rho_2}{\rho_1})^2 = [1 + (\frac{\gamma - 1}{2}) M^2]^{-\frac{1}{\gamma - 1}} \tag{A.12}$$

Considering (A.10) and (A.12) and the mass flow rate

$$\dot{m} = \rho V A \tag{A.13}$$

it follows that:

$$\frac{\dot{m}}{A} = \frac{\rho_1 a_1 M}{[1 + (\frac{\gamma - 1}{2}) M^2]^{\frac{\gamma + 1}{2(\gamma - 1)}}} \tag{A.14}$$

Applying this equation between the throat and the exit of the nozzle and assuming M at the throat is 1, M at the exit is then given by:

$$\frac{A_2}{A_1} = \frac{1}{M}\{(\frac{2}{\gamma+1})[1+(\frac{\gamma-1}{2})M^2]\}^{\frac{\gamma+1}{2(\gamma+1)}} \quad \text{(A.15)}$$

So, when the nozzle has a uniform depth *d*, (A.15) yields

$$\frac{D_2}{D_1} = \frac{1}{M}\{(\frac{2}{\gamma+1})[1+(\frac{\gamma-1}{2})M^2]\}^{\frac{\gamma+1}{2(\gamma+1)}} \quad \text{(A.16)}$$

This is Equation (2.1), defining the relationship between the expansion ratio D_2/D_1 of the converging-diverging nozzle and the Mach number M at the exit of the nozzle.

A.5 Summary

This appendix has presented the fundamentals of compressible fluid flow. First, the compressibility of a fluid was described with the interactions between the gas velocity, pressure, density and temperature. Next, fundamental principles and aspects of compressible flows such as the continuity equation, Newton's second law of motion, and the first law of thermodynamics were briefly discussed. Finally, gas flows in converging-diverging nozzles were presented.

APPENDIX B

EQUILIBRIUM SEPARATION NOZZLE FLOW

B.1 Introduction

In this appendix, an analytical model for predicting separation factors at thermal equilibrium is presented on the basis of the theoretical model developed in [24] for isotope separation. This model can be used to predict the relationship between the separation factor and the Mach number of the flow. It should be noted that this first-order model does not taken into account the non-equilibrium effects in the separation nozzle flows caused by the limited flow time of the mixture in the centrifugal field, and the spatial change of the centrifugal forces.

B.2 Equilibrium Separation Process

In the separation nozzle, a mass element of the process gas mixture passes through a centrifugal field of a complicated spatial structure within a short period of time. Because of the limited flow time of the mixture in the centrifugal field and the spatial change of the centrifugal forces, no equilibrium distribution of the components of the mixture can be established at which the diffusion streams caused by pressure and concentration gradients would fully compensate each other at each point. Nevertheless, some fundamental aspects of the separation process can be described by the limit case of equilibrium separation such as the distribution of molecular species in a steady-state cylindrical flow [24]. For simplification, an enclosed gas volume (e.g., a mixture of SF_6

and N_2) is assumed to circulate in a cylindrical flow at a constant angular velocity ω, it is well known that for each component i of the mixture a partial pressure p_i is

$$p_i(r) = p_i(0)\exp[M_i\omega^2 r^2/(2kT)] \tag{B.1}$$

where r is the radial coordinate, M_i is the mass of the molecule, k is Boltzmann's constant, and T is the absolute temperature. The quotient of the molar fraction ratios $N/(1-N)$, in the center $r=0$, and at the periphery $r=r_0$ of the cylindrical flow, which follows from the partial pressures, is identical with the equilibrium separation factor A^* of a gas centrifuge :

$$A^* = \frac{N_a(0)(1-N_a(r_0))}{(1-N_a(0))N_a(r_0)} = \exp[(M_h - M_a)\omega^2 r_0^2/(2kT)] \tag{B.2}$$

where N_a and $N_h = 1-N_a$ are the molar fractions of the auxiliary gas (N_2) and heavy gas (SF_6), respectively. M_a and M_h are the respective molecular masses; and ωr_0 is the peripheral velocity of the cylindrical flow. In order to facilitate the derivation, the flow parameter of speed ratio S_i is introduced below:

$$S_i = v/c_i = \omega r/(2kT/M_i)^{1/2} \tag{B.3}$$

which is the ratio between the flow velocity v and the most probable thermal velocity c_i of the component i of the mixture. Therefore, the equilibrium separation factor is derived to be

$$A^* = \exp[(M_h - M_a)S_a^2(r_0)/M_a] \tag{B.4}$$

At thermodynamic equilibrium, the peripheral Mach number of the mixture Ma_m, which characterizes the flow behavior of the mixture, is related to S_a by the relationship below

$$S_a^2 = \frac{\gamma}{2}\frac{M_a}{M_m}Ma_m^2 = \frac{\gamma}{2}\frac{M_a}{N_h M_h + (1-N_h)M_a}Ma_m^2 \tag{B.5}$$

where γ is the ratio of specific heats of the mixture, and M_m is the average molecular mass of the mixture [24]. Substituting equation (B.5) into equation (B.4) gives

$$A^* = \exp[(M_h - M_a)(\frac{\gamma}{2})(\frac{Ma_m^2}{N_h M_h + (1-N_h)M_a})] \tag{B.6}$$

Figure B.1 shows the elementary effect of the separation process (i.e., A*-1) for the model case of a cylindrical flow with constant angular velocity as a function of the SF_6 molar fraction N_h for various Mach numbers Ma_m of an N_2/SF_6 mixture. The increase in the relative difference A*-1 is obviously due to the fact that the SF_6 speed ratio increases correspondingly with a reduction in mean molecular weight of the mixture at a given Mach number Ma_m of the mixture.

B.3 Equilibrium Bifractional Splitting

For a simplified cylindrical flow with concentric stream lines which is split into two partial streams at a point r, the partial cut θ_i of the mixture component i can be calculated directly by radial integration over the flux profile [24]:

$$\theta_i(r) = \int_0^r j_i(r)dr \;/\; \int_0^{r_0} j_i(r)dr \tag{B.7}$$

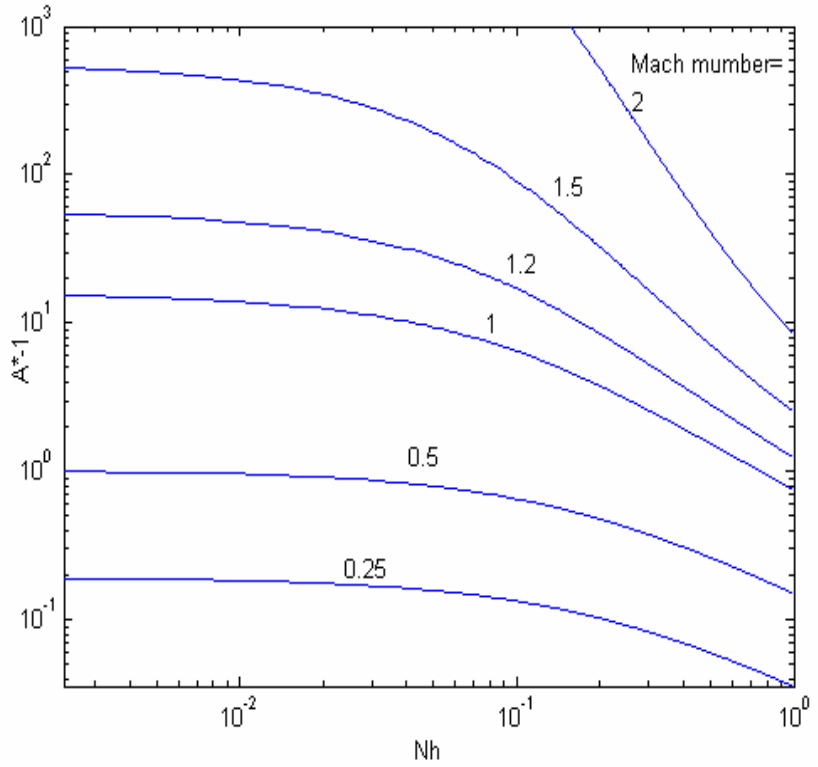

Figure B.1: Influence of the peripheral Mach number Ma_m (r_0) and the SF_6 molar fraction N_h (r_0) upon the elementary effect of the mixture separation (A*-1) for an isothermal cylindrical flow of N_2/SF_6 mixture.

It is known that for a cylindrical flow in a state of diffusion equilibrium (i.e., with constant angular velocity ω and spatially constant temperature)

$$p_i = \nu_i kT \tag{B.8}$$

where ν_i is the number density. With (B.1) and (B.8) the radial development of the flux j_i of the component i is derived as:

$$j_i(r) = wr\nu_i(0)\exp[M_i\omega^2 r^2/(2kT)] \tag{B.9}$$

where M_i is the molecular mass. Substituting (B.9) and (B.5) into (B.7) yields (B.10) or (3.2) mentioned in Section 3.2.1:

$$\theta_i(r) = \frac{\exp[(r/r_0)^2 \frac{\gamma}{2} \frac{M_i}{\overline{M}} Ma_m] - 1}{\exp[\frac{\gamma}{2} \frac{M_i}{\overline{M}} Ma_m] - 1} \tag{B.10}$$

Using (B.10) and (3.1) defined in Section 3.2, the separation factor can be calculated for different operating conditions.

B.4 Summary

In this appendix, an analytical model was derived to quantitatively describe the equilibrium separation processes in the separation nozzles. The influence of the molar fraction of the component and Mach number of the flow on the separation efficiency was discussed. Finally, an analytical equation for the separation factor was derived for the case of equilibrium bifractional splitting.

APPENDIX C

AUTOMATED PRESSURE MEASUREMENT SETUP

C.1 Introduction

In this appendix, an automated pressure measurement setup is presented. In this setup, LabVIEW programming and data collection on a computer provides real-time monitoring of the different manometers utilized in the gas separation experimental setup as discussed in Section 5.2. The bulk of this work was conducted by Mr. Yiu Au through his senior project studies.

C.2 Computer Setup

The MKS PDR-5D power supply/readout used in the gas separation experiments powers and reads up to 5 manometers for measurement. Its front panel contains a 4-digit display. The user needs to switch between different channels using the knob to read different channels by hand, thus channels cannot be read simultaneously or continuously. A computer interface with the power supply/readout will allow for continuous and simultaneous measurement automatically through an on-board interface device.

The power supply/readout includes on the back panel a 37-pin BCD (i.e., binary coded decimal) output. This output is included with an external digital display for displaying simultaneously up to 3 channels of input. Although the BCD output provides already digitalized signal, sending the signal directly to the computer is difficult due to non-standardized port (i.e. the pins are not standard to input to a 25-pin parallel port), thus extra specialty hardware is required to connect the port to the computer. Plus,

converting BCD to ordinary number requires complex programming. Since the power supply also has 5 analog DC signal outputs for each manometer, another approach is to digitize the signal from the analog output to the PC. The advantage of this method is that the signal can be more easily imported to LabVIEW for data gathering and processing with LabVIEW specific equipment, the extra hardware required by BCD output.

The analog DC signal outputs of the power supply/readout outputs a signal from 0V to +10V, proportional to the range of the manometer, which is either from 0 to 1000 Torr or 0 to 10,000 Torr. Since the digital display on the power supply/readout provides 4 digit of accuracy, with the last digit being uncertain according to the manual, the analog outputs would need 1mV of precision to utilize the full range of the power supply/readout. Since the manometers are relatively slow mechanical devices, any sampling rate faster than that on the order of seconds should be fine for this application.

Given the requirements, the NI-PCI6034E data acquisition (DAQ) device card was found to be the optimal solution that would be able to interface the power supply/readout to the computer. The DAQ card samples at maximum 200k samples/s and provides 16-bit of accuracy. However, the range of data input is limited to certain ranges.

Since the input of the power supply/readout is from 0V to +10V, the input range will have to be the largest input range for the DAQ card at -10V to +10V at a precision of 305.2μV. This precision is still enough to read the 4-digit power supply/readout correctly. The DAQ card can also support up to 16 inputs (using non-differential input channels with a common ground, or 8 differential signals with individual grounds). The power supply/readout only requires up to 5 input channels. Thus, in the future, there is room for

expansion to read output signals from the voltmeters measuring the outputs of the gas flow of the flowmeters, thus automating the entire measurement process.

Figure C.1 shows the block diagram for the NI-PCI6034E data acquisition device card [83]. The card includes 8 digital input and output channels. Automatic valves in controlling the flow of different input holes of the device could be set up and controlled by the computer through a digital signal output. Thus, the experimental environment could be automated in the future as well with simple addition to the current experimental setup.

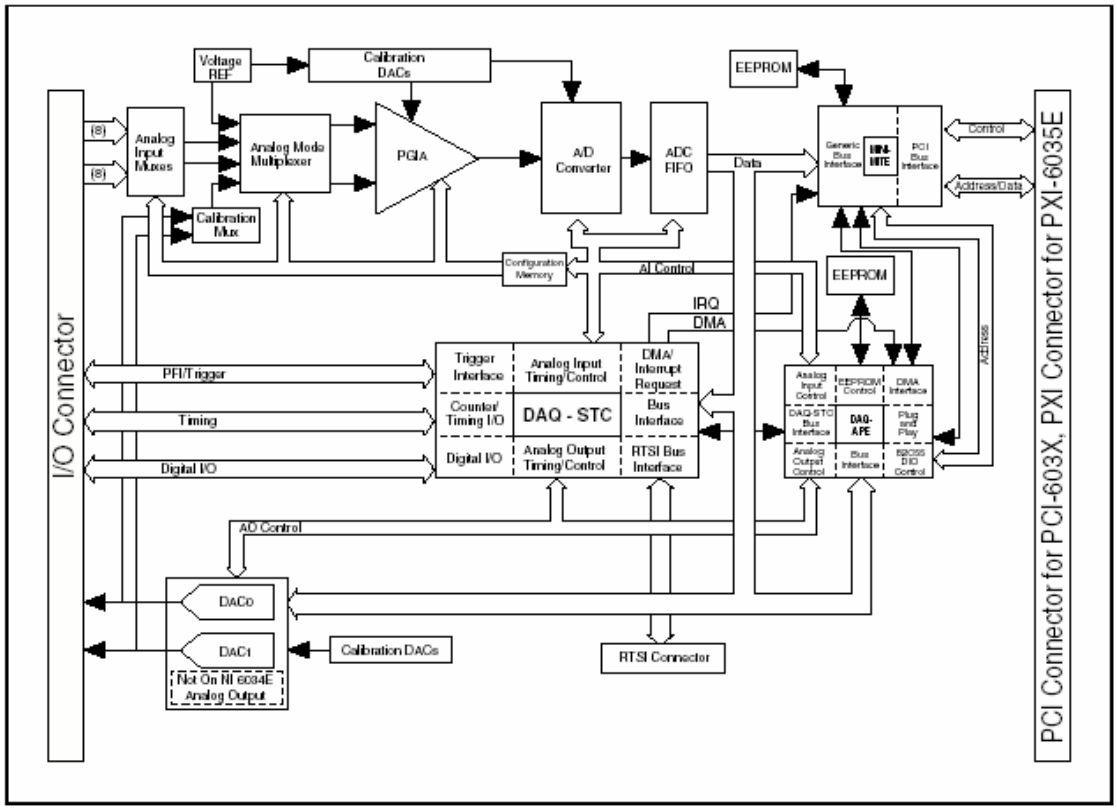

Figure C.1: Block diagram for the NI-PCI6034E data acquisition device card [83].

The NI-PCI6034E DAQ card is a 68-pin device, as shown in Figure C.2, that has a special ribbon cable and adapter to collect input signal and send output signal [83]. Since the power supply/readout will only require the use of up to 5 input channels and the ground input, the ribbon cable would not be necessary; it would be more cost effective to make a 6-wire cable out of shielded pre-cut cable soldered to special connectors to connect with pins on the DAQ card that are spaced at small distances apart and are required to be electrically isolated. Insulating Teflon tapes are wrapped to the connectors to ensure electrical isolation and safety from floating voltages.

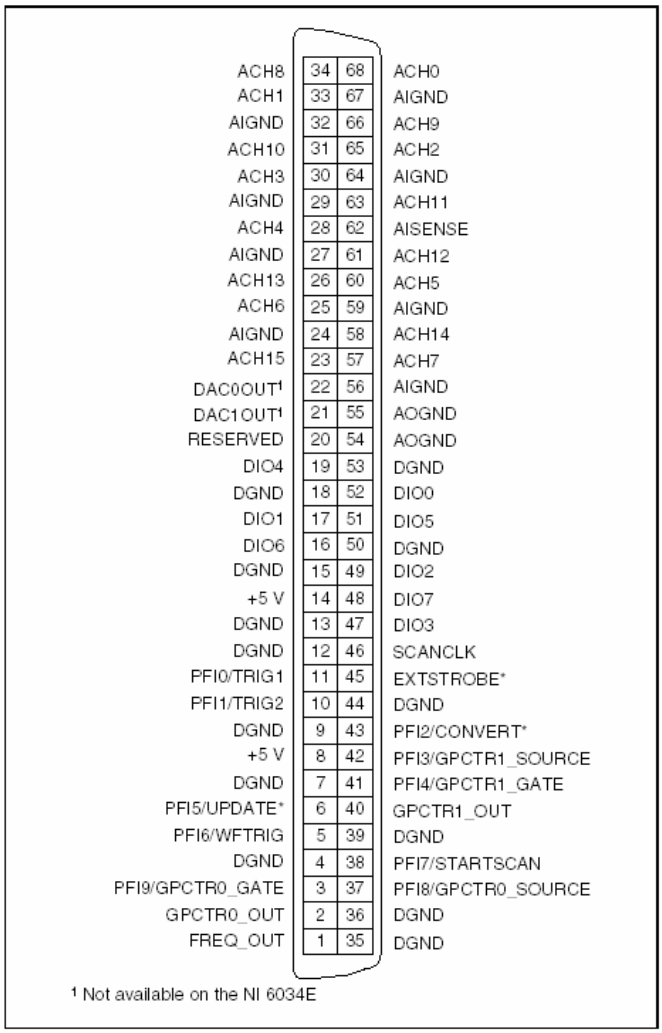

Figure C.2: Pin assignment on the NI-PCI6034E DAQ card [83].

The power supply/readout would use analog input channel 0 to 4 (ACH#) corresponding to manometers 1 to 5, respectively. Manometers 1 to 4 are the 1000 Torr ranged instruments, while manometer 5 is a 10000 Torr ranged instrument for measuring the inlet pressure. Color-coded wires from the cable are used in the connection from the power supply/readout to the DAQ card, and the black wire connects the ground of the power supply/readout to the analog ground (AIGND) of the DAQ card to use for non-differential input.

In the software *Measurement and Automation* provided by the DAQ card, each channel can be set to its smallest and largest input limits to ensure that the best precision range be used. Another function of the software is to specify the real range and unit of the input represented by voltages from the input proportionally. The manometer's input in Torr can be specified to automatically display in LabVIEW discussed below.

C.3 LabVIEW

LabVIEW is initially set as a viewer for the data gathered from the DAQ. In the "DAQ Solutions" from the main menu, the default DAQ measurement programs can be chosen for data gatherings [83]. The setup requires a "Voltage and Current Measurement" from the "Common Solution Gallery", and "Continuous Voltage Measurement" is needed since the pressure change over time needs to be recorded. Modifications were made to the LabVIEW program including changing the range of the graph to reflect the range of the manometers, especially for M5 since it's up to 10,000 Torr. Because virtual channels created in the *Measurement and Automation* can be

referenced directly in LabVIEW, M1 to M5 can be inputted directly into the program and the measurement range for the manometer is correctly displayed, as shown in Figure C.3.

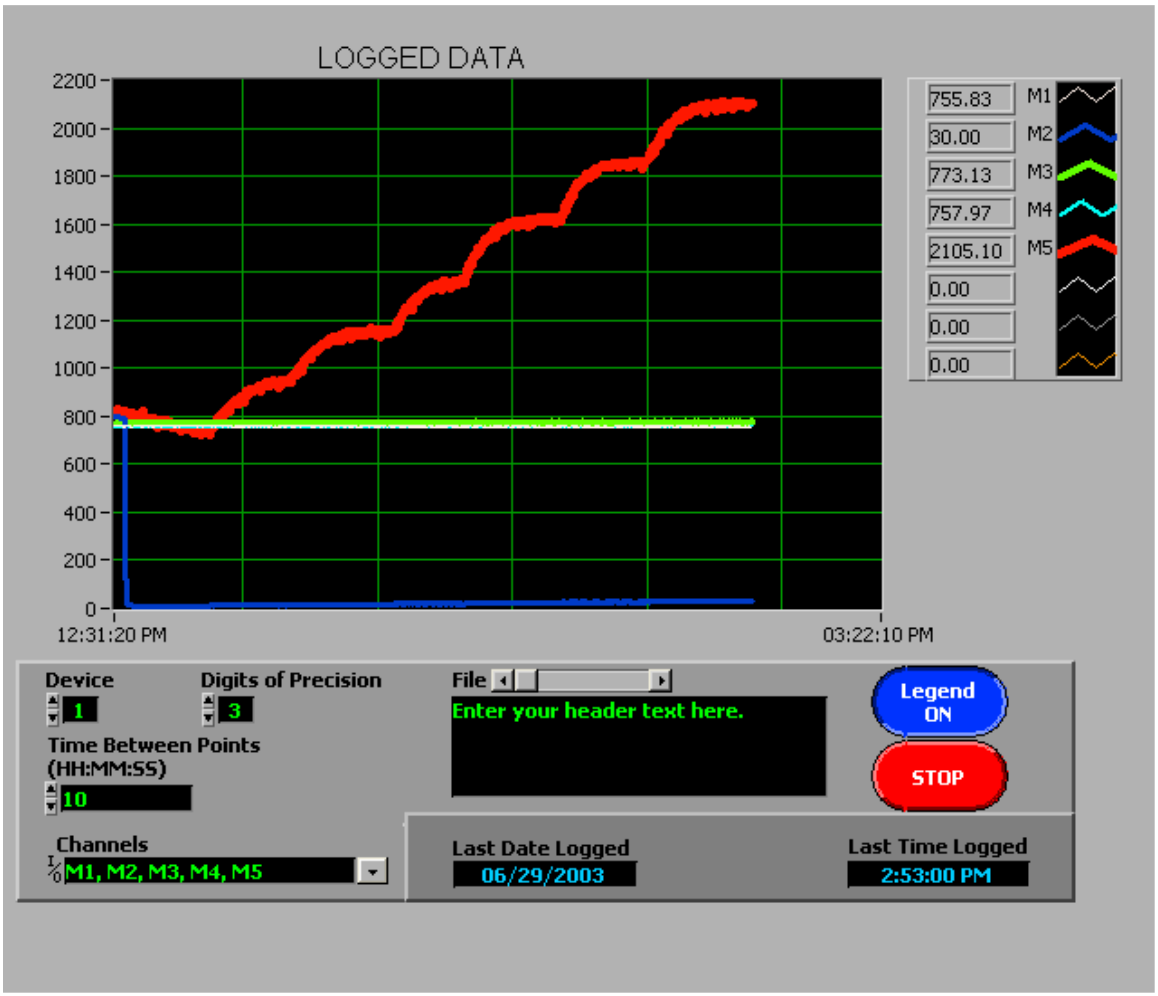

Figure C.3: The data logger after modifying the data viewer program.

LabVIEW has limited data plotting and printing capabilities for further data analysis and recording. Therefore, an important functionality of the data gathering program is to be able to log the manometer data and process the data gathered over time as a batch. One way to implement this function is to do the calculations to the measurements in LabVIEW continuous as they are being read. Although LabVIEW is

capable of doing the calculations through programming the VI (virtual instrument), it may be better to log the outputs and do the calculations later. The reason for this setup is that while LabVIEW is running, every point gathered is plotted to the graph. Since the nature of the device and of the experiment requires a relatively long time for stabilization (from tens of minutes to hours), the points from the time the experiment starts till it has completely stabilized should be plotted to the screen so that during the experiment, mistakes can be checked and changed quickly, and quick judgments and mental calculations can be made to the data. All points would use up 16-bit since that's the precision of the DAQ and it would be important to maintain that precision so we can measure the full range of the power supply/readout. Thus theoretically, memory needed for data gathering of all 5 channels will only be 10 bytes per second, with data values measured once every second. This corresponds to around 36 kilobytes per hour of measurement, which is not much.

However, one observed behavior of LabVIEW is that it seems to require 100 times the memory it theoretically needs to gather the data and to output them to the graph on the display. This behavior is directly linked to the number of points LabVIEW displays since reducing or increasing the number of points it is asked to display roughly affects the memory used by LabVIEW proportionally. One explanation for this behavior might be that LabVIEW, besides representing the data as the required number of precision, also stores extra precision internally (perhaps to 32-bit or 64-bit numbers). The extra bits for padding would help in internal calculations that LabVIEW does to avoid loss of precision. Also, *Windows* might need to duplicate the data to a separate memory

pool in order to display them. External data storage and calculation were carried out to compensate for the behavior.

The logged data can be easily imported to other applications (e.g., *Excel*) for calculations. Specifically, in *Excel*, the logged data can be imported using the tool that parses tab delimited file formats to their respective column in the spreadsheet. Data can then be plotted or used in the isentropic model as described in Section 2.2.1, which was already set up in an *Excel* spreadsheet.

C.4 Summary

In this appendix, the automated pressure measurement setup using DAQ and LabVIEW programming has been presented. The DAQ card was selected and color-coded wire interconnection was made in accordance with the specifications of the power supply/readout for the manometers. Modifications have been made to the built-in LabVIEW program to correctly display the measurements of the manometers used in the gas separation experiments. This automated measurement setup can also be easily tailored for other applications.

APPENDIX D

ELECTRONIC NOSE TECHNOLOGY

D.1 Introduction

Electronic noses are devices that functionally mimic the sense of olfaction to analyze gaseous mixtures and/or quantify the concentration of their constituents [84]. This technology is rapidly evolving, driven by the practical demand for objective analysis of odors as well as by the intellectual challenge of mimicking the mammalian sense of olfaction [85-87]. Electronic noses are generally composed of a sampling system, an array of chemical sensors, readout circuits, and data analysis software [88]. So far, electronic noses have already found two main application areas: food-quality control and environmental monitoring [84].

It is believed that humans and other mammals rely on a pattern generated from the response of many broadly tuned olfactory receptor sites, instead of employing lock-and-key type specificity to individual analytes in the broadly responsive portion of their olfactory systems [89]. Similarly, individual polymer types in an electronic nose are swollen by many chemically diverse analytes. Humans are thought to have ~1000 different olfactory genes that presumably encode for ~1000 olfactory receptor proteins. A major goal of developing an artificial nose is therefore to produce a highly diverse array of differentially responsive vapor detectors [79].

In the past years, numerous implementations of artificial noses have emerged, most of which are based on detecting a physical or chemical change in a polymer film upon exposure to a gaseous analyte [90]. The measured quantity in an individual detector

can be the frequency shift of a resonating crystal in a quartz crystal microbalance (QCM) [84] or a surface acoustic wave configuration (SAW) [92, 93] changes in the optical absorption or emission properties of a dye that has been impregnated into a polymer [94-96] or changes in the electrical resistance of a conductive polymer (CP) [97] or of a carbon black/polymer composite (CB/PC) film [98]. Any individual detector does not respond highly specifically toward an individual analyte, but the pattern of responses in an array of differentially responsive detectors can be used to identify, classify, and in some cases quantify, the analyte of interest [79]. In the following section, a specific electronic nose developed at Caltech is discussed.

D.2 Caltech Electronic Nose

The so-called Caltech electronic nose is based on the chemically sensitive conducting polymer films. The underlying principle is simple: when a polymer film is exposed to a gaseous vapor, some of the vapor enters the film and causes the film to swell (Figure D.1). In the electronic nose, this swelling is probed electrically because the sensor films each consist of a composite that contains regions of a conductor that have been dispersed into the swellable organic insulator. The vapor-induced film swelling produces an increase in the electrical resistance of the film because the swelling decreases the number of connected pathways of the conducting component of the composite material [99].

The detector films can be formed from conducting polymer composites, in which the electronically conductive phase is a conducting organic polymer and the insulating phase is an organic polymer, or from polymer-conductor composites in which the

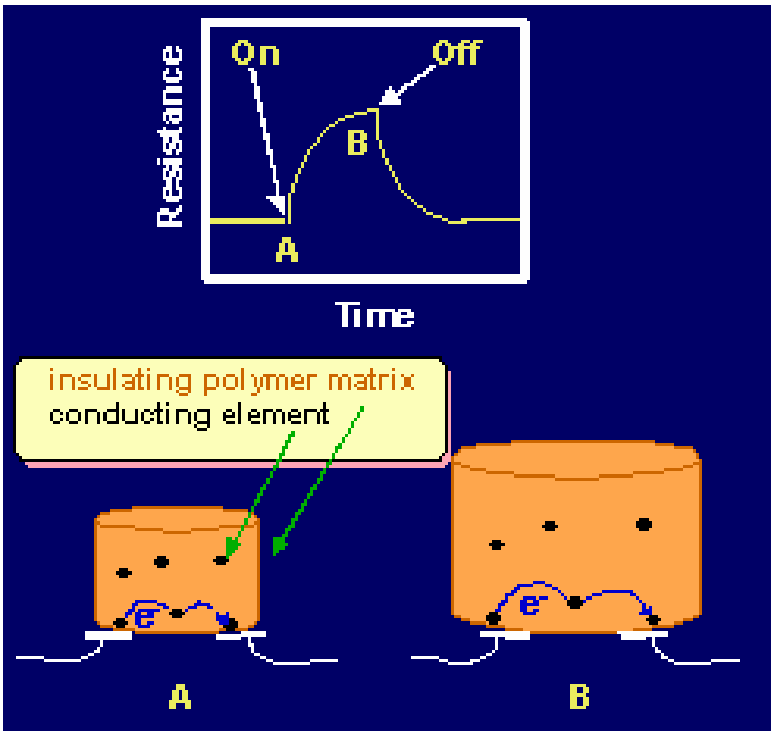

Figure D.1: Swelling occurs as vapor molecules enter the polymer. An increase in the electrical resistance of the film is caused by the vapor-induced film swelling (adapted from [99]).

conductive phase is an inorganic conductor such as carbon black, Au, Ag, etc and the insulating phase is a swellable organic material. The electrical resistance of the device is then read using simple, low power electronics [99].

Specifically, in the implementation of Caltech electronic noses, arrays of carbon black/polymer composites comprised of 10-20 compositionally different detectors have been shown to differentiate efficiently between many organic vapors when assessed under controlled conditions in the laboratory [79]. Distinctive patterns have allowed pairwise differentiation between species that differ in structure and polarity as well as between members of homologous series of, for example, alcohols or alkanes [100].

Furthermore, as shown in Figure D.2 [99], the response of the carbon black/polymer composite sensors is a linear function of analyte concentration [98-101]. An array of sensors, containing different polymers, yields a distinct fingerprint for each vapor because the swelling properties over the entire array are different for different vapors. The pattern of resistance changes on the array is a diagnostic of the vapor, while the amplitude of the patterns indicates the concentration of the vapor. A database, consisting of response patterns for different analytes, has been built as a reference source [80, 81].

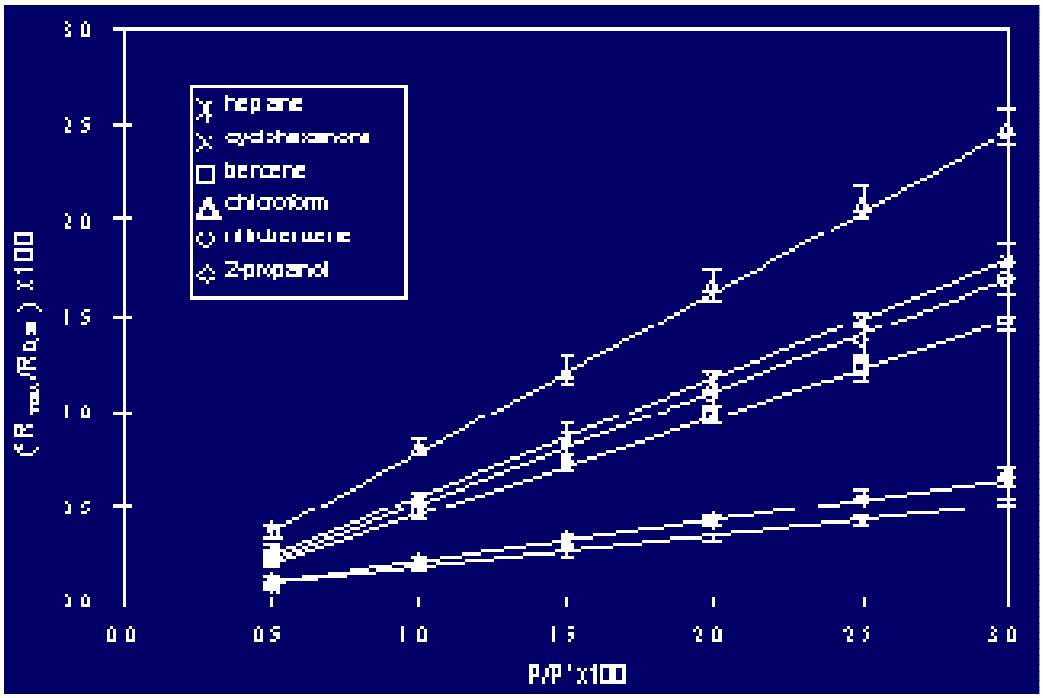

Figure D.2: A linear response of an individual sensor signal as a function of concentration is observed for a variety of analytes (adapted from [92]).

D.3 Comments and Summary

In this appendix, the basics of electronic nose technology have been reviewed with emphasis on the artificial nose developed at Caltech. The reader can refer to the cited references for more details regarding this technology. The next-generation electronic noses are envisioned to be hand-held devices for trace detection of pollutants and/or warfare agents. Despite the challenges facing the field (e.g., reliability of sensing materials and complex algorithms for signal discrimination [102]), the opportunities for developing on-chip biochemical detection systems are abundant in the light of the advances in nanotechnology and MEMS.

BIBLIOGRAPHY

[1] C.-M. Ho, "Fluidics-the link between micro and nano sciences and technologies," *in Proc. MEMS 2001*, pp. 375-384, Interlaken, Switzerland, Jan. 21-25, 2001.

[2] A. Folch, A. Ayon, O. Hurtado, and M. A. Schmidt, "Molding of deep polydimethylsiloxane microstructures for microfluidics and biological applications," *Transactions of the ASME: Journal of Biomechanical Engineering*, vol. 121, pp. 28-34, 1999.

[3] A. Manz, N. Graber, and H. M. Widmer, "Miniaturized total chemical analysis systems: a novel concept for chemical sensing," *Sensors and Actuators B: Chemical*, vol. B1, pp. 244-248, 1990.

[4] D. J. Harrison, A. Manz, Z. Fan, H. Luedi, and H. N. Widmer, "Capillary electrophoresis and sample injection systems integrated on a planar glass chip," *Analytical Chemistry*, vol. 64, pp. 1926-1932, 1992.

[5] V. Srinivasan and J. W. Weidner, "An electrochemical route for making porous nickel oxide electrochemical capacitors," *Journal of the Electrochemical Society*, vol. 144, pp. 210-213, 1997.

[6] P. C. Simpson, A. T. Woolley, and R. A. Mathies, "Microfabrication technology for the production of capillary array electrophoresis chips," *Biomedical Microdevices*, vol. 1, pp. 7-25, 1998.

[7] J. P. Brody, Y. Han, R. H. Austin, and M. Bitensky, "Deformation and flow of red blood cells in a synthetic lattice: evidence for an active cytoskeleton," *Biophysical Journal*, vol. 68, pp. 2224-2232, 1995.

[8] C.-J. Lu, J. Whiting, R. D. Sacks, and E. T. Zellers, "Portable gas chromatography with tunable retention and sensor array detection for determination of complex vapor mixture," *Analytical Chemistry*, vol. 75, pp. 1400-1409, 2003.

[9] S. Taylor, R. F. Tindall, and R. R. A. Syms, "Silicon based quadrupole mass spectrometry using microelectromechanical systems," *Journal of Vacuum Science and Technology B*, vol. 19, pp. 557-562, 2001.

[10] C. B. Freidhoff, R. M. Young, S. Sriram, T. T. Braggins, T. W. O'Keefe, J. D. Adam, H. C. Nathanson, R. R. A. Syms, T. J. Tate, M. M. Ahmad, S. Taylor, and J. Tunstall, "Chemical sensing using nonoptical microelectromechanical systems," *Journal of Vacuum Science and Technology A*, vol. 17, pp. 2300-2307, 1999.

[11] J. W. Grate and M. H. Abraham, "Solubility interactions and the design of chemically selective sorbent coatings for chemical sensors and arrays," *Sensors and Actuators B: Chemical*, vol. B3, pp. 85-111, 1991.

[12] M. S. Nieuwenhuizen and A. W. Barendsz, "Processes involved at the chemical interface of a SAW chemosensor," *Sensors and Actuators*, vol. 11, pp. 45-62, 1987.

[13] G. G. Guilbault, Y. Tomita, and E. S. Kolesar, Jr, "A coated piezoelectric crystal to detect organophosphorous compounds and pesticides," *Sensors and Actuators*, vol. 2, pp. 43-57, 1981.

[14] A. Mohacsi, Z. Bozoki, and R. Niessner, "Direct diffusion sampling-based photoacoustic cell for in situ and on-line monitoring of benzene and toluene concentrations in water," *Sensors and Actuators B: Chemical*, vol. B79, pp. 127-131, 2001.

[15] "http://www.chem.vt.edu/chemed/sep/gc."

[16] E. T. Zellers, W. H. Steinecker, G. R. Lambertus, M. Agah, C.-J. Lu, H. K. L. Chan, J. A. Potkay, M. C. Oborny, J. M. Nichols, A. Astle, H. S. Kim, M. P. Rowe, J. Kim, L. W. d. Silva, J. Zheng, J. J. Whiting, R. D. Sacks, S. W. Pang, M. Kaviany, P. L. Bergstrom, A. J. Matzger, Ç. Kurdak, L. P. Bernal, K. Najafi, and K. D. Wise, "A versatile MEMS gas chromatograph for determinations of environmental vapor mixtures," *in Proc. Solid-State Sensors, Actuators and Microsystems Workshop*, pp. 61-66, Hilton Head Island, South Carolina, June 6-10, 2004, 2004.

[17] C.-Y. Peng and S. Batterman, "Performance evaluation of a sorbent tube sampling method using short path thermal desorption for volatile organic compounds," *Journal of Environmental Monitoring*, vol. 2, pp. 313-324, 2000.

[18] W.-C. Tian, S. W. Pang, C.-J. Lu, and E. T. Zellers, "Microfabricated preconcentrator-focuser for a microscale gas chromatograph," *Journal of Microelectromechanical Systems*, vol. 12, pp. 264-272, 2003.

[19] W.-C. Tian, H. K. L. Chan, S. W. Pang, C.-J. Lu, and E. T. Zellers, "Multiple-stage microfabricated preconcentrator-focuser for micro gas chromatography system," *Journal of Microelectromechanical Systems*, vol. 14, pp. 498-507, 2005.

[20] P. Lubicki, J. D. Cross, S. Jayaram, J. S. Zhao, and O. Ward, "Removal of nitrobenzene and volatile organic compounds using electron radiation," presented at 1997 IEEE Annual Report - Conference on Electrical Insulation and Dielectric Phenomena, Minneapolis, October 19-22, 1997.

[21] C. Schaper and A. Tay, "Electron beam patterning on permeable polymer membranes for nanolithography and microfluidic applications," presented at Thirteenth Biennial University/Government/Industry Microelectronics Symposium, 1999.

[22] E. W. Becker, W. Ehrfeld, D. Münchmeyer, H. Betz, A. Heuberger, S. Pongratz, W. Glashauser, H. J. Michel, and R. v. Siemens, "Production of separation-nozzle systems for uranium enrichment by a combination of x-ray lithography and galvanoplastics," *Naturwissenschaften*, vol. 69, pp. 520-523, 1982.

[23] E. W. Becker, W. Bier, P. Bley, W. Ehrfeld, K. Schubert, and D. Seidel, "Development and technical implementation of the separation nozzle process for enrichment of uranium-235," *Am. Inst. Chem. Eng., Sym. Ser.*, vol. 78, 1982.

[24] W. Ehrfeld, *Elements of Flow and Diffusion Processes in Separation Nozzles*. Berlin Heidelberg: Springer-Verlag, 1983.

[25] E. W. Becker, "Development of the separation nozzle process for enrichment of uranium," *German Chemical Engineering*, vol. 9, pp. 204-208, 1986.

[26] E. W. Becker, K. Bier, and W. Bier, "Trenndusenverfahren mit leichtem Zusatzgas," *Z. Naturforsh*, vol. A17, pp. 778-785, 1962.

[27] E. W. Becker, K. Bier, W. Bier, and R. Schutte, "Trenndusenentmischung der Uranisotope bei Verwendung leichter Zusatzgase," *Z. Naturforsch*, vol. A18, pp. 246-250, 1963.

[28] E. W. Becker, K. Bier, W. Bier, R. Schutte, and D. Seidel, "Separation of the isotopes of uranium by the separation nozzle process," *Angew. Chem. Int. Edit. Engl.*, vol. 6, pp. 507-518, 1967.
[29] E. W. Becker, W. Bier, and R. Schutte, "Principles and econimic aspects of the separation nozzle process," *KFK 853, Karlsruhe*, 1968.
[30] H. Lorenz, M. Despont, N. Fahrni, N. LaBianca, P. Renaud, and P. Vettiger, "SU-8: a low-cost negative resist for MEMS," *Journal of Micromechanics and Microengineering*, vol. 7, 1997.
[31] M. Despont, H. Lorenz, N. Fahrni, J. Brugger, P. Renaud, and P. Vettiger, "High aspect ratio ultrathick, negative-tone near-UV photoresist for MEMS applications," *in Proc. MEMS 1997*, pp. 518-522, Nagora, Japan, 1997.
[32] H. Lorenz, M. Despont, N. Fahrni, J. Brugger, P. Vettiger, and P. Renaud, "High-aspect-ratio, ultrathick, negative-tone near-UV photoresist and its applications for MEMS," *Sensors and Actuators A: Physical*, vol. 64, pp. 33-39, 1998.
[33] R. J. Jackman, T. M. Floyd, R. Ghodssi, M. A. Schmidt, and K. F. Jensen, "Microfluidic systems with on-line UV detection fabricated in photodefinable epoxy," *Journal of Micromechanics and Microengineering*, vol. 11, pp. 263-269, 2001.
[34] P.-A. Clerc, L. Dellmann, F. Gretillat, M.-A. Gretillat, P-F. Indermuhle, S. Jeanneret, P. Luginbuhl, C. Marxer, T. L. Pfeffer, G.-A. Racine, S. Roth, U. Staufer, C. Stebler, P. Thiebaud, and N. F. d. Rooij, "Advanced deep reactive ion etching: a versatile tool for microelectromechanical systems," *Journal of Micromechanics and Microengineering*, vol. 8, pp. 272-278, 1998.
[35] D. E. Rother, "Electron-beam studies of viscous flow in supersonic nozzles," *J. AIAA*, vol. 9, pp. 804-811, 1971.
[36] S. P. Grisnik, T. A. Smith, and L. E. Salz, "Experimental study of low Reynolds number nozzle," *AIAA Paper*, pp. 87-0092, 1987.
[37] R. L. Bayt and K. S. Breuer, "Viscous effects in supersonic MEMS-fabricated micronozzles," presented at 3rd ASME Microfluids Symposium, Anaheim, Califonia, 1998.
[38] P. H. Oosthuizen and W. E. Carscallen, *Compressible Fluid Flow*. New York: The McGraw-Hill, 1997.
[39] "ANSYS/FLOTRAN Manual," 2004.
[40] S. Li and R. Ghodssi, "Development of microfluidic devices for gas centrifuge separation," presented at AVS 49th International Symposium, Denver, CO, 2002.
[41] S. Li, C. B. Freidhoff, R. M. Young, and R. Ghodssi, "Fabrication of micronozzles using low temperature wafer-level bonding with SU-8," *Journal of Micromechanics and Microengineering*, vol. 13, pp. 732-738, 2003.
[42] L. J. Guérin, M. Bossel, M. Demierre, S. Calmes, and P. Renaud, "Simple and low cost fabrication of embedded microchannels by using a new thick-film photoplastic," presented at Transducers'97, Chicago, USA, 1997.
[43] W. P. Maszara, G. Goetz, A. Caviglia, and J. B. Mckitterick, "Bonding of silicon wafers for slicon-on-insulator," *J. Appl. Phys.*, vol. 64, pp. 4943-4950, 1988.
[44] Q.-Y. Tong and U. Gösele, *Semiconductor Wafer Bonding*. New York: Wiley, 1999.

[45] S. Li, C. B. Freidhoff, R. M. Young, and R. Ghodssi, "Fabrication, packaging and testing of micronozzles for gas sensing applications," presented at AVS 50th International Symposium, Baltimore, MD, 2003.
[46] F. J. Blanco, M. Agirregabiria, J. Garcia, J. Berganzo, M. Tijero, M. T. Arroyo, J. M. Ruano, I. Aramburu, and K. Mayora, "Novel three-dimensional embedded SU-8 microchannels fabricated using a lowtemperature full wafer adhesive bonding," *Journal of Micromechanics and Microengineering*, vol. 14, pp. 1047-1056, 2004.
[47] E. S. Lee, D. Howard, E. Liang, S. D. Collins, and R. L. Smith, "Removable tubing interconnects for glass-based micro-fluidic systems made using ECDM," *Journal of Micromechanics and Microengineering*, vol. 14, pp. 535–541, 2004.
[48] P. Abgrall, C. Lattes, V. Conédéra, X. Dollat, S. Colin, and A. M. Gué, "A novel fabrication method of flexible and monolithic 3D microfluidic structures using lamination of SU-8 films," *Journal of Micromechanics and Microengineering*, vol. 16, pp. 113-121, 2006.
[49] W. W. Y. Chow, K. F. Lei, G. Shi, W. J. Li, and Q. Huang, "Microfluidic channel fabrication by PDMS-interface bonding," *Smart Materials and Structures*, vol. 15, pp. 112-116, 2006.
[50] S. D. Senturia, *Microsystem Design*. Boston: Kluwer Academic Publishers, 2001.
[51] M. A. Schmidt, "Wafer-to-wafer bonding for microstructure formation," *Proc. of the IEEE*, vol. 86, pp. 1575-1585, 1998.
[52] A. U. Chatwani, M. Fiebig, N. K. Mitra, W. Schwan, P. Bley, W. Ehrfeld, and W. Fritz, "Tracer Monte Carlo simulation for an isotope separation nozzle," presented at *in Proc. 12th Int. Symp. Rarefied Gas Dynamics*, New York, 1981.
[53] A. U. Chatwani, M. Fiebig, N. K. Mitra, W. Ehrfeld, and W. Fritz, "Nonequilibrium effects and their modeling in separation nozzles," presented at *in Proc. 12th Int. Symp. Rarefied Gas Dynamics*, New York, 1981.
[54] M. Gad-el-Hak, "The fluid mechanics of microdevices-the Freeman scholar lecture," *Journal of Fluids Engineering*, vol. 121, pp. 5-33, 1999.
[55] J. C. Day, "Numerical simulation of a microfabricated gas preconcentrator for environmental monitoring," in *Aerospace Engineering*. College Park: University of Maryland, 2005.
[56] J. D. Anderson, *Modern Compressible Flow with Historical Perspective*. Boston: McGraw Hill, 1990.
[57] R. F. Probstein, *Physiconchemical Hydrodynamics: An Introduction*. New York: John Wiley & Sons, 1994.
[58] R. B. Bird, W. E. Stewart, and E. N. Lightfoot, *Transport Phenomena*. New York: John Wiley & Sons, 2002.
[59] R. Verfurth, *A Review of a Posteriori Error Estimation and Adaptive Mesh-Refinement Techniques*. Stuttgart: Teubner Verlag and J. Wiley, 1996.
[60] "FEMLAB Reference Manual." Burlington, MA, 2005.
[61] G. T. A. Kovacs, N. I. Maluf, and K. E. Petersen, "Bulk micromachining of silicon," *Proceedings of the IEEE*, vol. 86, pp. 1536-1551, 1998.
[62] M. J. Madou, *Fundamentals of Microfabrication: the Science of Miniaturization*: CRC Press LLC, 2002.

[63] A. A. Ayon, X. Zhang, and R. Khanna, "Ultra deep anisotropic silicon trenches using deep reactive ion etching (DRIE)," presented at Solid-State Sensor and Actuator Workshop, Hilton Head Island, SC, 2000.
[64] G. K. Fedder, S. Santhanam, M. L. Reed, S. C. Eagle, D. F. Guillou, M. S.-C. Lu, and L. R. Carley, "Laminated high-aspect-ratio microstructures in a conventional CMOS process," *Sensors and Actuators A: Physical*, vol. 57, pp. 103-110, 1996.
[65] R. L. Bayt and K. S. Breuer, "Viscous effects in supersonic MEMS-fabricated micronozzles," *in Proc. The 3rd ASME Microfluids Symposium, Anaheim, California*, 1998.
[66] M. A. Schmidt, "Wafer-to-wafer bonding for microstructure formation," *Proceedings of the IEEE*, vol. 86, pp. 1575-1585, 1998.
[67] F. Niklaus, P. Enoksson, E. Kälvesten, and G. Stemme, "Low-temperature full wafer adhesive bonding," *Journal of Micromechanics and Microengineering*, vol. 11, pp. 100-107, 2001.
[68] "Manual of Surface Technology Systems (STS) Deep Reactive Ion Etching System," 2003.
[69] S. Li, C. B. Freidhoff, R. M. Young, and R. Ghodssi, "Development of MEMS-based micronozzles for gas separation," presented at Materials Research Society (MRS) Spring Meeting, San Francisco, CA, 2004.
[70] "http://www.waters.com/WatersDivision/."
[71] "http://www.kimphys.com/new_products/new.htm."
[72] C. G. Herbert and R. A. W. Johnstone, *Mass Spectrometry Basics*. Boca Raton: CRC Press, 2002.
[73] "http://webbook.nist.gov/chemistry."
[74] W. Umrath, "Fundamentals of Vacuum Technology," in *Leybold Vacuum Products and Reference Book*. Cologne, 1998.
[75] S. Li, J. J. Park, J. C. Day, G. W. Rubloff, C. P. Cadou, and R. Ghodssi, "Development of a fast-response microfluidic gas concentrating device," presented at Eurosensors XIX, Barcelona, Spain, 2005.
[76] C. M. Waits, B. Morgan, M. J. Kastantin, and R. Ghodssi, "Microfabrication of 3D silicon MEMS structures using gray-scale lithography and deep reactive ion etching," *Sensors and Actuators A: Physical*, 2004.
[77] A. Modafe, N. Ghalichechian, B. Kleber, and R. Ghodssi, "Electrical characterization of benzocyclobutene polymers for electric micromachines," *IEEE Transactions on Device and Materials Reliability*, 2004.
[78] N. S. Lewis, "An electronic nose from array of polymer composite vapor sensors," presented at Materials Research Society (MRS) Spring Meeting, San Francisco, CA, 2004.
[79] A. J. Matzger, C. E. Lawrence, R. H. Grubbs, and N. S. Lewis, "Combinatorial approaches to the synthesis of vapor dectector arrays for an electronic nose," *Journal of Combinatorial Chemistry*, vol. 2, pp. 301-304, 2000.
[80] M. C. Lonergan, E. J. Severin, B. J. Doleman, S. A. Beaber, R. H. Grubbs, and N. S. Lewis, "Array-based sensing using chemically sensitive, carbon black-polymer resistors," *Chemistry of Materials*, vol. 8, pp. 2298-2312, 1996.

[81] G. A. Sotzing, S. M. Briglin, R. H. Grubbs, and N. S. Lewis, "Preparation and properties of vapor detector arrays formed from poly(3,4-ethylenedioxy)thiophene-poly(styrene sulfonate)/insulating polymer composites," *Analytical Chemistry*, vol. 72, pp. 3181-3190, 2000.
[82] A. H. Shapiro, *The Dynamics and Thermodynamics of Compressible Fluid Flow*, vol. 1. New York: The Ronald Press Company, 1953.
[83] "Guide to National Instruments Data Acquisition (DAQ)," 2003.
[84] M. Pardo and G. Sberveglieri, "Electronic olfactory systems based on metal oxide semiconductor sensor arrays," *Material Research Society (MRS) Bulletin*, vol. 29, pp. 703-708, 2004.
[85] T. A. Dickinson, J. White, J. S. Kauer, and D. R. Walt, "Current trends in 'artificial-nose' technology," *Trends Biotechnology*, vol. 16, pp. 250-258, 1998.
[86] P. N. Bartlett, J. M. Elliott, and J. W. Gardner, "Application of, and developments in, machine olfaction," *Ann. Chim.*, vol. 87, pp. 33-44, 1997.
[87] E. Schaller, J. O. Bosset, and F. Escher, "Electronic noses and their application to food," *Food Sci. Technol.-Lebensm.-Wiss. Technol.*, vol. 31, pp. 305-316, 1998.
[88] J. Gardner and P. Bartlett, *Electronic Noses*: Oxford University Press, 1999.
[89] B. Malnic, J. Hirono, T. Sato, and L. B. Buck, "Combinatorial receptor codes for odors," *Cell*, vol. 96, pp. 713-723, 1999.
[90] G. Harsányi, *Polymer Films in Sensor Applications: Technology, Materials, Devices and Their Characteristics*. Lancaster: Technomic Pub. Co., 1995.
[91] S. M. Chang, Y. Iwasaki, M. Suzuki, E. Tamiya, I. Karube, and H. Muramatsu, "Detection of odorants using an array of piezoelectric crystals and neural network pattern recognition," *Anal. Chim. Acta*, vol. 249, pp. 323-329, 1991.
[92] J. W. Grate, S. J. Martin, and R. M. White, "Acoustic wave microsensors (part II)," *Anal. Chem.*, vol. 65, pp. A987-A996, 1993.
[93] J. W. Grate, S. J. Martin, and R. M. White, "Acoustic wave microsensors (part I)," *Anal. Chem.*, vol. 65, pp. A940-A948, 1993.
[94] T. A. Dickinson, J. White, J. S. Kauer, and D. R. Walt, "A chemical-detecting system based on a cross-reactive optical sensor array," *Nature*, vol. 382, pp. 697-700, 1996.
[95] J. White, J. S. Kauer, T. A. Dickinson, and D. R. Walt, "Rapid analyte recognition in a device based on optical sensors and the olfactory system," *Anal. Chem.*, vol. 68, pp. 2191-2202, 1996.
[96] J. H. Krech and S. L. RosePehrsson, "Detection of volatile organic compounds in the vapor phase using solvatochromic dye-doped polymers," *Anal. Chim. Acta*, vol. 341, pp. 53-62, 1997.
[97] K. C. Persaud, S. M. Khaffaf, J. S. Payne, A. M. Pisanelli, D. H. Lee, and H. G. Byun, "Sensor array techniques for mimicking the mammalian olfactory system," *Sens. Actuator B-Chem.*, vol. 36, pp. 267-273, 1996.
[98] M. C. Lonergan, E. J. Severin, B. J. Doleman, S. A. Beaber, R. H. Grubbs, and N. S. Lewis, "Array-based vapor sensing using chemically sensitive, carbon black-polymer resistors," *Chem. Mater.*, vol. 8, pp. 2298-2312, 1996.
[99] http://www.its.caltech.edu/~mmrc/~nsl/nose.htm.

[100] B. J. Doleman, M. C. Lonergan, E. J. Severin, T. P. Vaid, and N. S. Lewis, "Quantitative study of the resolving power of arrays of carbon black-polymer composites in various vapor-sensing tasks," *Anal. Chem.*, vol. 70, pp. 4177-4190, 1998.

[101] E. J. Severin, B. J. Doleman, and N. S. Lewis, "An investigation of the concentration dependence and response to analyte mixtures of carbon black/insulating organic polymer composite vapor detectors," *Anal. Chem.*, vol. 72, pp. 658-668, 2000.

[102] P. Gouma and G. Sberveglieri, "Novel materials and applications of electronic noses and tongues," *Material Research Society (MRS) Bulletin*, vol. 29, pp. 697-700, 2004.